3

CLD modelling: Analytical models

3.1 Introduction

An important part of the work performed throughout this doctoral thesis has been devoted to model the mechanical behaviour of the VE CLD treatments. In this sense, all the models applied have been used to compute the fundamental modal properties of CLD-treated beams, this means, their natural frequency f_1 and their damping ratio, ξ_1. As a result, modal analysis has been a crucial and ever-present tool along the methodology of the thesis.

The mechanical models studied have been classified into two groups: i) analytical ones, and ii) numerical ones. This chapter addresses the first group. More specifically, the analytical model examined has been a PDE that governs the behavior of the so-called 'sandwich beams' with VE core.

The chapter starts with a brief description of the different formulations developed up to today to reproduce the mechanical behavior of the above-mentioned 'sandwich beams'. Then, the particular formulation solved during the chapter is described in detail, clarifying its main assumptions and deriving its PDE together with its boundary conditions (BCs). Later, a methodology to carry out the mechanical coupling of three 'sandwich beam'

segments is described. This has been done with the aim of modelling partially CLD-treated beams (those with a CLD treatment applied only along their lateral regions). Finally a numerical methodology to find exact modal solutions of the equation is described and applied within a parametric study.

3.2 CLD analytical models

The first analytical formulations to model the mechanical behaviour of VE sandwich beams emerged during the decade of the '50s. At that time, the aerospace and the mechanical engineering industry began to demand broad-band and lightweight damping solutions to overcome resonant vibrations. In this scenario, many authors started to research the potential of, at that time, novel VE materials. A holistic and representative contribution that still preserves the feeling of that time is the work published by Ruzicka in 1961 [161] [162]. Most of the investigation developed at the time was impulsed by the U.S.A. government by financing research works developed by companies as Bolt, Beranek and Newman (BBN). In fact, two of the most influential pioneers in the damping research field, Kerwin and Ungar, were BBN employees when they published the first solid work related to the analytical modelling of *Damping of plate flexural vibrations by means of viscoelastic laminae* in 1959 [163] (although preliminary studies had been carried out before).

General framework for viscoelastically-damped bending elements

The majority of the studies proposed to analytically model VE treatments applied to bending elements are derived through analyzing the equilibrium of a differential element of the beam (as the one depicted in Figure 3.1). Most of the authors paid their attention to the study of a 3-layer sandwich beam as the one illustrated in Figure 3.1. This beam has two elastic outer layers (layers 1 and 3) and a VE core (layer 2). Figure 3.1 depicts a generic 2D scenario of analysis (with an x-z coordinate system) which many authors tend to simplify for the sake of an easier mathematical treatment. The beam depicted in this figure has the following characteristics:

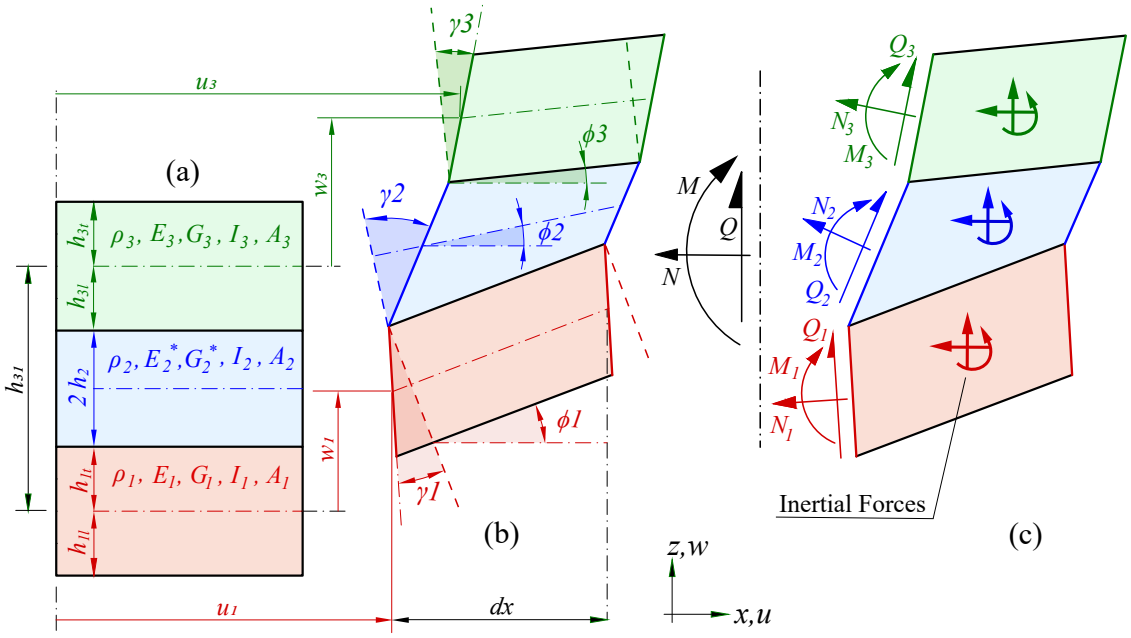

Figure 3.1: Differential slice of a 3-layer sandwich beam with elastic outer faces and a VE core. (a) Non-deformed geometry (b) Deformed geometry (c) Forces in each layer

- Small displacements and curvatures are assumed.
- The two outer layers are made of an elastic material with Young and shear modulus E_1, G_1, E_3 and G_3, respectively, whereas the core is a VE material, with a complex Young and shear modulus E_2^* and G_2^*, respectively (see Figure3.1.(a)).
- The outer layers are considered to be Timoshenko beams capable of resisting bending moments (M_1 and M_3), shear forces (Q_1 and Q_3) and longitudinal extensional forces (N_1 and N_3). These are infinitely rigid with respect to extensional forces in the vertical direction. It is important to highlight that these layers deform to shear as indicated in Figure 3.1.(b) with γ_1 and γ_3 angles.
- The outer layers may have non-symmetric sections. Thus two magnitudes are needed to describe them accurately, namely, h_{1t} and h_{1b} (the distances from the section's centroid to their top and bottom fibers, respectively). Thus, the height of layer 1, h_1 is obtained by $h_1 = h_{1t} + h_{1b}$). The same applies to layer 3.
- The core layer is a bi-dimensional elastic element that behaves in plain-stress. This means that energy dissipation within it arises not only due to its shear, bending or longitudinal extensional deformation but also from a transversal extensional deformation in the vertical direction.

- The vertical and horizontal displacements of the outer layers, w_1, w_3, u_1 and u_3 are considered to be independent, and only related through Kinematic, constitutive and equilibrium equations. Consequently, their derivatives to the $x-coordinate$ are different. This means, for example, that layers 1 and 3 will have distinct curvatures and this difference will be determined by the stiffness in the vertical direction of layer 2.
- The resultant of sectional forces in the sandwich beam section is defined by a bending moment, M, a shear vertical force, Q, and a longitudinal extensional component N. Therefore, the general 'sandwich beam' can be seen as a combination of a bar and a beam element.
- Finally, three types of inertial forces, namely, vertical, longitudinal and rotational, have been considered for each layer. This involves, among other things, that the model is able to predict not only bending vibration modes but also, for instance, shear modes in which layer 3 displaces longitudinally with respect layer 1, deforming layer 2 to shear.

This general framework for the modelling of viscoelastically-damped bending members is far too general and complex to be analytically analyzed. For this reason, many authors have proposed reasonable Kinematic, constitutive and equilibrium assumptions to simplify it, in such a way that analytical solutions can be derived.

Ross, Kerwin and Ungar initial formulation

In their first aforementioned work, Ross, Ungar, and Kerwin [163] proposed a first methodology (usually named RKU formulation) valid to study both, CLD and ULD treatments applied on infinitely long beams vibrating on standing sinusoidal flexural motion. They studied a three-layer element, however, they did not obtain PDE for the beam. Instead, they aimed to compute an overall complex bending stiffness B^* for whole sandwich beam, in such a way that the damping can be obtained from its imaginary part. For that, they assumed the following statements:

- Small displacements are assumed.
- The three layers, 1, 2 and 3 bend in the Euler-Bernoulli's hypothesis.

- Additionally, a shear stiffness is considered in layer 2 which is the only one deforming to shear a magnitude γ_2.
- The vertical displacement w, the rotation ϕ and curvature χ are assumed to be equal in the three layers.
- The three-layer element analyzed is assumed to behave as a beam, thus, in the resultant of sectional forces, the overall axial force is zero, $N = 0$.
- Steady-state sinusoidal flexural motion is assumed in the time and in the spatial domain. This motion is defined by a wave number p_{rku}, and a circular frequency ω_{rku}. This means, that an stationary harmonic wave is being propagated within the infinitely long beam with a speed, $c_{rku} = \omega_{rku}/p_{rku}$.

In their formulation B^* is obtained by dividing the momentum of the sandwich beam section (computed with respect to the overall section's centroid) between the curvature of the section, according to the following equation:

$$M = B^* \frac{\partial \phi}{\partial x} = M_1 + M_2 + M_3 + N1\ h_{10} + N_2\ h_{20} + N_3\ h_{30}, \tag{3.1}$$

where h_{10}, h_{20} and h_{30} are the distances between the centroid of each layer to the overall centroid of the section. The stiffness computed is complex as M_2 and N_2 are complex magnitudes (because they belong to the viscoelastic layer). The complex stiffness computed by them can be rewritten in following form:

$$B^* = B(1 + \eta_B i), \tag{3.2}$$

where B is a real bending stiffness of the sandwich beam, and η_b is the beam's loss factor, which for values lower than 0.2 can be approximately related to the beam's damping ratio, ξ_B, as follows:

$$\xi_B = \eta_B/2. \tag{3.3}$$

The computation of B^* results from stating kinematic, constitutive and equilibrium relation that have not been covered in this thesis (as later, similar ones are used to derived the formulation definitely used in this thesis). To compute B^* two main parameters of the beam are needed: i) h_{10}, and ii) the rate of change of the shear deformation of the VE layer γ_2, with respect the turn angle of the beam ϕ, or $\dfrac{\partial \gamma_2}{\partial \phi}$ (which is constant if

flexural motion is sinusoidal). Both parameters can be computed as a function of the mechanical properties of the beam and the wave number p_{rku}. Hereafter, a summary of their formulation is provided.

For simplicity, the distances from the centroids of layers 3 and 2 to the centroid of layer 1, h_{31} and h_{21}, respectively, are defined as follows:

$$h_{31} = h_{3l} + 2h_2 + h_{1t}, \tag{3.4a}$$

$$h_{21} = h_2 + h_{1t}. \tag{3.4b}$$

A dimensionless factor called 'RKU complex shear parameter' or g^*_{rku} is clarified with the formulation:

$$g^*_{rku} = \frac{G^*_2}{E_3\ I_3\ p^2_{rku}}. \tag{3.5}$$

The parameters h_{10} and $\dfrac{\partial \gamma_2}{\partial \phi}$ may be computed as described below:

$$h_{10} = \frac{E^*_2 A_2 \left(h_{21} - \dfrac{h_{31}}{2}\right) + \left(E^*_2 A_2\ h_{21} + E_3 A_3\ h_{31}\right) g^*_{rku}}{E_1 A_1 + \dfrac{E^*_2 A_2}{2} + g^*_{rku}\left(E_1 A_1 + E^*_2 A_2 + E_3 A_3\right)} \tag{3.6a}$$

$$\frac{\partial \gamma_2}{\partial \phi} = \frac{E_1 A_1\ h_{31} + E^*_2 A_2 \left(h_{31} - h_{21}\right)}{2h_2 \left(E_1 A_1 + \dfrac{E^*_2 A_2}{2} + g^*_{rku}\left(E_1 A_1 + E^*_2 A_2 + E_3 A_3\right)\right)} \tag{3.6b}$$

As a result, B^* can be finally computed by performing simple arithmetic operations between complex numbers as follows:

$$\begin{aligned} B^* =& E_1 I_1 + E^*_2 I_2 + E_3 I_3 + E_1 A_1 h^2_{10} + E^*_2 A_2 \left(h_{10} - h_{21}\right)^2 + E_3 A_3 \left(h_{10} - h_{31}\right)^2 \\ & - E^*_2 I_2 \frac{\partial \gamma_2}{\partial \phi} - 2h_2 \left[\frac{E^*_2 A_2}{2}\left(h_{21} - h_{10}\right) + E_3 A_3 \left(h_{31} - h_{10}\right)\right] \frac{\partial \gamma_2}{\partial \phi}, \end{aligned} \tag{3.7}$$

A mechanical interpretation of this equation is here provided. The first three terms of the equation correspond to the contributions of each layer to the bending stiffness, the next three are the Steiner's contribution of each layer, the seventh is negative and represents a decrease in the bending stiffness of layer 2 as it deforms to shear, finally the

eight term corresponds to a reduction of the Steiner's contributions of layers 2 and 3 due to a shear deformation of layer 2.

To sum up, given a sandwich beam with a set of mechanical properties and a wave number p_{rku}, a complex stiffness B^* may be obtained. This methodology can be reasonably applied to the particular case of simply-supported beams, as their bending modes are well approximated by sinusoidal functions. To proceed, a given beam length, L_B, and a particular vibration mode index, n, need to be fixed. Then, according to the conceptual representation of Figure 3.2, the wave length, λ, to be transmitted into the beam is derived according to:

$$L_B = \frac{n\lambda}{2} \implies \lambda = \frac{2L_B}{n}. \tag{3.8}$$

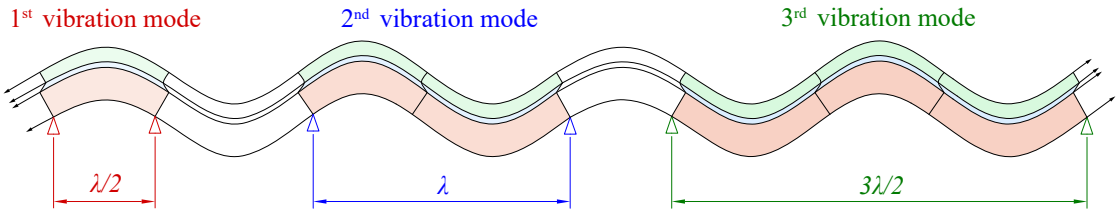

Figure 3.2: Graphical representation of the 'sandwich beam' reproduced with the RKU model and its applicability to simply supported beams

Thereby, the value of p_{rku} (needed to obtain B^*) may be computed as a function of n and L_B as indicated below:

$$p_{rku} = \frac{2\pi}{\lambda} = \frac{\pi n}{L_B} \tag{3.9}$$

Finally, once B^* has been calculated, a complex circular frequency ω^*_{rku} might be derived. As a result of assuming sinusoidal flexural motion, the following relation stays true:

$$\omega^*_{rku} = \sqrt{\frac{p^4_{rku}B^*}{m}} = \sqrt{\frac{p^4_{rku}B}{m}}\sqrt{1+\eta_B i} = w_{rku}\sqrt{1+\eta_B i}, \tag{3.10}$$

ω^*_{rku} is a complex circular frequency that can be expressed as a function of two modal parameters, i) the real circular frequency of motion ω_{rku}, and ii) the loss factor η_B.

Although the RKU model is limited to simply supported beams, it provided the researchers with an overview of how to damp bending vibrations with VE materials. In

fact, the model works for both CLD and ULD treatments, since it takes into account the bending stiffness of the VE layer. This allows to consider the additional energy dissipation from the extensional deformation of layer 2 to be considered. With this model, a whole set of different VE treatments (as those shown in Figure 3.3 can be modelled assessing the influence of both extensional and shear damping mechanisms in the final application designed.

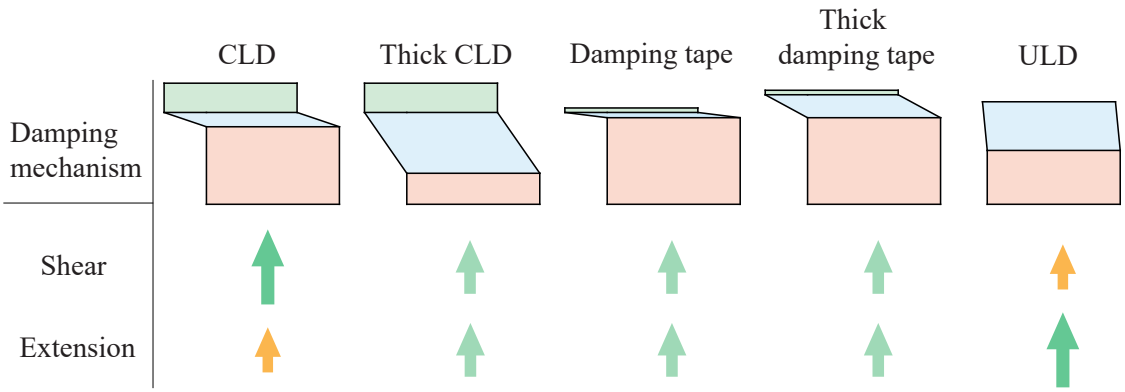

Figure 3.3: Contribution of each structural element to the total EC of the structure of a building. [5]

PDE of the sandwich beam with VE core: Mead's equilibrium derivation

Despite its usefulness, the RKU model does not provide an PDE. This fact limits its ability to assess the effectiveness of VE damping treatments for BCs other than simply supported beams. For this reason, during the decades of the '60s, '70s and '80s some researchers were focused on developing PDEs for sandwich beams with VE cores. The role models for these emergent formulations were the widespread PDEs already developed for elastic beams or shell elements.

Probably, the most popular was the one derived by DiTaranto[164] in 1965. DiTaranto proposed a PDE based on various time and spatial derivatives of the horizontal displacement u_1, and even, proposed a solution method that he did not applied. Even though the PDE derived by DiTaranto[164] was significant for the modelling of sandwich beams, the use of u_1 was considered as a drawback of the formulation, since beam PDEs have been traditionally expressed as a function of the vertical deflection. This was finally achieved by Mead and Markus in 1969 also obtaining the equations for different BCs, analyzing the equilibrium of a differential beam segment. Finally, in 1974, Rao [166] built

the same formulation using an energetic methodology based on the Hamilton's principle. Additionally, he numerically solved the modal analysis of this PDE for different BCs combinations, providing a whole set of exact solutions valid for beams treated with CLD along its whole length.

In this subsection a comprehensive derivation of the sandwich beam PDE is given based on Mead and Markus's contribution. The main simplifications assumed by DiTaranto with respect to the general framework are summarized in Figure 3.4 and are listed below:

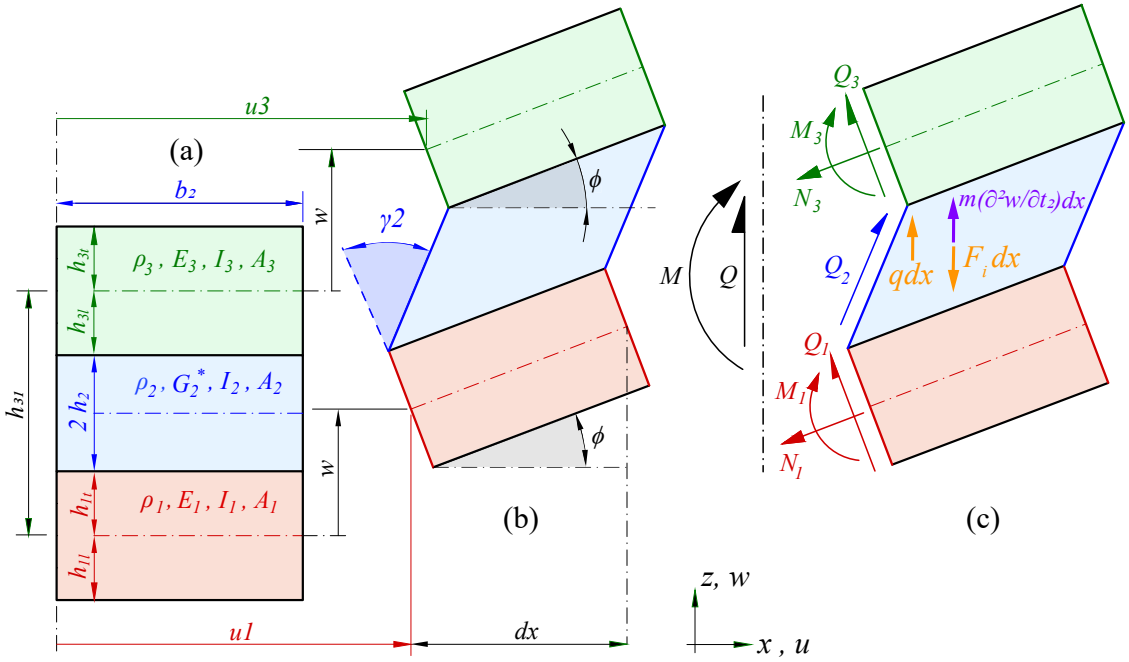

Figure 3.4: Differential slice of the sandwich beam analyzed by DiTaranto, Mead *et al.* and [166]

- Small vertical displacements and curvatures are assumed.
- The elastic outer layers bend in the Euler-Bernoulli's Hypothesis.
- The VE core is modelled just assuming its shear stiffness. Hence, neither its bending or extensional stiffness are considered.
- The beam vertical deflection w is equal for the three layers of the sandwich beam section.

- The resultant of extensional longitudinal forces in the sandwich beam is null. This means that the element being analyzed behaves as a beam but not as a bar.
- Longitudinal and rotational inertial forces are ignored and only the vertical one is taken into account.

These are the same assumptions stated in the RKU model with the exception of 'just considering the shear stiffness of the VE core'. This indicates that DiTaranto's formulation is only valid to analyze CLD, but not ULD. In addition, the PDE derivation process has been divided into four steps coinciding with the subfigures presented in Figure 3.5. This Figure has been included to ease the reader's understanding along with the equations. A fifth step is finally included to reorganize all the equations and clean the terminology.

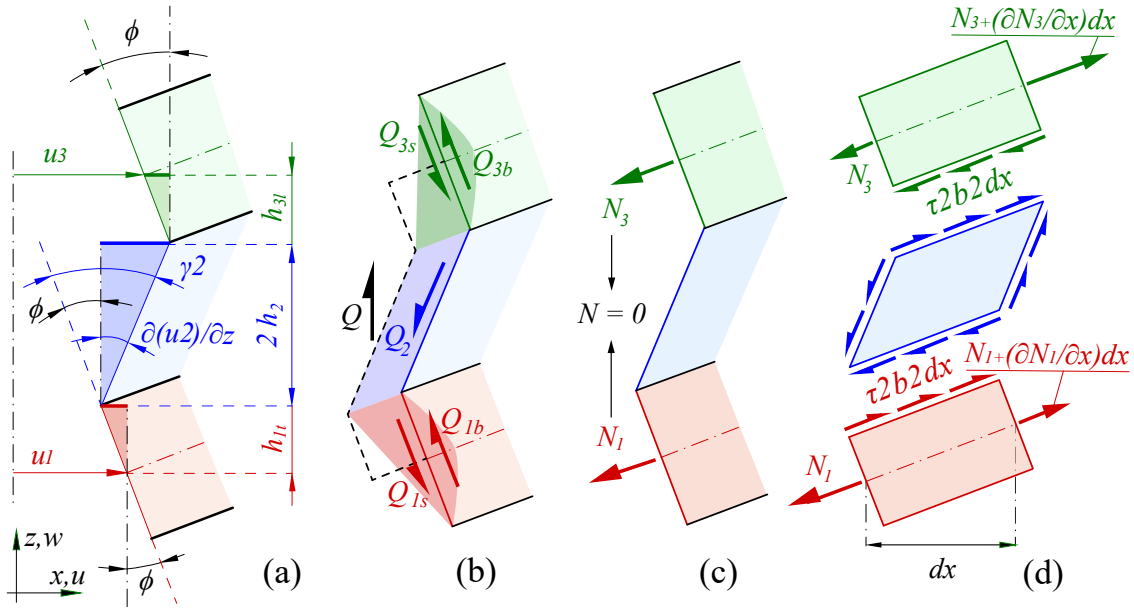

Figure 3.5: kinematic and equilibrium relations needed to derive the PDE of the sandwich beam with VE core

The deduction of the PDE has been divided into the four steps illustrated in 3.5:

1. Mechanical behaviour of the VE core

The building process of the PDE starts deducing a kinematic relation within the sandwich beam section. For that, in Figure 3.5.(a) three main angles can be distinguished: i) ϕ which represents the turn bending angle equals to $\partial w/\partial x$, ii) γ_2 which is the shear deformation angle of the VE core, and iii) $\partial u_2/\partial z$ that is the variation of the horizontal

displacements within layer 2 along the vertical coordinate z. From this figure, it results evident that:

$$\gamma_2 = \phi + \frac{\partial u_2}{\partial z} \tag{3.11}$$

It may be useful to express $\partial u_2/\partial z$ as a function of u_3, u_1 and ϕ. The three shaded triangles depicted in Figure 3.5.(a) may help to obtain the following relation. All the angles have been approximated by the value of their tangents (as Bernoulli hypothesis are assumed):

$$\frac{\partial u_2}{\partial z} = \frac{u_3 + \phi\ h_{3b} - (u_1 - \phi\ h_{1t})}{2h_2}. \tag{3.12}$$

Substituting equation 3.12 into 3.11 the following one is obtained:

$$\gamma_2 = \frac{h_{31}\ \phi}{2h_2} + \frac{u_3 - u_1}{2h_2} \tag{3.13}$$

It is important to clarify here that the shear strain has been assumed to be constant along the thickness of the VE core, which is a result of neglecting its bending and longitudinal extensional stiffness. Consequently the shear stress is also constant and it is equal to:

$$\tau_2 = G_2^*\ \gamma_2 \tag{3.14}$$

2. Equilibrium of vertical forces into the differential slice

At this point, the total vertical shear force Q in the sandwich beam section needs to be computed. A graphical representation of the different shear stress components that build Q is shown in Figure 3.5.(b). Given that the outer layers bend in the Euler's hypothesis, their shear force due to bending can be defined as follows:

$$Q_1 b = E_1 I_1\ \frac{\partial^3 w}{\partial x^3} \tag{3.15a}$$

$$Q_3 b = E_3 I_3\ \frac{\partial^3 w}{\partial x^3} \tag{3.15b}$$

The shear deformation of the VE core generates a constant shear stress τ_2 within the viscoelastic core. This shear stress is also present at the inner faces of layers 1 and 3 and

decreases linearly along their thickness till being zero at their outer faces. These shear stresses are illustrated with shaded areas in Figure 3.5.(b) together with their resultant forces, Q_2, $Q_1 s$ and $Q_3 s$, respectively. The total force caused by the shear deformation of layer 2 may can be computed as follows:

$$Q_2 + Q_{1S} + Q_3 s = -\tau_2 b_2 h_{31}. \tag{3.16}$$

The above equation is an approximation derived form assuming that the integral of the shaded area in Figure 3.5.(b) is equal to the one delimited by dashed lines. The negative sign into this equation is due to the fact that this force has to go downwards (given the depicted deformation of the shear layer) whereas the other shear forces have been initially assumed to go upwards. The total shear force of the section, Q can be now computed:

$$\begin{aligned} &Q = Q_{1b} + Q_{3b} + Q_2 + Q_{1S} + Q_3 s \implies \\ &Q = (E_1 I_1 + E_3 I_3)\,\frac{\partial^3 w}{\partial x^3} - G_2^*\; b_2\; h_{31}\left(\frac{h_{31}}{2h_2}\frac{\partial w}{\partial x} + \frac{u_3 - u_1}{2h_2}\right) \end{aligned} \tag{3.17}$$

Finally, assuming that the three-layer element analyzed behaves as a beam the following equation for the equilibrium of vertical forces stays valid:

$$\begin{aligned} &p = \frac{\partial Q}{\partial x} \implies \\ &p = (E_1 I_1 + E_3 I_3)\,\frac{\partial^4 w}{\partial x^4} - \frac{G_2^*\; b_2\; h_{31}^2}{2h_2}\frac{\partial^2 w}{\partial x^2} - \frac{G_2^*\; b_2\; h_{31}}{2h_2}\left(\frac{\partial u_3}{\partial x} - \frac{\partial u_1}{\partial x}\right) \end{aligned} \tag{3.18}$$

being p the resultant of vertical forces acting over the differential element and pointing in the z positive direction. At this point, the equilibrium equation is expressed in terms of three kinematic variables (w, u_1 and u_3). Hence, more mechanical relations between these variable are needed to be rewrite the equation only in terms of w.

3. Beam behaviour: resultant of extensional forces equals zero

As stated before, the three-layer element studied behaves as a beam element, and thus, the overall extensional force should be zero $N = 0$. This means that:

$$N_1 + N_3 = 0 \implies N_1 = -N_3 \tag{3.19}$$

Then, extensional forces of layers 1 and 3 may be expressed as:

$$N_1 = E_1 A_1 \frac{\partial u_1}{\partial x}, \tag{3.20a}$$

$$N_3 = E_3 A_3 \frac{\partial u_3}{\partial x}. \tag{3.20b}$$

Thus, the following relation between u_1 and u_3 is derived through combining the two above equation and integrating with respect to x:

$$E_1 A_1 u_1 = -E_3 A_3 u_3 \tag{3.21}$$

Substituting this last relation into Equation 3.18 this one can be rewritten as follows, only depending on w and u_1:

$$p = (E_1 I_1 + E_3 I_3) \frac{\partial^4 w}{\partial x^4} - \frac{G_2^* \; b_2 \; h_{31}^2}{2h_2} \frac{\partial^2 w}{\partial x^2} + \frac{G_2^* \; b_2 \; h_{31}}{2h_2} \left(\frac{E_1 \; A_{\;1} + E_3 A_3}{E_3 \; A_3} \right) \frac{\partial u_1}{\partial x} \tag{3.22}$$

4. Equilibrium of extensional forces on layer 1

The last relation needed to eventually express the PDE in terms of just w is the one derived from analyzing the equilibrium of extensional forces on layers 1 and 3 (see Figure 3.5.(d)). Analyzing layer 1 the following equilibrium expression is obtained:

$$\begin{gathered} N_1 = \tau_2 \; b_2 \; dx + N_1 + \frac{\partial N_1}{\partial x} dx \implies \\ -\tau_2 \; b_2 = \frac{\partial N_1}{\partial x} \end{gathered} \tag{3.23}$$

By substituting into this equation those derived for τ_2(Equation 3.14) and N_1 (Equation 3.20a), the following one is derived:

$$E_1 A_1 \frac{\partial^2 u_1}{\partial x^2} - \frac{G_2^* b_2}{2h_2} \left[\frac{E_1 A_1 + E_3 A_3}{E_3 A_3} \right] u_1 = -\frac{G_2^* b_2 h_{31}}{2h_2} \frac{\partial w}{\partial x} \tag{3.24}$$

At this point, all the equations needed to derive the final partial differential equation (PDE) have been established. All that remains is clean-up work and rewriting.

5. Formulation clean-up and rewriting

For that, it results convenient to define two parameters that will simplify the notation. The first one is dimensionless and is the so-called Kerwin's 'Geometric parameter' Y, defined as follows.

$$Y = \frac{{h_{31}}^2}{(E_1 I_1 + E_3 I_3)} \frac{E_1 A_1 E_3 A_3}{(E_1 A_1 + E_3 A_3)} \tag{3.25}$$

This parameter was mechanically interpreted by Mead *et al.* He realized that Y represents the percentage of additional bending stiffness achieved when both elastic layers (1 and 3) bend as a unique monolithic section compared to when they bend as independent sections. In other words, the proportion in which the bending stiffness increases when the central core is infinitely rigid in shear compared to when its shear stiffness is negligible.

The second parameter used is the one called 'Mead's complex shear parameter' g_m^* and is defined as indicated below:

$$g_m^* = \frac{G_2^* b_2}{2h_2} \frac{(E_1 A_1 + E_3 A_3)}{E_1 A_1 E_3 A_3} \tag{3.26}$$

This parameter makes reference to the shear stiffness of the viscoelastic core, as it can be seen by its first multiplying factor.

Now, both equilibrium equations, the one of the shear force (Equation 3.22) and the one of the extensional force in layer 1 (Equation 3.24 can be written in terms of Y and g_m^* in the following way:

$$\frac{p}{(E_1 I_1 + E_3 I_3)} = \frac{\partial^4 w}{\partial x^4} - g_m^* Y \frac{\partial^2 w}{\partial x^2} + g_m^* \frac{E_1 A_1 h_{31}}{(E_1 I_1 + E_3 I_3)} \frac{\partial u_1}{\partial x} \tag{3.27a}$$

$$\frac{\partial^2 u_1}{\partial x^2} - g_m^* u_1 = -g_m^* Y \frac{(E_1 I_1 + E_3 I_3)}{E_1 A_1 h_{31}} \frac{\partial w}{\partial x} \tag{3.27b}$$

Finally, both equations can be condensed into the final PDE in terms of w, which is the PDE for the forced vertical motion of the sandwich beam:

$$\frac{\partial^6 w}{\partial x^6} - g_m^* (1 + Y) \frac{\partial^4 w}{\partial x^4} = \frac{1}{(E_1 I_1 + E_3 I_3)} \left(\frac{\partial^2 p}{\partial x^2} - gp \right). \tag{3.28}$$

Now, the overall vertical load p needs to be defined as a function of two components: i) the inertial force F_i (equal in magnitude to the mass times the acceleration but in the opposite sense), and ii) an external vertical force q. Thus p may be expressed as follows:

$$p = q(x,t) + F_i = q(x,t) - m \frac{\partial^2 w}{\partial t^2} \tag{3.29}$$

Including this equation into the previous one, and assuming that q is zero, the equation for the free vibrations of the sandwich beam arises:

$$\frac{\partial^6 w}{\partial x^6} - g_m^*(1+Y)\frac{\partial^4 w}{\partial x^4} + \frac{m}{(E_1 I_1 + E_3 I_3)}\frac{\partial^2}{\partial t^2}\left(\frac{\partial^2 w}{\partial x^2} - w\right) = 0 \tag{3.30}$$

This equation can be further simplified, by expressing it as PDE with dimensionless coefficients. This was first achieved by Rao [166] in 1978, by developing an energetic derivation of the PDE that is provided hereafter.

PDE of the sandwich beam with VE core: Rao's equilibrium derivation

In order to achieve a PDE with dimensionless coefficients, Rao decided to use dimensionless time $\bar{t}$, and space $\bar{x}$ expressed as follows:

$$\bar{t} = \frac{t}{\sqrt{\frac{mL^4}{E_1 I_1 + E_3 I_3}}} \tag{3.31a}$$

$$\bar{x} = \frac{x}{L} \tag{3.31b}$$

where L expresses the length of the beam to be analyzed. Like Mead and Markus, he additionally built two parameters that simplify the Equation 3.30, however, now, both of them are dimensionless. The first one is Y and the second one is the so-called 'dimensionless complex shear parameter' or g^* which is computed in the following way:

$$g* = \frac{G_2^* A_2 L^2}{4h_2^2}\frac{(E_1 A_1 + E_3 A_3)}{E_1 A_1 E_3 A_3} = g\,(1 + j\eta_2) \tag{3.32}$$

where g is just called the 'shear parameter' and $\eta_{2,ve}$ is the loss factor of the VE material of layer 2.

Rao derives the PDE using a variational energetic procedure, thus, the energies involved in the sandwich beam motion need to be outlined. Firstly, three potential elastic energies are used, namely, the bending and extensional ones of layers 1 and 3, $(V_1 + V_3)_{bending}$ and $(V_1 + V_3)_{extension}$, respectively, and the shear one of layer 2, $(V_2)_{shear}$. Secondly, the kinetic energy for the motion in the vertical direction, T, is defined. Finally, the work produced by the external forces W_e is included (in the equation the only external force considered is F_i, thus assuming that $q = 0$). The equations for computing these

energies can be finally expressed in terms of dimensionless derivatives of w and u. where u is a parameter that represents the slip between faces and is expressed as follows:

$$u = \frac{2h_2 L}{h_{31}}\gamma_2 \tag{3.33}$$

The final expressions for the energies expressed are the following ones:

$$\begin{aligned}(V_1+V_3)_{\text{bending}} &= \frac{1}{2}\left(E_1I_1+E_3I_3\right)\int_0^L \frac{\partial^2 w}{\partial x^2}dx \\ &= \frac{1}{2}\frac{\left(E_1I_1+E_3I_3\right)}{L^3}\int_0^1 \frac{\partial^2 w}{\partial \bar{x}^2}d\bar{x}\end{aligned} \tag{3.34a}$$

$$\begin{aligned}(V_1+V_3)_{\text{extension}} &= \frac{1}{2}\int_0^L \left(E_1A_1\frac{\partial^2 u_1}{\partial x^2}+E_3A_3\frac{\partial^2 u_3}{\partial x^2}\right)dx \\ &= \frac{1}{2}\frac{\left(E_1I_1+E_3I_3\right)}{L^3}\int_0^1 \left(\frac{\partial^2 w}{\partial \bar{x}^2}-\frac{\partial u}{\partial \bar{x}}\right)d\bar{x}\end{aligned} \tag{3.34b}$$

$$(V_2)_{\text{shear}} = \frac{1}{2}\int_0^L G_2^* A_2 \gamma_2^2\, dx = \frac{1}{2}\frac{\left(E_1I_1+E_3I_3\right)}{L^3 g^*}Y\int_0^1 u^2 d\bar{x} \tag{3.34c}$$

$$T = \frac{1}{2}m\int_0^L \frac{\partial^2 w}{\partial t^2}dx \;= \frac{1}{2}\frac{\left(E_1I_1+E_3I_3\right)}{L^3}\int_0^1 \frac{\partial^2 w}{\partial \bar{t}^2}d\bar{x} \tag{3.34d}$$

$$W_e = \int_0^L w\left(-m\frac{\partial^2 w}{\partial t^2}\right)dx = \frac{\left(E_1I_1+E_3I_3\right)}{L^3}\int_0^1 w\left(-m\frac{\partial^2 w}{\partial t^2}\right)d\bar{x} \tag{3.34e}$$

Then, using these equations the Lagrangian of the sandwich beam system, L_g, may be built as follows:

$$L_g = T - (V_1+V_3)_{bending} - (V_1+V_3)_{extension} - (V_2)_{shear} + W_e \tag{3.35}$$

Applying Hamilton's principle to this Lagrangian the following expression is obtained:

$$\int_{t_1}^{t_2}\delta\left(L\right)dt = 0 \implies \sqrt{\frac{\left(E_1I_1+E_3I_3\right)}{mL^4}}\int_{\bar{t}_1}^{\bar{t}_2}\delta\left(L\right)d\bar{t} = 0 \tag{3.36}$$

By substituting the Lagrangian into this equation and applying the rules of variational calculus, the PDE for the free vibrations of the sandwich beam and its BCs naturally

emerge. This PDE is the same as the one derived by Mead and Markus (Equation 3.30), but expressed with dimensionless coefficients:

$$\frac{\partial^6 w}{\partial \bar{x}^6} - g^*(1+Y)\frac{\partial^4 w}{\partial \bar{x}^4} + \frac{\partial^2}{\partial \bar{t}^2}\left(\frac{\partial^2 w}{\partial \bar{x}^2} - g^* w\right) = 0 \tag{3.37}$$

The BCs associated with this PDE are six and they are grouped into three pairs of 'kinematic or force constrains'. This implies that, at any end, either the vertical displacement w or the shear force Q must be zero, but not both of them. Similarly, one of the two between the turn angle ϕ or the bending moment M, has to be zero. Finally, either the longitudinal slip u or the extensional force in the elastic layer N must be zero. The equations that enable computing these BCs are given below:

$$w = 0 \qquad or \tag{3.38a}$$

$$Q = \frac{(E_1 I_1 + E_3 I_3)}{L^3}\left(\frac{\partial^5 w}{\partial \bar{x}^5} - g^*(1+Y)\frac{\partial^3 w}{\partial \bar{x}^3} + \frac{\partial^2}{\partial \bar{t}^2}\left(\frac{\partial w}{\partial \bar{x}}\right)\right) = 0, \tag{3.38b}$$

$$\phi = \frac{\partial w}{\partial \bar{x}} = 0 \qquad or \tag{3.38c}$$

$$M = \frac{-(E_1 I_1 + E_3 I_3)}{L^2}\left(\frac{\partial^4 w}{\partial \bar{x}^4} - g^*(1+Y)\frac{\partial^2 w}{\partial \bar{x}^2} + \frac{\partial^2 w}{\partial \bar{t}^2}\right) = 0, \tag{3.38d}$$

$$u = \frac{\partial^5 w}{\partial \bar{x}^5} - g^* Y\frac{\partial^3 w}{\partial \bar{x}^3} + \frac{\partial^2}{\partial \bar{t}^2}\left(\frac{\partial w}{\partial \bar{x}}\right) = 0 \qquad or \tag{3.38e}$$

$$N = Y\left(\frac{\partial^4 w}{\partial \bar{x}^4} - g^* Y\frac{\partial^2 w}{\partial \bar{x}^2} + \frac{\partial^2 w}{\partial \bar{t}^2}\right) = 0. \tag{3.38f}$$

Thus, eight types of beam edges arise from combining these BCs. These are illustrated in Table 3.1 together with their identifying names and defining equations. From now on, the chapter will deal with the equations derived by Rao based on the dimensionless parameters Y and g^*.

Table 3.1 Possible edge types applicable to the Sandwich beam with VE core [166].

Type of edge	Non-deformed Deformed	Equation
Free	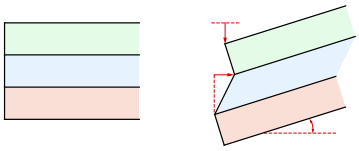	$Q = M = N = 0$
Free, riveted	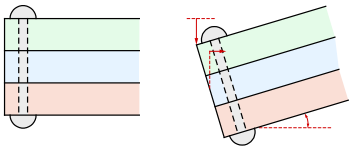	$Q = M = u = 0$
Pinned	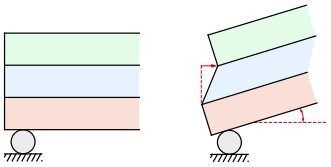	$w = M = N = 0$
Pinned, riveted	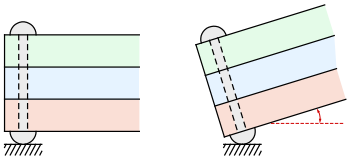	$w = M = u = 0$
Clamped (unrestrained)	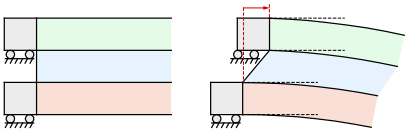	$w = \phi = N = 0$
Clamped, riveted	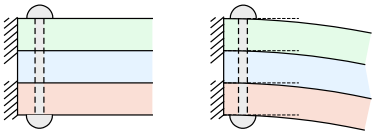	$w = \phi = u = 0$
Sliding	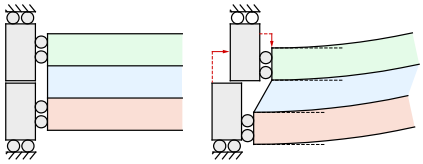	$\phi = Q = N = 0$
Sliding, riveted	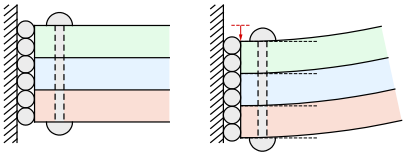	$\phi = Q = u = 0$

3.3 Modal solution of the PDE for the free vibrations of sandwich beams

3.3.1 Solution approach

Once the PDE for the free vibrations of the sandwich beam has been derived, the next step is to provide a solution.

The PDE to be solved has constant coefficients with a complex nature, as the parameter g^* is, indeed, complex. Thus, the solution to this equation has to be similar to the one applicable to a constant-coefficients PDE, but complex. Taking the separation of variables and assuming a harmonic nature of the solution, the following solution of the equation might be proposed.

$$w(\bar{x},\bar{t}) = A^*\ e^{\Omega^*\bar{t}}\ e^{K^*\bar{x}} \tag{3.39}$$

where A^* is a complex coefficient, Ω^* is a 'dimensionless complex circular frequency' also called 'circular frequency factor' that defines the rhythm of motion. The parameter Ω^* is a dimensionless version of the complex natural frequency of the sandwich beam derived by Ross, Ungar, and Kerwin in Equation 3.10. and K^* represents the so-called 'Characteristic values' which are a sort of wave numbers that define the shape of the harmonic motion along the beam. Substituting this solution into Equation 3.37, the following complex polynomial equation is obtained:

$$K^{*6} - g^*(1+Y)K^{*4} + \Omega^{*2}\left(K^{*2} - g^*\right) = 0 \tag{3.40}$$

Assuming that Ω^* is a known parameter, this equation results to be a bi-cubic polynomial with six solutions organized in three pairs. Hence, each value of Ω^* is related to six zeros of this polynomial equation $K_1^*(\Omega^*)$, $K_2^*(\Omega^*)$, $K_3^*(\Omega^*)$, $K_4^*(\Omega^*)$, $K_5^*(\Omega^*)$ and $K_6^*(\Omega^*)$. For this reason, a more general harmonic solution to be used for solving the PDE is the following one:

$$w(\bar{x},\bar{t}) = \left(A_1^*\ e^{K_1^*\bar{x}} + A_2^*\ e^{K_2^*\bar{x}} + A_3^*\ e^{K_3^*\bar{x}} + A_4^*\ e^{K_4^*\bar{x}} + A_5^*\ e^{K_5^*\bar{x}} + A_6^*\ e^{K_6^*\bar{x}}\right) e^{\Omega^*\bar{t}} \tag{3.41}$$

where A_1^* to A_6^* is a set of six complex constants that are also bi-univocally related to ω^*. These can be determined through a system of equations resulting from imposing the six

boundary conditions of the beam.

Given a certain beam with three BCs at $\bar{x} = 0$ and three more at $\bar{x} = 1$, this can be represented with a system of six PDEs each one given by a BC PDE (as those shown in Equations 3.38). By substituting the solution given in Equation 3.41 in those PDEs the derivatives disappear and the system is expressed in terms of A_j^*, K_j^* and Ω^* (where j is used as an index). Then, if a given value is assigned to Ω^*, the values of K_j^* are determined as the zeros of Equation 3.40 and hence, the only unknowns are the values of A_j^*.

A modal solution for the free vibration motion of a structural system is never unique. In fact, a mode shape is not a unique function depending on the spatial coordinate x, but a set of infinite homothetic functions. This implies that the system of equations above-mentioned must have infinite A_j^* solutions when searching for a modal solution of the PDE, thus, being compatible but non-determined. This is the same as saying that the determinant of the system needs to be zero. Thus, this solution process can be summed up as 'finding a complex value of Ω^* that provides a system determinant equal to zero'.

An example of a simply-supported 'sandwich beam' with both pinned edges at $\bar{x} = 0$ and $\bar{x} = 1$ is here provided. For this particular case, the BCs are the following ones:

$$w(\bar{x}=0) = w(\bar{x}=1) = N(\bar{x}=0) = N(\bar{x}=1) = M(\bar{x}=0) = M(\bar{x}=1) = 0 \tag{3.42}$$

Substituting the solution for w the previous BCs look like this:

$$w = \left(\sum_{i=1}^{6} A_j^* \; e^{K_j^* \bar{x}} \right) e^{\Omega^* \bar{t}} = 0 \tag{3.43a}$$

$$M = \frac{-\left(E_1 I_1 + E_3 I_3\right)}{L^2} \left(\sum_{j=1}^{6} A_j^* \; e^{K_j^* \bar{x}} \left(K_j^{*4} - g^*(1+Y) K_j^{*2} + \Omega^{*2} \right) \right) e^{\Omega^* \bar{t}} = 0 \tag{3.43b}$$

$$N = Y \left(\sum_{j=1}^{6} A_j^* \; e^{K_j^* \bar{x}} \left(K_j^{*4} - g^* Y K_j^{*2} + \Omega^{*2} \right) \right) e^{\Omega^* \bar{t}} = 0 \tag{3.43c}$$

And particularizing for their $\bar{x}$ coordinates the following system of equations arises:

$$w(\bar{x}=0) = \sum_{j=1}^{6} A_i^* = 0 \tag{3.44a}$$

$$M(\bar{x}=0) = \sum_{j=1}^{6} A_j^* \left(K_j^{*4} - g^*(1+Y)K_j^{*2} + \Omega^{*2} \right) = 0 \tag{3.44b}$$

$$N(\bar{x}=0) = Y \sum_{j=1}^{6} A_j^* \left(K_j^{*4} - g^* Y K_j^{*2} + \Omega^{*2} \right) = 0 \tag{3.44c}$$

$$w(\bar{x}=1) = \sum_{j=1}^{6} A_j^* \; e^{K_j^*} = 0 \tag{3.44d}$$

$$M(\bar{x}=1) = \sum_{j=1}^{6} A_j^* \; e^{K_j^*} \left(K_j^{*4} - g^*(1+Y)K_j^{*2} + \Omega^{*2} \right) = 0 \tag{3.44e}$$

$$N(\bar{x}=1) = \sum_{j=1}^{6} A_j^* \; e^{K_j^*} \left(K_j^{*4} - g^* Y K_j^{*2} + \Omega^{*2} \right) = 0 \tag{3.44f}$$

This system of equations can be expressed in a matricial way as follows:

$$\begin{bmatrix} 1 & ... & 1 \\ K_1^{*4} - g^*(1+Y)K_1^{*2} + \Omega^{*2} & ... & K_6^{*4} - g^*(1+Y)K_6^{*2} + \Omega^{*2} \\ K_1^{*4} - g^* Y K_1^{*2} + \Omega^{*2} & ... & K_6^{*4} - g^* Y K_6^{*2} + \Omega^{*2} \\ e^{K_1^*} & ... & e^{K_6^*} \\ e^{K_1^*} \left(K_1^{*4} - g^*(1+Y)K_1^{*2} + \Omega^{*2} \right) & ... & e^{K_6^*} \left(K_6^{*4} - g^*(1+Y)K_6^{*2} + \Omega^{*2} \right) \\ e^{K_1^*} \left(K_1^{*4} - g^* Y K_1^{*2} + \Omega^{*2} \right) & ... & e^{K_6^*} \left(K_6^{*4} - g^* Y K_6^{*2} + \Omega^{*2} \right) \end{bmatrix} \begin{bmatrix} A_1^* \\ A_2^* \\ A_3^* \\ A_4^* \\ A_5^* \\ A_6^* \end{bmatrix} = \begin{bmatrix} 0 \\ 0 \\ 0 \\ 0 \\ 0 \\ 0 \end{bmatrix}, \tag{3.45a}$$

$$M(\Omega^*)\boldsymbol{a} = \mathbf{0}, \tag{3.45b}$$

where $M(\Omega^*$ is the matrix of the system, $\boldsymbol{a}$ is the column vector of complex coefficients and $\mathbf{0}$ is a column vector of zeros.

Finally, to find the modal solutions for this beam, the following transcendental equation needs to be solved for Ω^*:

$$\det\left(M(\Omega^*)\right) = 0 \tag{3.46}$$

These equations have infinite solutions for Ω^* (also called 'zeros' or 'roots') that enable

the determinant to be equal to zero. Each solution corresponds to a complex natural frequency of the sandwich beam analyzed. Nevertheless, these transcendental equations rarely have closed-form solutions as formulae that directly provide their roots. For this reason, 'root-finding' numerical algorithms, similar to the secant method, need to be used to solve them.

3.3.2 Closed-form solution for the simply-supported sandwich beam

The only case for which a closed-form solution exists is the simply supported one with pinned BCs at both edges. Before introducing this expression it is convenient to remember that the roots for Ω^*, from now on called Ω_n^* (being n an index referring to the ordinal position of each root) can be expressed as follows:

$$\Omega_n^* = \omega_n^* \sqrt{\frac{mL^4}{E_1 I_1 + E_3 I_3}} = \Omega_n \sqrt{1 + i\eta_n} \,, \tag{3.47}$$

where ω_n^* is the dimensional n^{th} complex circular frequency and, Ω_n and η_n are the n^{th} dimensionless circular frequency and the n^{th} loss factor, respectively, associated to the beam's n^{th} vibration mode.

The solution for Ω_n and η_n were firstly derived by Ross, Ungar, and Kerwin and are coincident with those later derived by DiTaranto and Rao. These, are given below:

$$\Omega_n = \sqrt{\frac{(n\pi)^4 + (n\pi)^2 (2+Y)\, g + \left(1 + \eta_{2,ve}^2\right)(1+Y)\, g^2}{(n\pi)^4 + 2\,(n\pi)^2\, g + \left(1 + \eta_{2,ve}^2\right) g^2}}\, (n\pi)^2 \tag{3.48a}$$

$$\eta_n = \frac{(n\pi)^2\, gY\, \eta_{2,ve}}{(n\pi)^4 + (n\pi)^2 (2+Y)\, g + \left(1 + \eta_{2,ve}^2\right)(1+Y)\, g^2} \tag{3.48b}$$

It can be seen that the value of the η_n is a function of the shear parameter g. This means that the shear stiffness of the VE core (not only dependant on G_2^* but also on b_2 and h_2) influences the final damping capacity of the sandwich beam. Building on this idea, Mead thought it could be interesting to know the maximum loss factor achievable on a sandwich beam defined by Y and $\eta_{2,ve}$ by changing its$g$ (for example, modifying the sizes b_2 or h_2). As a result, he obtained two expressions that provide the maximum loss factor to be achieved, called η_{max}, and the optimal value of the shear parameter that provides it, called $g_{n,opt}$:

$$\eta_{max} = \frac{\eta_{2,ve} Y}{(2+Y) + 2\sqrt{(1+Y)\left(1+\eta_{2,ve}^2\right)}} \tag{3.49a}$$

$$g_{n,opt} = \frac{(n\pi)^2}{\sqrt{(1+Y)\left(1+\eta_{2,ve}^2\right)}} \tag{3.49b}$$

It is interesting to mention that η_{max} does not depend on the mode number n, but that $g_{opt,n}$ increases quadratically with it.

3.3.3 Iterative root-finding solution

Despite what has been presented in the previous subsection, for the majority of cases there is no formula that directly provides the zeros for these equations, so they need to be searched with iterative root-finding techniques. For a better understanding of the function $\det(M(\Omega^*))$ two different cases have been represented in Figure 3.6.

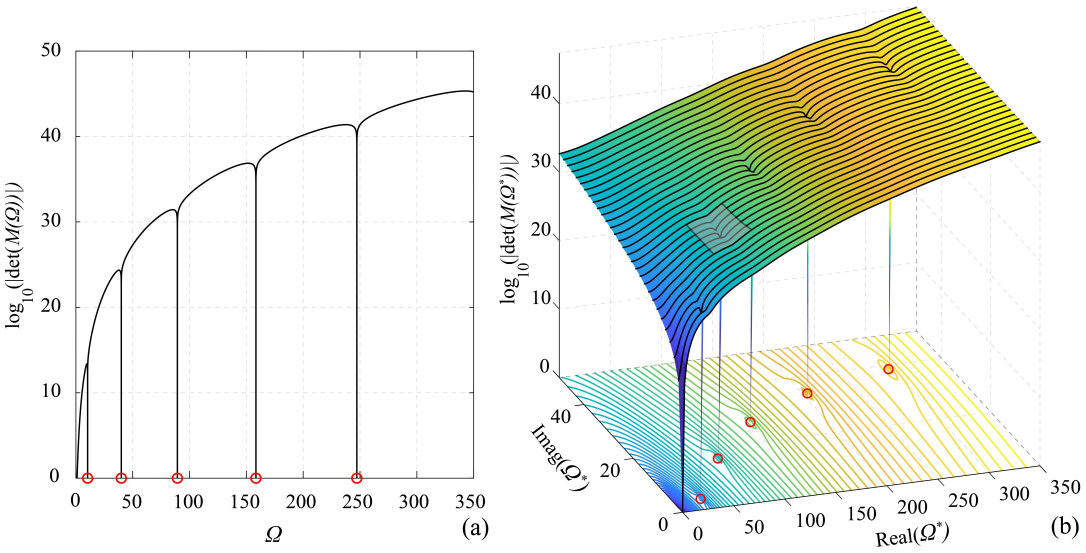

Figure 3.6: Zeros of determinant functions.(a) for $\eta_{2,ve} = 0$. (b) for $\eta_{2,ve} = 1$.

Figure 3.6.(a) represents this function for a sandwich beam with an elastic core in which $\eta_{2,ve} = 0$. This means that the circular natural frequencies of this beam have to be real numbers as the core does not provide additional damping and so, $\eta_n = 0$ and $\Omega_n^* = \Omega_n$. In this case, the function $\det(M(\Omega))$ is of type $\mathbb{R} \to \mathbb{C}$ (as the inputted frequencies are real numbers but the output determinant is complex K_i^* might be complex). In this case,

the modulus of the determinant complex number, $|\det(M(\Omega))|$, which is a real number can be used. This simplifies substantially the root-finding problem as now, a $\mathbb{R} \rightarrow \mathbb{R}$ function is analyzed. The application of the secant method can be used to find these roots. The vertical axis is on a logarithmic scale as the value of the determinant module increases considerably fast when increasing the value of Ω.

Figure 3.6.(b) represents the same function for a sandwich beam with a VE core with $\eta_{2,ve} = 1$. Now Ω_n^* is a complex number so the root-finding has to be performed in the complex plane. In this case $\det(M(\Omega^*))$ is $\mathbb{C} \rightarrow \mathbb{C}$ function. Figure 3.6.(b) depicts the module of the determinant as an image of the real and imaginary parts of the complex input frequency Ω^*. In this case, a complex-valued root-finding technique has to be used to find Ω_n^*. The one used here is the so-called Muller's method.

Muller's Method for finding complex roots

This section is devoted to conceptually explaining Muller's method which is valid for finding complex roots. For that, Figure 3.7 has been included. There, Muller's method is applied to find one of the roots of an example polynomial function.

The simplest iterative method to be used for that purpose is the so-called secant method, depicted in Figure 3.7.(a). This method requires two starting guess points close to the searched root with x coordinates x_0 and x_1. A straight line connecting them is developed and its zero is searched. This zero will be the point x_0 for the next iteration and the previous x_0 will become x_1. This process is repeated until it converges to a zero as represented in Figure 3.7.(a) with lines that change from lighter to darker colours. The secant method is useful, however is only valid for finding real roots.

Muller's method works similarly but instead of using straight lines makes use of parabolas so three points x_0, x_1 and x_2 are needed per iteration. An example of this is given in Figure 3.7.(b) (Figure 3.7.(c) represented the same image but in absolute value and in Figure 3.7.(d) the vertical axis is in logarithmic scale). The parabolas used in Figure 3.7.(b) have real zeros, nevertheless, it is widely known that parabolas may have complex zeros, and for that reason, Muller's method is also valid for finding complex roots. For further understanding of how this works, the function and the parabolas treated in this example have been represented over the complex plane in Figure 3.7.(e). Finally, Figure 3.7.(f) provides a real example of different complex parabolas used to finally converge to the second root of the function $\det(M(\Omega^*))$ highlighted in Figure 3.6.(b).

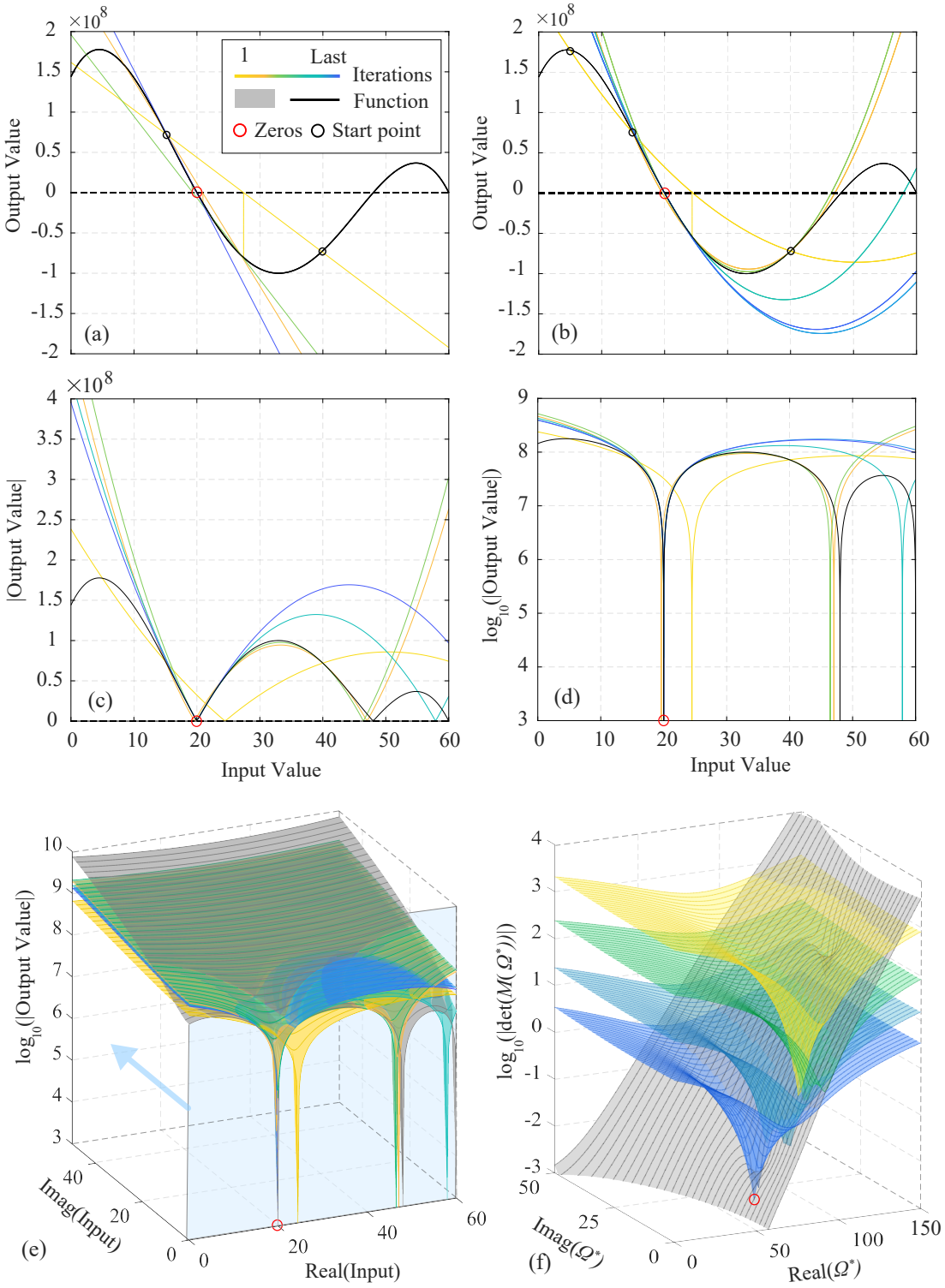

Figure 3.7: (a) Secant Method. (b) Muller's method for real roots. (c) Absolute value Muller's method. (d) Absolute value in logarithmic scale Muller's method. (e) Muller's method in the complex plane. (f) Muller's method iterations to find the second root of the determinant function.

In this thesis, an algorithm that uses Muller's method has been developed to find a given number of roots of the determinantal equation 3.46, and thus, the complex natural frequencies of a given sandwich beam. The methodology is divided into three steps:

- Step 1: An initial exploration of an undamped beam. Prior to the complex root-finding, the determinantal function of the same sandwich beam but with $\eta = 0$ is explored. This enables approximating the real values of the complex roots to be searched.
- Step 2: Complex root-finding. For each real root obtained in the previous step, a complex zero is searched. For that, three starting guess points with increasing imaginary coordinates are proposed for applying Muller's method.
- Step 3: Managing erroneous or repeated convergence. When applying Muller's method, three possible scenarios apart from a successful convergence might occur. i) a wrong convergence to the trivial zero $\Omega^* = 0$, ii) a repeated convergence into a previous root already detected, and iii) an erroneous convergence to a zero with a negative imaginary coordinate and with no modal meaning. When such a possibility occurs, the initial guess points are slightly changed and Muller's method is re-run till achieving a right convergence.

The use of this algorithm is illustrated in Figure 3.8, which displays the various iterations undertaken to find the roots of the function depicted earlier in Figure 3.6(b).

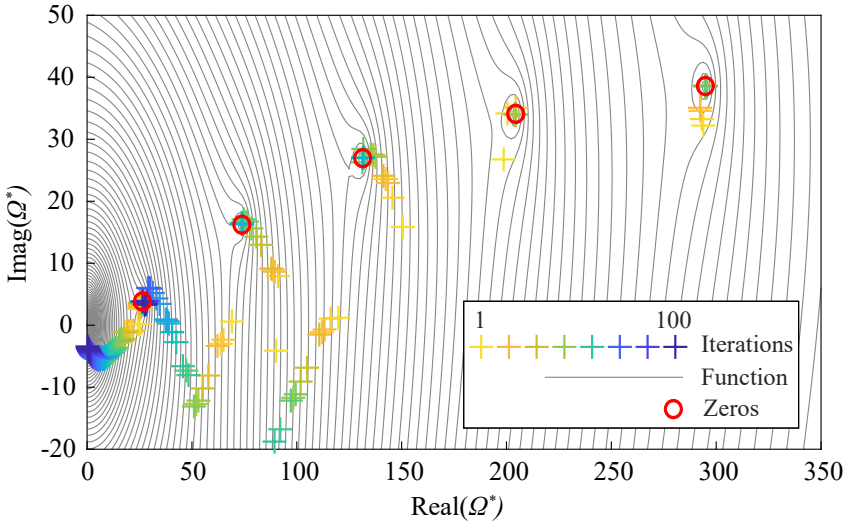

Figure 3.8: Application of root-finding algorithm

3.4 Partially treated sandwich beams

The formulation introduced up to now is valid for modelling sandwich beams with a VE layer applied along their whole length. Nevertheless, this thesis is focused on assessing the effectiveness of CLD treatments applied only for a proportion of the beam's length near the supports, such as the one depicted in Figure 1.5. Exact solutions for the modal properties of these partially treated sandwich beams can be obtained by solving the PDE in three segments.

Figure 3.9 depicts a beam divided into three segments a, b and c with respective lengths L_a, L_b and L_c. The edge ones, a and c, have a VE soft core while the central one, the b, has a rigid elastic core that connects the face layers to longitudinal shear. Assuming that the analyzed beam is symmetric and that the VE core extends along a proportion p of the beam length, the following relation stays true:

$$p = \left(\frac{2L_a}{L_b} \right) \tag{3.50}$$

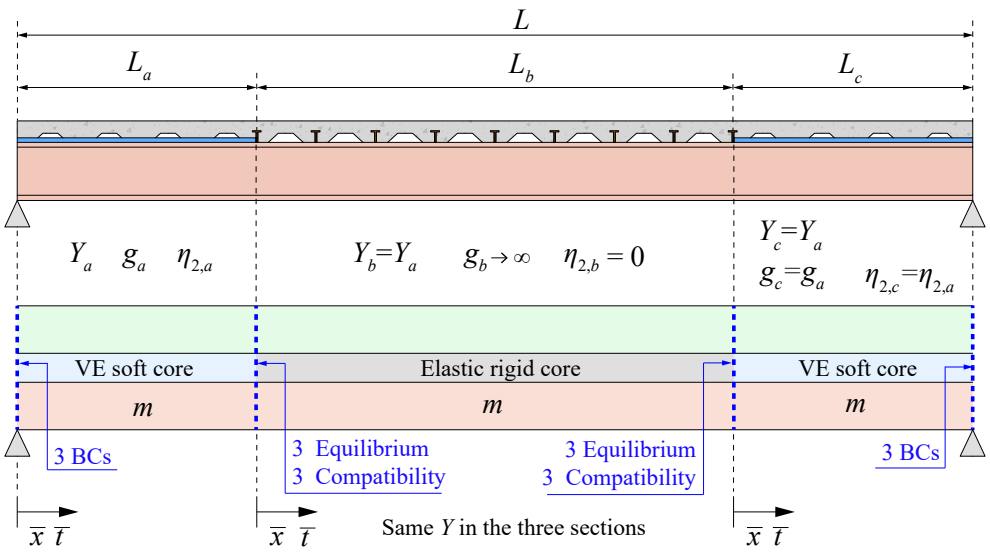

Figure 3.9: Partially treated sandwich beam divided into three segments, two edge segments treated with a VE core, and a central one with an elastic rigid core.

Within each segment, the PDE previously explained governs the bending motion of the segment. The same dimensionless coordinates $\bar{x}$ and $\bar{t}$ are used in each segment. Additionally, the three segments have the same geometric parameter Y as the elastic face

layers do not change and the same mass per unit of length m. However, this does not apply to the shear parameter g^*. Segments a and c display the same VE treatment, thus, $g_a = g_c$ and $\eta_{2,a} = \eta_{2,c}$. Segment b displays an elastic longitudinal shear connection in which g_b tends to infinity and $\eta_{2,b}$ is equal to zero.

When facing the modal solution of such the segmental beam, a different solution (w_a, w_b and w_c) has to be assumed for each segment of the beam. As before, they can be obtained according to the following expressions.

$$w_a = \left(\sum_{i=1}^{6} A^*_{a,j} \; e^{K^*_{a,j}\bar{x}} \right) e^{\Omega^* \bar{t}} = 0 \tag{3.51a}$$

$$w_b = \left(\sum_{i=1}^{6} A^*_{b,j} \; e^{K^*_{b,j}\bar{x}} \right) e^{\Omega^* \bar{t}} = 0 \tag{3.51b}$$

$$w_c = \left(\sum_{i=1}^{6} A^*_{c,j} \; e^{K^*_{c,j}\bar{x}} \right) e^{\Omega^* \bar{t}} = 0 \tag{3.51c}$$

Consequently, the free-vibration solution of the three-segment beam depends on eighteen constants, six $A^*_{a,j}$, six $A^*_{b,j}$ and six $A^*_{c,j}$. Thus, a determinantal equation depending on Ω^* can be derived from a system of 18 equations as the following one derived for a simply-supported beam

$$w_a(\bar{x} = 0) = 0 \tag{3.52a}$$

$$M_a(\bar{x} = 0) = 0 \tag{3.52b}$$

$$N_a(\bar{x} = 0) = 0 \tag{3.52c}$$

$$w_a(\bar{x} = p/2) = w_b(\bar{x} = 0) \tag{3.52d}$$

$$\phi_a(\bar{x} = p/2) = \phi_b(\bar{x} = 0) \tag{3.52e}$$

$$u_a(\bar{x} = p/2) = u_b(\bar{x} = 0) \tag{3.52f}$$

$$Q_a(\bar{x} = p/2) = Q_b(\bar{x} = 0) \tag{3.52g}$$

$$M_a(\bar{x} = p/2) = M_b(\bar{x} = 0) \tag{3.52h}$$

$$N_a(\bar{x} = p/2) = N_b(\bar{x} = 0) \tag{3.52i}$$

$$w_b(\bar{x} = 1 - p) = w_c(\bar{x} = 0) \tag{3.52j}$$

$$\phi_b(\bar{x} = 1 - p) = \phi_c(\bar{x} = 0) \tag{3.52k}$$

$$u_b(\bar{x} = 1 - p) = u_c(\bar{x} = 0) \tag{3.52l}$$

$$Q_b(\bar{x} = 1 - p) = Q_c(\bar{x} = 0) \tag{3.52m}$$

$$M_b(\bar{x} = 1 - p) = M_c(\bar{x} = 0) \tag{3.52n}$$

$$N_b(\bar{x} = 1 - p) = N_c(\bar{x} = 0) \tag{3.52o}$$

$$w_c(\bar{x} = p/2) = 0 \tag{3.52p}$$

$$M_c(\bar{x} = p/2) = 0 \tag{3.52q}$$

$$N_c(\bar{x} = p/2) = 0 \tag{3.52r}$$

This system emerges from imposing the BCs at the edges of the beam (Equations 3.52 a, b, c and p, q, r), the compatibility equations (3.52 d, e, f and j, k, l) and the equilibrium equations (3.52 g, h, i and m, n, o) at the interface sections between segments a-b and b-c.

$$\begin{bmatrix} \blacksquare & \blacksquare & \blacksquare & \blacksquare & \blacksquare & \blacksquare & 0 & 0 & 0 & 0 & 0 & 0 & 0 & 0 & 0 & 0 & 0 & 0 \\ \blacksquare & \blacksquare & \blacksquare & \blacksquare & \blacksquare & \blacksquare & 0 & 0 & 0 & 0 & 0 & 0 & 0 & 0 & 0 & 0 & 0 & 0 \\ \blacksquare & \blacksquare & \blacksquare & \blacksquare & \blacksquare & \blacksquare & 0 & 0 & 0 & 0 & 0 & 0 & 0 & 0 & 0 & 0 & 0 & 0 \\ \blacksquare & \blacksquare & \blacksquare & \blacksquare & \blacksquare & \blacksquare & \blacksquare & \blacksquare & \blacksquare & \blacksquare & \blacksquare & \blacksquare & 0 & 0 & 0 & 0 & 0 & 0 \\ \blacksquare & \blacksquare & \blacksquare & \blacksquare & \blacksquare & \blacksquare & \blacksquare & \blacksquare & \blacksquare & \blacksquare & \blacksquare & \blacksquare & 0 & 0 & 0 & 0 & 0 & 0 \\ \blacksquare & \blacksquare & \blacksquare & \blacksquare & \blacksquare & \blacksquare & \blacksquare & \blacksquare & \blacksquare & \blacksquare & \blacksquare & \blacksquare & 0 & 0 & 0 & 0 & 0 & 0 \\ \blacksquare & \blacksquare & \blacksquare & \blacksquare & \blacksquare & \blacksquare & \blacksquare & \blacksquare & \blacksquare & \blacksquare & \blacksquare & \blacksquare & 0 & 0 & 0 & 0 & 0 & 0 \\ \blacksquare & \blacksquare & \blacksquare & \blacksquare & \blacksquare & \blacksquare & \blacksquare & \blacksquare & \blacksquare & \blacksquare & \blacksquare & \blacksquare & 0 & 0 & 0 & 0 & 0 & 0 \\ \blacksquare & \blacksquare & \blacksquare & \blacksquare & \blacksquare & \blacksquare & \blacksquare & \blacksquare & \blacksquare & \blacksquare & \blacksquare & \blacksquare & 0 & 0 & 0 & 0 & 0 & 0 \\ 0 & 0 & 0 & 0 & 0 & 0 & \blacksquare & \blacksquare & \blacksquare & \blacksquare & \blacksquare & \blacksquare & \blacksquare & \blacksquare & \blacksquare & \blacksquare & \blacksquare & \blacksquare \\ 0 & 0 & 0 & 0 & 0 & 0 & \blacksquare & \blacksquare & \blacksquare & \blacksquare & \blacksquare & \blacksquare & \blacksquare & \blacksquare & \blacksquare & \blacksquare & \blacksquare & \blacksquare \\ 0 & 0 & 0 & 0 & 0 & 0 & \blacksquare & \blacksquare & \blacksquare & \blacksquare & \blacksquare & \blacksquare & \blacksquare & \blacksquare & \blacksquare & \blacksquare & \blacksquare & \blacksquare \\ 0 & 0 & 0 & 0 & 0 & 0 & \blacksquare & \blacksquare & \blacksquare & \blacksquare & \blacksquare & \blacksquare & \blacksquare & \blacksquare & \blacksquare & \blacksquare & \blacksquare & \blacksquare \\ 0 & 0 & 0 & 0 & 0 & 0 & \blacksquare & \blacksquare & \blacksquare & \blacksquare & \blacksquare & \blacksquare & \blacksquare & \blacksquare & \blacksquare & \blacksquare & \blacksquare & \blacksquare \\ 0 & 0 & 0 & 0 & 0 & 0 & \blacksquare & \blacksquare & \blacksquare & \blacksquare & \blacksquare & \blacksquare & \blacksquare & \blacksquare & \blacksquare & \blacksquare & \blacksquare & \blacksquare \\ 0 & 0 & 0 & 0 & 0 & 0 & 0 & 0 & 0 & 0 & 0 & 0 & \blacksquare & \blacksquare & \blacksquare & \blacksquare & \blacksquare & \blacksquare \\ 0 & 0 & 0 & 0 & 0 & 0 & 0 & 0 & 0 & 0 & 0 & 0 & \blacksquare & \blacksquare & \blacksquare & \blacksquare & \blacksquare & \blacksquare \\ 0 & 0 & 0 & 0 & 0 & 0 & 0 & 0 & 0 & 0 & 0 & 0 & \blacksquare & \blacksquare & \blacksquare & \blacksquare & \blacksquare & \blacksquare \end{bmatrix} \begin{bmatrix} A^*_{a,1} \\ A^*_{a,2} \\ A^*_{a,3} \\ A^*_{a,4} \\ A^*_{a,5} \\ A^*_{a,6} \\ A^*_{b,1} \\ A^*_{b,2} \\ A^*_{b,3} \\ A^*_{b,4} \\ A^*_{b,5} \\ A^*_{b,6} \\ A^*_{c,1} \\ A^*_{c,2} \\ A^*_{c,3} \\ A^*_{c,4} \\ A^*_{c,5} \\ A^*_{c,6} \end{bmatrix} = \begin{bmatrix} 0 \\ 0 \\ 0 \\ 0 \\ 0 \\ 0 \\ 0 \\ 0 \\ 0 \\ 0 \\ 0 \\ 0 \\ 0 \\ 0 \\ 0 \\ 0 \\ 0 \\ 0 \end{bmatrix} \tag{3.53}$$

where the blue squares are terms of the matrix related to segments a and c and grey ones are referred to as segment b.

The determinantal equation derived from this expression has to be solved with the iterative root-finding method previously explained. However, some numerical problems arise.

Numerical overflow problems when solving partially treated beams

When solving a partially treated beam, the central segment b displays a much higher $g_b = 10^7$ value than the other two segments where this parameter is around four orders of magnitude lower. Hence, some of the wave numbers corresponding to this segment, $K^*_{b,j}$, are much higher than those of sections a and c. This fact provokes some exponential terms of type $e^{K^*_{b,j}(1-p)}$ that belong to the expressions of $w_b(\bar{x} = 1 - p)$, $\phi_b(\bar{x} = 1 - p)$,

$u_b(\bar{x}=1-p)$, $Q_b(\bar{x}=1-p)$, $M_b(\bar{x}=1-p)$ and $N_b(\bar{x}=1-p)$ to be such big numbers that may produce numerical overflow problems. This means, that these numbers can not be well represented with 'double' 64-bit floating-point numbers.

The way of solving this problem is by saturating or limiting the value of $K^*_{b,j}$ when it plays the role of 'exponent' of these problematic terms. Consequently, only inside these exponent the value of $K^*_{b,j}$ is substituted by a lower value $\overline{K^*_{b,j}}$. An example of this is shown in the following expression:

$$M_b(\bar{x}=1-p)=\sum_{j=1}^{6} A^*_{b,j} e^{\overline{K^*_{b,j}}(1-p)}\left(K^{*4}_{b,j}-g^*_b(1+Y_b)K^{*2}_{b,j}+\Omega^{*2}\right) \tag{3.54}$$

This modification does not appreciably change the roots of the determinantal equation. This is shown in Figure 3.10 where for a particular case, the values of some $|K^*_{b,j}|$ round 200 and are saturated to 10 and the position of the roots is preserved.

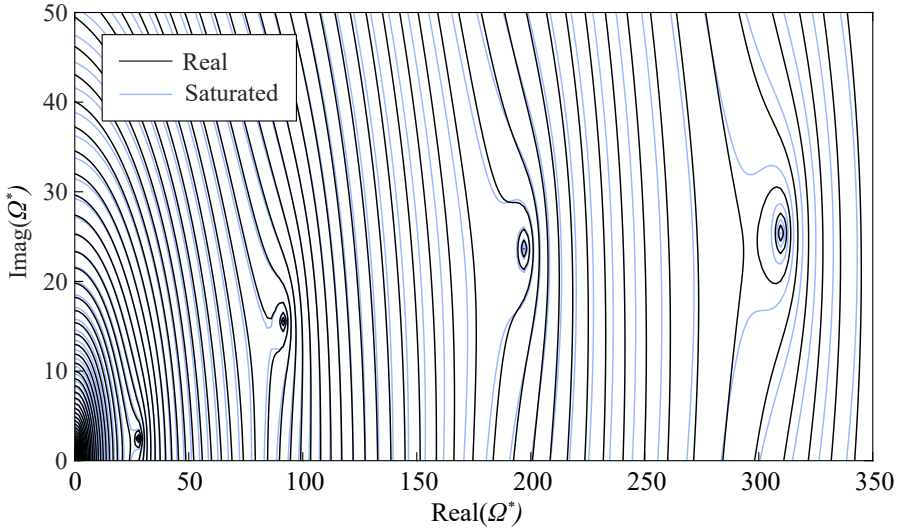

Figure 3.10: Difference between the real and the approximated determinantal function of a 50% treated sandwich beam assuming $|\overline{K^*_{b,j}}| \leq 10$.

3.5 Parametric analysis with the analytical model

The present section provides the first parametric analysis, to the author's knowledge, in which the proportion of beam length treated with VE core, p, is considered as parameter for the study. From now on, the percentage value related to a given value of p will be

called % CLD. Two main parametric studies have been performed:

1. The first one aims to achieve a general perspective of the dynamic behaviour of sandwich beams with a considerable dissipative VE core with $\eta_{2,ve} = 1$. Different values of Y, g and % CLD have been studied to assess their impact on the final modal solution of the first four vibration modes.

2. The second one has been focused on understanding the influence of the loss factor of the VE material on the final fundamental loss factor of the sandwich beam. Hence, the fundamental modal properties of different sandwich beams resulting from combining different values of Y, g, % CLD, and $\eta_{2,ve}$ have been studied.

3.5.1 Parametric study 1

Within this study the only defining variable of the sandwich beam kept constant has been $\eta_{2,ve}$ with a value equal to 1. The rest of the parameters have been varied. Each sandwich beam analyzed results by combining these parameters. The values studied for each variable are included below:

$$Y = [0.1, 1, 10] \tag{3.55a}$$

$$g = [0.01, ..., 100000] \quad \text{(35 values 10th-logarithmically spaced)} \tag{3.55b}$$

$$\%\ CLD = [10, 20, 30, 40, 50, 60, 70, 80, 90, 100] \tag{3.55c}$$

$$\text{BCs} = [\text{Pinned, Clamped riveted}] \tag{3.55d}$$

$$\eta_{2,ve} = 1 \tag{3.55e}$$

The results from this study are the modal parameters, Ω_n and η_n, of the first four vibration modes of the sandwich beams. These results for simply supported beams and encastred beams are respectively depicted in Figures 3.11 and 3.12. These figures consist of two 3-row x 4-column matrices of charts, one on top of the other. The top matrix with bell-shape charts provides the results of η_n, while the bottom one provides the results for Ω_n. Within the matrices, each row corresponds to a fixed Y value and each column to a given vibration mode n. Inside each chart, the corresponding modal parameter is studied as a function of the shear stiffness of the VE core by varying g along the horizontal axis and considering ten different values of % CLD, one per each curve plotted.

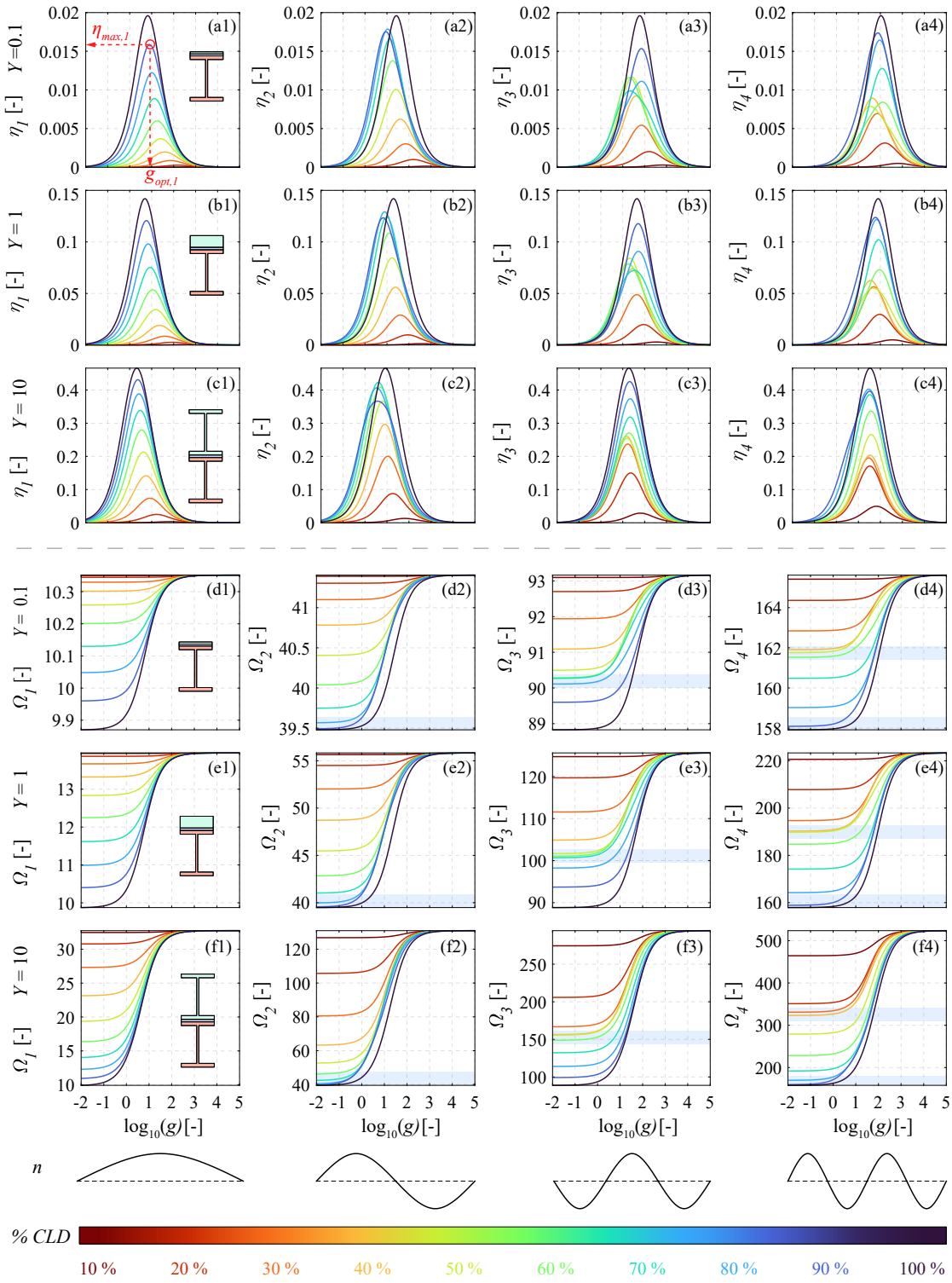

Figure 3.11: Modal parameters Ω_n and η_n of the first four vibration modes for Simply-supported beams with pinned BCs, obtained from parametric study 1.

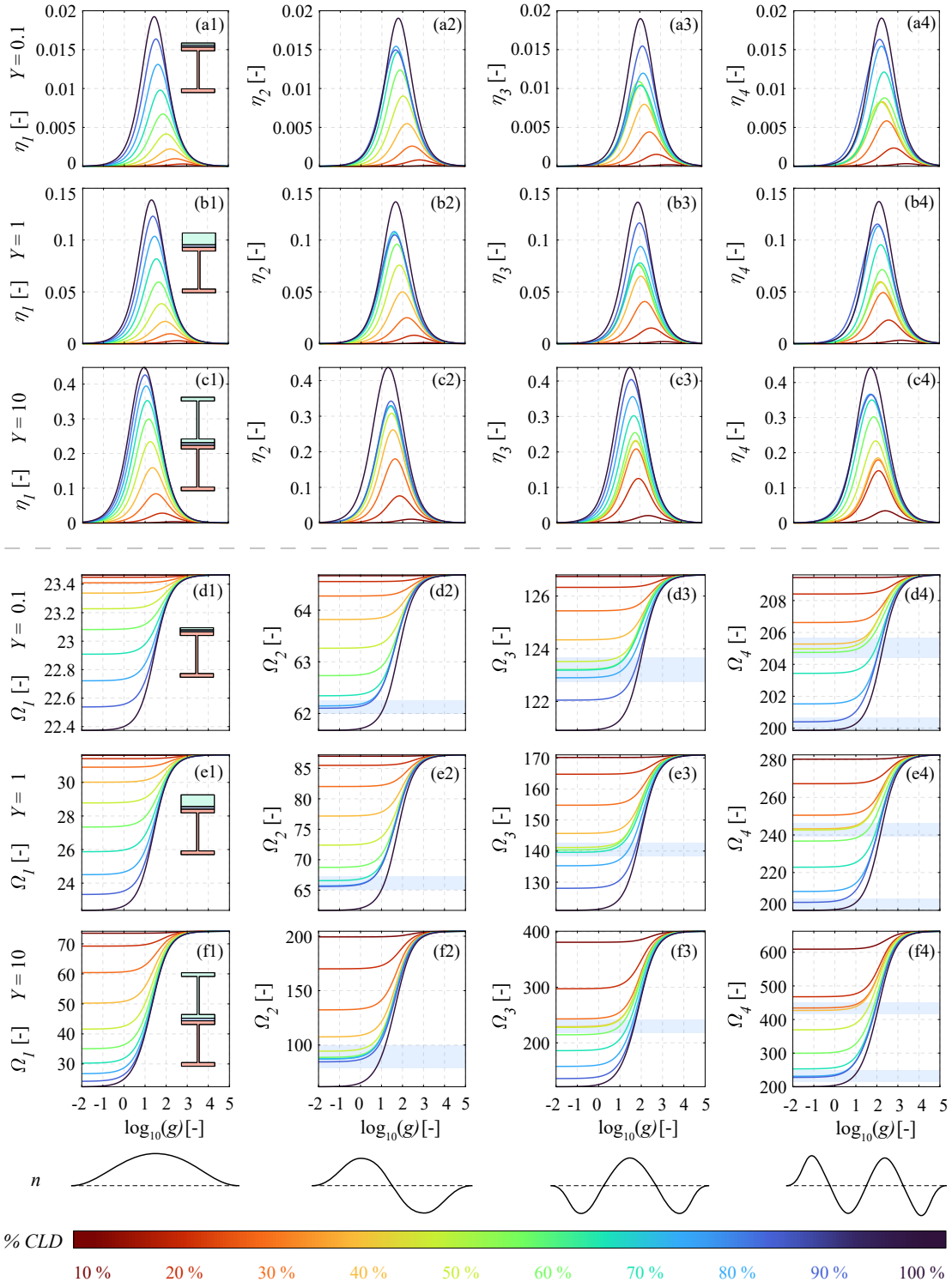

Figure 3.12: Modal parameters Ω_n and η_n of the first four vibration modes for encastred beams with clamped riveted BCs, obtained from parametric study 1.

In η_n charts it can be observed that each plotted line (representing a beam defined by a given combination of Y, $\%\ CLD$ and $\eta_{2,ve} = 1$) has an optimum value of the shear parameter $g_{opt,n}$ that provides the maximum loss factor $\eta_{max,n}$ (as indicated in Figure 3.11.(a1)). A summary of these $\eta_{max,n}$ and $g_{opt,n}$ values is provided in Figure 3.13 as a function of $\%\ CLD$.

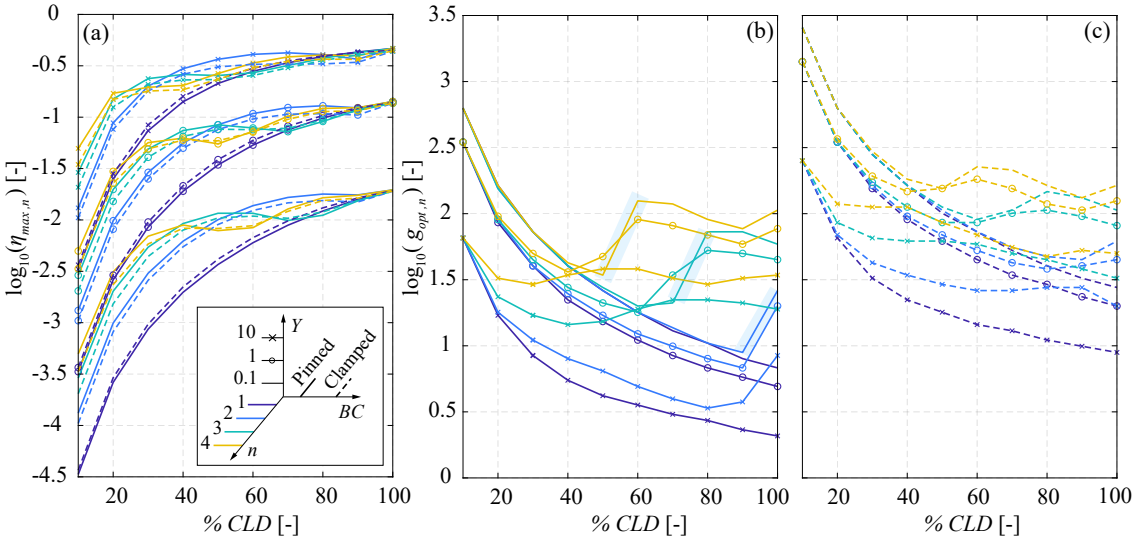

Figure 3.13: Summary of $\eta_{max,n}$ and $g_{opt,n}$ for parametric study 1. (a) $\eta_{max,n}$. (b) $g_{opt,n}$ for simply supported beams. (c) $g_{opt,n}$ for encastred beams.

Parametric study 1: results discussion

From the results obtained in Parametric Study 1, the following conclusions may be extracted:

- Regarding the general aspect of the charts depicted in Figures 3.11 and 3.12 it is visible that the shapes of the η_n and Ω_n curves are similar within each mode of vibration (within each column), independently on the Y parameter. The BCs have more influence in this respect, this means that charts' shapes in Figure 3.11 differ from those of Figure 3.12. Additionally, focusing on the first vibration mode, in η_n charts it can be appreciated that the curves with higher $\%\ CLD$ are envelopes of those with a lower proportion of VE-treated length. This does not happen for higher vibration modes.

- In the Ω_n charts of Figures 3.11 and 3.12, it can be appreciated that for lower values of g, some curves with consecutive $\%\ CLD$ tend to be concentrated or

grouped. These groups have been highlighted in these figures with blue-shaded areas. Some patterns related to the location of these areas can be identified. Charts of the 2$^{\text{nd}}$ mode of vibration present this concentration in curves with 80, 90 and 100% CLD. In the 3$^{\text{rd}}$ mode of vibration this concentration happens between curves with 60, 70 and 80% CLD. Finally, the 4$^{\text{th}}$ one presents two concentrations, the first between 30, 40 and 50% CLD and the second one between 80, 90 and 100% CLD curves. This effect is caused by the nodal points of the modes of vibration. The presence of more or less bending stiffness in the surroundings of a nodal point does not severely influence the value of the natural frequency of that vibration mode. Hence, these concentrations occur between % CLD in which the frontier between the VE-treated and the shear-connected regions is close to a node of the vibration mode. Additionally, the nodes are those points of the vibration mode where the shear deformation of the VE core is greater. Thus, whenever an node changes from being shear-connected to be VE-treated, the loss factor curves tend to change their optimal $g_{opt,n}$. This is clearly visible in Figures 3.11.(a2) and (d2) between curves with 90 and 100% CLD.

- From the summary of results provided in Figure 3.13, the following conclusions may be extracted from sub-figure (a). First, it has been confirmed that for partially treated beams, the higher the Y, the higher the $\eta_{max,n}$ (this was already known for 100% CLD beams). Second, generally, for lower values of % CLD, the higher the order of the vibration mode, the higher the $\eta_{max,n}$. Third, it has been confirmed that the highest values of $\eta_{max,n}$ are always achieved with 100% CLD. Nevertheless, for higher modes than the first one, it can be seen that a higher % CLD does not always implies a higher value of $\eta_{max,n}$. Fourth, it is observed that encastred beams have similar or even higher values of $\eta_{max,n}$ than simply supported ones. Finally, It has been proved that for 100% CLD beams the value of $\eta_{max,n}$ is independent of the mode of vibration and of the BC used.

- From Figures 3.13.(c) the following findings have been revealed. First, for mode of vibration 1, the higher the % CLD the lower the value of $g_{opt,n}$, and for the next modes of vibration this is not met. Second, the higher the n, the greater the $g_{opt,n}$. Third, The BCs have a significant impact on $g_{opt,n}$ as their values are much higher for encastred beams than for simply-supported ones. Fourth, the 'jumps' experienced by $g_{opt,n}$ when changing the status of an nodal section from shear-connected to VE-treated, are much more patent on simply supported beams with lower Y values (these have been highlighted with blue shaded areas on Figure 3.13.(b))

- A final important conclusion may be extracted from this study. One might think that CLD treatments provide a great amount of damping to many modes of vibration at the same time, however, this is not true. Each mode of vibration is related to an optimum configuration of the VE layer. Hence, a treatment designed to damp a particular mode of vibration might not work to damp another mode. Generally, the higher the difference in the modal order of two modes, the higher the difference in their $g_{opt,n}$. This effect becomes more severe for encastred beams and for higher Y values.

3.5.2 Parametric study 2

Once the general mechanical behaviour of partially treated beams has been analyzed, a second and more detailed parametric study is here presented. This one is focused just on the first mode of vibration (as this one is the main responsible for floor vibrations on floor buildings). Additionally, different values of $\eta_{2,ve}$ have been studied to see their influence on the final values of damping. The different parameters studied are included below:

$$Y = [0.1, 1, 10] \tag{3.56a}$$

$$g = [0.01, ..., 100000] \quad \text{(35 values 10th-logarithmically spaced)} \tag{3.56b}$$

$$\%\ CLD = [10, 20, 30, 40, 50, 60, 70, 80, 90, 100] \tag{3.56c}$$

$$\text{BCs} = [\text{Pinned}] \tag{3.56d}$$

$$\eta_{2,ve} = [0.01, 0.1, 1, 10] \tag{3.56e}$$

In this case, the only results provided from this study are the values of η_1. The values of Ω_1 are similar to those depicted in the first column of the bottom matrix of charts shown in Figure 3.11. The results for η_1 are illustrated in Figure 3.14 on a 3-rows x 4-columns matrix of charts. Now, each row provides a value of Y and each column represents a value of $\eta_{2,ve}$. Each chart has ten curves, each one representing a given $\%\ CLD$. As before, the results are plotted as a function of g.

Again, the optimal points of each curve have been summarized in Figure 3.15 as a function of the $\%\ CLD$. Sub-figure (a) depicts the values of $\eta_{max,1}$ and sub-figure (b) the values of $g_{opt,1}$. Sub-figure (c), however, provides a representation of the variation of $\eta_{max,1}$ as a function of $\eta_{2,ve}$.

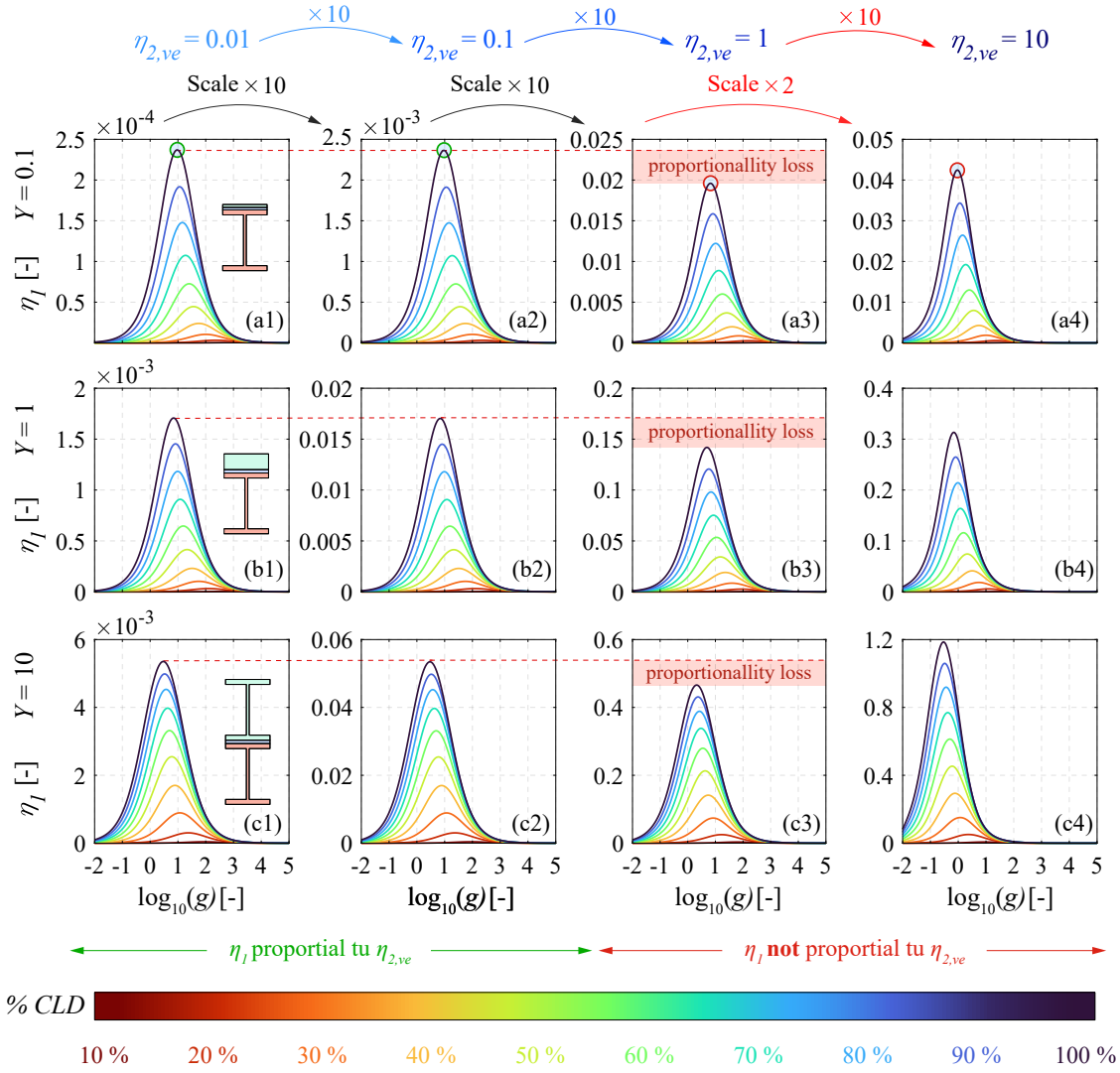

Figure 3.14: Loss factor of the first mode of vibration, η_1, of simply-supported sandwich beams with different Y and $\eta_{2,ve}$ values, obtained from parametric study 2.

Parametric study 2: results discussion

Analyzing the results of the parametric study 2, the following conclusions can be outlined:

- From Figure 3.14, it can be concluded that the shapes of the loss factor curves shown in the different charts are quite similar independently on the values of $\eta_{2,ve}$ or Y.
- Within each row of charts depicted in Figure 3.14 it can be appreciated that the increase of η_1 is not linear with the increase of $\eta_{2,ve}$. In fact, for lower values of $\eta_{2,ve}$ this change is linear, nevertheless this proportionality is lost for higher values

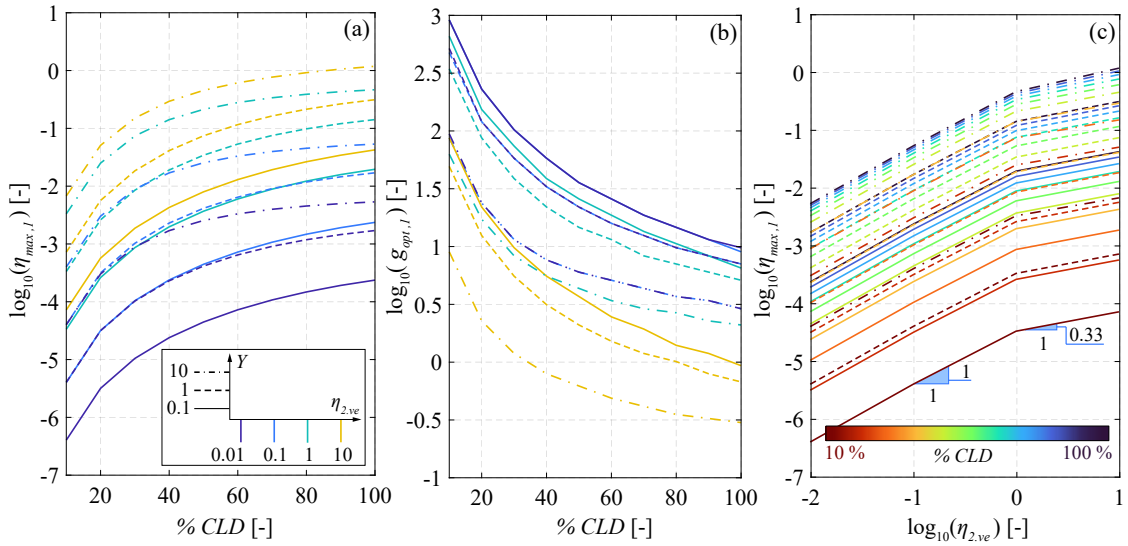

Figure 3.15: Summary of $\eta_{max,1}$ and $g_{opt,1}$ for parametric study 2. (a) $\eta_{max,1}$ as a function of % CLD. (b) $g_{opt,1}$ as a function of % CLD. (c) $\eta_{max,1}$ as a function of $\eta_{2,ve}$.

of $\eta_{2,ve}$. For example, between Figures 3.14.(a1) and (a2), $\eta_{2,ve}$ is multiplied by a factor of 10 (from 0.01 to 0.1), and consequently the maximum values of $\eta_{max,1}$ for the 100% CLD also increase by a factor of 10 (from 2.3x10^{-4} to 2.3x10^{-3}). This does not occur between Figures 3.14.(a3) and (a4) where $\eta_{2,ve}$ changes from 1 to 10 and the maximum η_1 just increases by a factor of 2 from 0.02 to 0.04. This effect is clearly noticeable in Figure 3.15.(c), where for the different cases studied $\eta_{max,1}$ has been represented as a function of $\eta_{2,ve}$. As both values are in logarithmic way, the slopes of the different cases (almost parallel between each other) represent the exponent b of a curve $\eta_{max,1} = 10^a(\eta_{2,ve})^b$. In the Figure, it can be seen how the initial value of b is close to 1, and then, it changes to approximately 0.3.

- The results depicted in 3.15.(a) allow inferring the following two statements. First, the higher the % CLD the higher the $\eta_{max,1}$, and second, the higher the Y the higher the $\eta_{max,1}$, but its rate of increase is decreasing for higher % CLD values.

- Finally, the following outcomes can be extracted from Figure 3.15.(b). First, again, the higher the % CLD the lower the $g_{opt,1}$. Second, the higher the Y, the lower the $g_{opt,1}$. And third, the value of $\eta_{2,ve}$ influences the values of $g_{opt,1}$. For lower values of $\eta_{2,ve}$, this influence is almost negligible, however, the higher the value of $\eta_{2,ve}$ the lower the $g_{opt,1}$ and the higher its rate of change.

3.6 Conclusions

This Chapter has provided a deep analysis of the mechanical and dynamic behaviour of sandwich beams with a VE core analytically modelled by means of PDEs. For the first time, the analytical solution of partially-treated sandwich beams has been covered, and an iterative algorithm based on Muller's method has been proposed to obtain its exact solutions. Additionally, a remedial to address numerical overflow problems typically arising when solving determinantal equations, has been provided. Finally, the study of partially-treated sandwich beams has been faced by developing two parametric studies. With the first one, a general insight on the modal parameters of the first four modes of vibration has been covered. The second study, which has been focused on the fundamental vibration mode, has confirmed the strong non-linear dependency of the fundamental modal parameters with respect to $\eta_{2,ve}$.

4

CLD modelling: Numerical FE models

4.1 Introduction

This Chapter is a continuation of Chapter 3, moving on from the above-studied analytical models through numerical models. The objective of the Chapter is the same one as before: to study the implementation of these models, more specifically, those based on FE analysis, for predicting the additional damping ratio provided by the CLD treatments applied in composite floor beams.

For CLD treatments to be extensively used in composite floor construction it is essential to come up with a reliable and manageable way of predicting the additional damping ratio they can provide [168]. As has been already seen in Chapter 3, many authors, like Ross, Ungar, and Kerwin or DiTaranto have proposed different analytical models and even solutions to these models. Some authors who have previously studied the implementation of CLD treatments on composite floor systems as, Farah *et al.* [158] and Zegers [169] have used similar analytical formulations. These authors studied both retrofitting solutions and CLD treatments similar to *"Resotec"* applied along the whole length of the floors' beam, in 100% CLD layout. Later, Willford *et al.* from ARUP, claimed to have used a model based on the one proposed by Ross, Ungar, and Kerwin

for studying partially CLD-treated beams, of the type 50% CLD. Nonetheless, they did not deepen on the model they used which would probably be an FE model, as at that time, the software company *'Oasys'* (known as *'the software house of ARUP'*) started to offer the capability of analysing partially CLD-treated composite floors inside its module 'Compos'. Again, the 'Compos' user guide does not offer further information on how this damping prediction is done.

The idea of predicting the damping capacity of CLD treatments through using FE modelling has been previously explored by some authors. Some of them, as Ahmadi *et al.* [160] or Antar [170] have opted for detailed models where the VE layer is represented with solid elements with VE constitutive behaviour and solved with CMA. This type of approaches are complex and do not encourage civil engineers to use the CLD technology. In this context, the present Chapter aims to provide a simplified and practitioner-focused FE modelling methodology based on two important characteristics, i) the use of simple elements such as springs for the VE layer, and ii) real modal analysis. This simple methodology proposed, has been validated through rigorous comparison of its results for a 100% CLD benchmark beam with two widely accepted modelling approaches, namely: i) a detailed FE model of the CLD treatment solved with CMA, and ii) the analytical solution of Rao [166] described in Chapter 3 on the Equation 3.48. After this, the proposed methodology has been also validated to model partially treated beams, comparing it with the detailed FE model. For that, a parametric analysis with different beam lengths and % CLD has been carried out. Thirdly, the results obtained in this parametric analysis have been used to assess the dynamic performance of single-spanning composite floors partially treated with CLD.

The remainder of this Chapter is organized as follows: Section 2 describes a 100% CLD benchmark composite beam used for a first validation. Section 3 describes the different types of models and types of analyses used to assess this benchmark beam, and compares the results obtained with each modelling approach studied. Section 4 describes the parametric analysis developed to validate the proposed modelling approach for partially treated beams. Section 5 studies as an example of application, the dynamic performance of single-spanning composite floors made with partially treated beams. Finally, Section 6 provides some conclusions.

4.2 Benchmark floor beam

4.2.1 Geometry of the benchmark floor beam

The benchmark example used for comparing the modelling approaches is a simply supported secondary floor beam with a 100% CLD treatment. The beam has a length of 12 m and makes use of a UB 457X191X67 steel profile combined with a rib-deck for the concrete slab ALX1.2 mm of gauge (from Richard Lee Steel Decking). The total height of the concrete slab is 130 mm and its width b_c is 2.30 m. The CLD treatment applied consists of two steel sheets of 1 mm thickness comprising a 1 mm VE layer in the middle. The width of the treatment is the same as the one of the steel profile flange, 191 mm.

4.2.2 Constitutive model

This Chapter deals with the dynamic structural analysis of floor beams in serviceability conditions. For that, both concrete and steel are modelled as elastic materials. The steel has been modelled with a Young modulus E_s=210 GPa, a Poisson modulus ν_s=0.3 and a density ρ_s=7850 kg/m^3. The concrete has been defined with the following properties, E_c=30 GPa, ν_c=0.2 and ρ_c=2500 kg/m^3.

In this Chapter, the VE material of the CLD is defined through $G_2^{'}$ and $\eta_{2,ve}$. These magnitudes can be considered to be constant along the frequency band of interest.The value of $\eta_{2,ve}$ has been assumed to be constant and equal to 1, however, the value of G_2' has been varied along the whole set of studies performed in the study, in order to develop curves relating the additional damping provided by the CLD treatment in terms of the shear parameter of the beam g as done in Figure 3.11.(a) to (c). Typical values of G_2' for VE materials used in these kind of CLD treatments are around 0.5 to 2 MPa within the low-frequency band between 3 to 10 Hz, as will be later explained in Chapter 5, when describinf the VE material used on the experimental tests of the thesis[171]. Finally, the Poisson coefficient assumed for this material ν_2 has been set to 0.49 (a typical value for an elastomeric material used for these types of damping applications) [172].

4.3 Modelling approaches

The term "modelling approach" is used in this study to define the combination of two elements, i) a type of model and ii) a type of modal analysis performed on the model. 3 types of models and 3 types of analysis are described in this section. All of them will be combined defining 3 x 3 = 9 different modelling approaches that will be compared between each other. The objective of this comparison is to validate the accuracy of one modelling approach proposed by the author as a simplified option to be used for the design of composite floors with integrated CLD treatments.

4.3.1 Types of Models

Model 1: Detailed FE model

This first detailed model has been considered to be the reference for comparison in terms of accuracy, as the geometry has been precisely modelled. The FE modelling presented in this Section has been performed in ANSYS Mechanical APDL.

As has been illustrated in Figure 4.1.(a), the concrete slab has been modelled with SOLID185 elements using one element along its thickness. The steel rib-deck used for the slab has been modelled with SHELL181 elements rigidly connected to the concrete slab, node by node. The steel beam is defined using SHELL181 elements and a positive offset equal to half of the flange thickness has been used for the elements of the profile's upper flange. Finally, the CLD treatment has been defined using SHELL181 elements for its thin constraining steel sheets, and SOLID185 elements for the VE layer, using only one element along its thickness. The lower constraining steel sheet of the CLD has not been included in the model as its influence is negligible. Additionally, the upper and lower surfaces of the CLD treatment have been rigidly connected to the concrete slab and the steel beam, respectively.

Three main aspects of this model must be highlighted. First, a constraint linear equation has been defined between the top and bottom nodes of the VE layer at any beam section, so they have the same vertical displacement. Second, the upper constraining layer of the CLD treatment (depicted with green colour in Figure 4.1.(a)) need to be included, as it allows transferring the shear deformation of the VE layer within the rib-deck valleys, where the slab is not directly in contact with the CLD treatment (Figure 4.1.(b)). Third,

the length-to-height aspect ratio (AR) of the SOLID185 elements used to model the VE layer (Figure 4.1.(c)), and the number of these elements included along its thickness have been analyzed. A sensitivity analysis varying this AR was carried out proving that these parameters do not influence significantly the results obtained. After all, an AR of around 100 was finally used in the model.

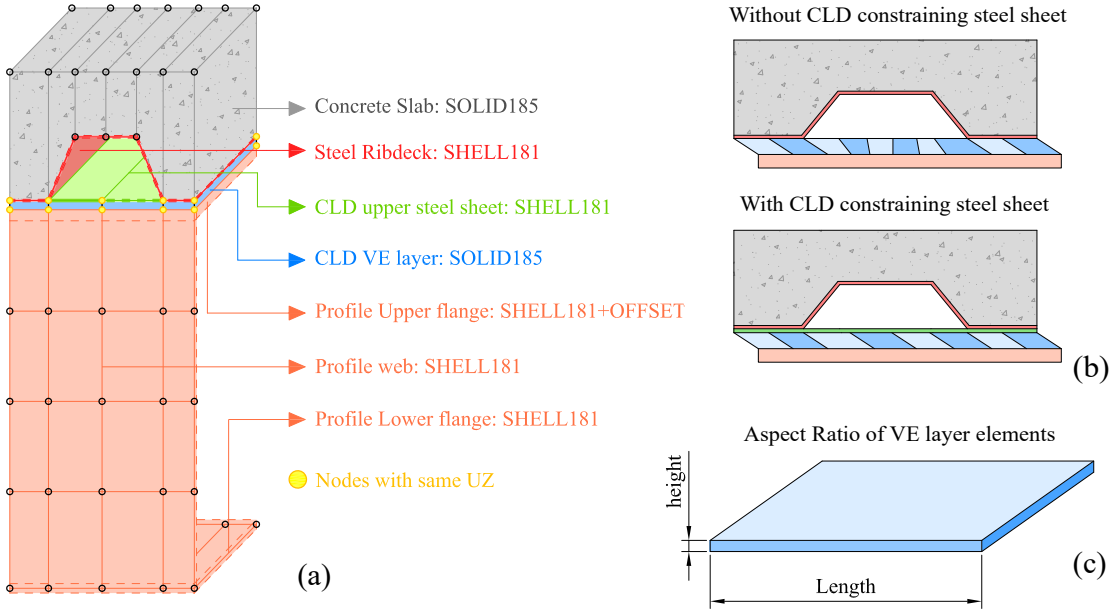

Figure 4.1: Model 1. Detailed FE model with SOLID185 and SHELL181 elements.

Model 2: Simplified FE model

This second model has been proposed as a simplified approach to model the dynamic behaviour of a floor sandwich beam with BEAM, SHELL and SPRING elements. The modelling approach is here described in 4 Steps, and is graphically represented in Figure 4.3:

- *Step 1: Steel profile modelling.*

  The steel profile is modelled with Euler-Bernoulli first-order BEAM elements, particularly, the author used BEAM188 from ANSYS. A positive offset equal to half of the profile's height $h_s/2$ is given to the profile's section, so the nodes are located at its top fibre (See Figure 4.3). A given element length L_{el} is adopted.

- *Step 2: Rib-deck slab modelling.*

The rib-deck concrete slab is modelled with SHELL elements including nodes just over the nodes of the profile. An equivalent constant-height slab (as the one depicted in Figure 4.2), which can be defined with four parameters, has been used.

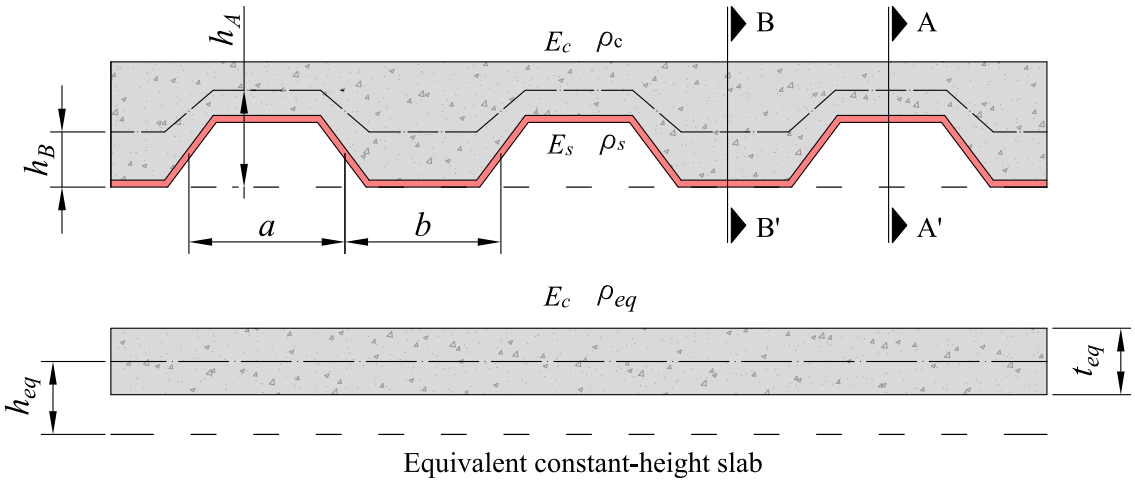

Figure 4.2: Equivalent constant-height concrete slab used in Model 2.

The equivalent parameters of the slab are obtained as follows [173]. First, the Young Modulus is considered to be equal to the concrete one, E_c. Second, by considering that the bending stiffness of both the real and the equivalent slab must be equal when simply-supported and subjected to a constant bending moment state, the equivalent height, t_{eq}, is computed as follows:

$$t_{eq} = \sqrt[3]{\frac{12(a+b)}{\left(\frac{a}{I_{hA}} + \frac{b}{I_{hB}}\right)}}, \tag{4.1}$$

where a and b are the distances depicted in Figure 4.2, and I_{hA} and I_{hB} are the moments of inertia of the concrete-homogenised sections A-A' and B-B' considering 1 m section width, respectively. Third, to ensure the same weight per m^2 (here named as w_{slab}), an equivalent density for the slab, ρ_{eq} is used,

$$\rho_{eq} = w_{slab}/t_{eq}. \tag{4.2}$$

Forth, the composite section made by the steel profile and the equivalent slab should have the same composite bending stiffness as the original one. This is achieved by adding a negative offset to the equivalent slab equal to h_{eq} and computed as the weighted average of h_A and h_B (distances from the original bottom fibre to the centroid of the sections A-A' and B-B', respectively) as follows:

$$h_{eq} = (a\ h_A + b\ h_B)/(a+b). \tag{4.3}$$

- *Step 3: VE layer modelling.*

  The VE layer is modelled by equivalent horizontal springs. COMBIN14 ANSYS elements have been used for the model. Each horizontal spring links one node of the steel profile with one node of the equivalent slab, as depicted in Figure 4.3. As the VE layer is very thin, the position of both nodes could be assumed to be coincident. The stiffness of each horizontal spring, k_{eqX}, is proposed to be computed as follows:

$$k_{eqX} = \frac{G_2'\ L_{el}\ b_2}{h_2}, \tag{4.4}$$

  where b_2 and h_2 are the width and the thickness of the VE layer and G_2' is the assumed shear modulus for the VE material which will vary depending on the type of analysis performed with the model.

- *Step 4: Couple vertical displacement of profile and slab.*

  For the same reason above-mentioned, a constraint linear equation is also included in this model to equate the vertical displacements of both the slab and the profile.

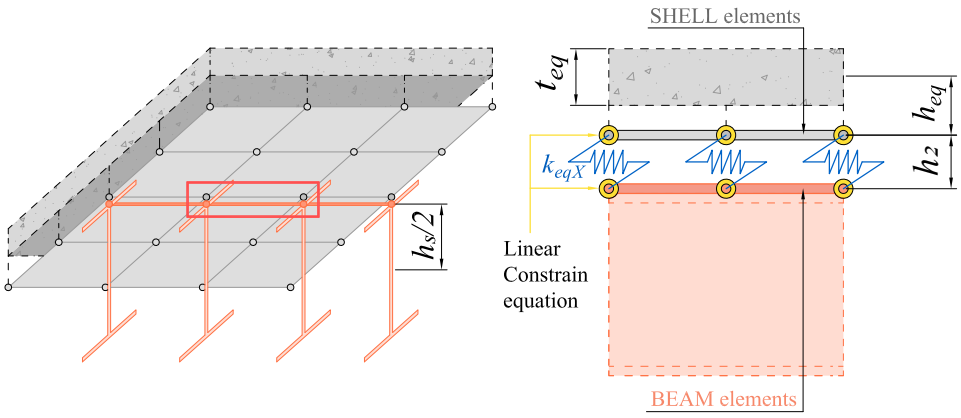

Figure 4.3: Model 2. Simplified Model made of BEAM, SHELL and SPRING elements.

Model 3: Analytical model

The analytical model used is the six-order PDE that has been solved in Chapter 3, based on the DiTaranto [164] and Rao [166] contributions.

This model has been used again in its dimensionless formulation, based on the two parameters before introduced: the geometric parameter Y provided in Equation 3.25, and the shear parameter g given in Equation 3.32. In order to compute the these parameters, the steel profile has been assumed to be the layer 1 of the sandwich beam, the VE treatment is layer 2, and the equivalent rib-deck slab computed for Model 2 has been used as layer 3. The properties of layer 1 are the area, the inertia, the Young modulus and the density of the steel profile. Similarly, the properties of layer 3 are: i) the area $A_3 = t_{eq}b_c$, ii) the inertia $I_3 = (t_{eq}^3 b_c)/12$, iii) the Young modulus $E_3 = E_c$, and iv) the density $\rho_3 = \rho_{eq}$. Additionally, the distance between the centroids of the outer layers has been taken as $h_{31} = h_{eq} + h_s/2 + h_2$.

4.3.2 Types of modal analysis

This subsection describes three different types of modal analysis that can be applied to each type of model described in subsection 3.1.

Complex Modal Analysis

The CMA is considered to provide the most realistic and accurate results in terms of the beam's dynamic behaviour. In this type of analysis, the VE core material is defined with a complex-valued stiffness as the G_2^* aforementioned. The CMA provides a set of different complex circular frequencies of vibration, ω_n^*, each one of them associated with a different complex vibration mode, $\overline{\Phi_n^*}$. As previously indicated, when dealing with VE-damped systems, each complex frequency may be expressed in the following way [164]:

$$\omega_n^* = \omega_n \sqrt{1 + \eta_n i}, \tag{4.5}$$

where ω_n and η_n are the circular natural frequency and the loss factor associated with the n^{th} vibration mode, respectively. Besides, for low-damped structures, as those dealt with hereof, it is important to remember that the damping ratio ξ_n may be obtained as half of the loss factor η_n.

- *CMA for Models 1 and 2.*

  When using an FE model, the CMA consists in solving a complex generalized eigenvalue problem (as the one shown below) with a complex-valued stiffness matrix

$[K^*]$ and a real-valued mass matrix $[M]$, [174].

$$([K^*] - \omega_n^*[M])\overline{\Phi_n^*} = 0. \tag{4.6}$$

Hence, when applying the CMA to the FE Models 1 and 2 the shear stiffness of the VE material has been considered to be complex and equal to G_2^*. This has been done by first, assigning the shear storage modulus G_2' to the VE material and second, specifying the VE loss factor $\eta_{2,ve}$ in the ANSYS pre-processing module. Finally, ANSYS has been commanded to perform a CMA.

- *CMA for Model 3.*

  In Model 3 the CMA has been applied through the set of closed-form equations derived by Rao [166] for a simply supported sandwich beam. Therefore, to compute the different natural circular frequencies of the beam, ω_n^*, it is necessary to previously compute the dimensionless complex circular frequency Ω_n^* using Equation 3.48. Later, this parameter may be dimentionalized and transformed into ω_n^* using Equation 3.47.

Modal Strain Energy Method

The CMA requires a complex-valued eigensolver not commonly found in every commercial structural analysis software. The MSE method enables estimating the damping ratio of a VE damped system by just using real modal analysis (always available in commercial software). This method was first applied to FE models by Johnson and Kienholz [174]. The method estimates the modal loss factor, denoted as $\eta_{n,MSE}$, of the VE damped system as a quotient of two energies: D_n the modal dissipated energy, and V_n the whole modal energy elastically stored in the system:

$$\eta_{n,MSE} = \frac{D_n}{2\pi V_n}. \tag{4.7}$$

The main simplification of this method lies in estimating the modal dissipated energy as follows:

$$V_n = 2\pi\eta_{2,ve}V_2, \tag{4.8}$$

where V_2 is the elastically stored energy in the VE elements of the system.

Both of these stored energies V_n and V_2 are computed using the n^{th} vibration mode $\overline{\Phi_n}$ derived from a real modal analysis in which the VE material is assumed to be elastic with an elastic shear modulus equal to the storage one G_2'. The derivation of these energies depends on whether an FE model or an analytical model is being used.

- *MSE method for Models 1 and 2.*

  In this case, $\overline{\Phi_n}$ (a column vector) is directly derived from a real modal analysis. Then, V_n and V_2 are computed as follows [174]:

$$V_n = \overline{\Phi}_n^T [K] \overline{\Phi}_n, \tag{4.9}$$

$$K_2 = \overline{\Phi}_n^T [K_2] \overline{\Phi}_n, \tag{4.10}$$

  where $[K]$ is the real overall stiffness matrix and $[K_2]$ is a sub-stiffness matrix that only contains the stiffness contributions of the VE elements.

- *MSE method for Model 3.*

  Here, the ω_n of the beam is computed with the closed-form of Rao assuming that $\eta_{2,ve} = 0$. Then, the vibration mode $\Phi(x) = w(x)$ is derived as a mathematical function (depending on the length coordinate x) with the form:

$$w(x) = \sum_{j=1}^{6} A_j^* e^{K_j^* x/L} \tag{4.11}$$

  As indicated in Chapter 3, the wave numbers K_j^* can be obtained solving the a bicubic polynomial similar to the one showed in Equation 3.40 in which the value of $\Omega^* = \Omega_n$. After that, the values of the constants A_j^* can be obtained solving the compatible non-determinate homogeneous system of equations, derived from the different BCs of the sandwich beam. This system has been previously shown for the simply-supported case on Equation 3.45. Again, for this system it is assumed that $\Omega^* = \Omega_n$. Once $w(x)$ and $w(\bar{x})$ are known, the computation of the different energies involved on the MSE method is straightforward.

  The involved energies in PDE of the sandwich beam with VE core are: (i) the bending strain energies of both elastic faces $(V_1 + V_3)_{bending}$, computed using Equation 3.34a (ii) the extensional strain energy of both elastic faces, $(V_1 + V_3)_{extensional}$, calculated from Equation 3.34b , and (iii) the shear strain energies of the VE core, $(V_2)_{shear}$,

extracted from Equation 3.34c. The application of the MSE method is done as follows:

$$V_n = (V_1 + V_3)_{bending} + (V_1 + V_3)_{extensional} + (V_2)_{shear}, \tag{4.12}$$

$$V_2 = (V_2)_{shear}. \tag{4.13}$$

From Equations (4.7) and (4.8) it can be observed that the MSE method establishes a linear relation between $\eta_{2,ve}$ and $\eta_{n,MSE}$, however, from equation (3.48b), it can be observed that the analytical CMA provides a non-linear relation between both magnitudes. Plotting the estimated η_1 from both, CMA and MSE (Figure 4.4), it can be concluded that whereas for lower values of $\eta_{2,ve}$, the linear approximation is accurate, for higher values of $\eta_{2,ve}$, the MSE method considerably over predicts the beam fundamental loss factor η_1. This loss of the linearity between η_1 and $\eta_{2,ve}$ was also commented previously in Figure 3.14.

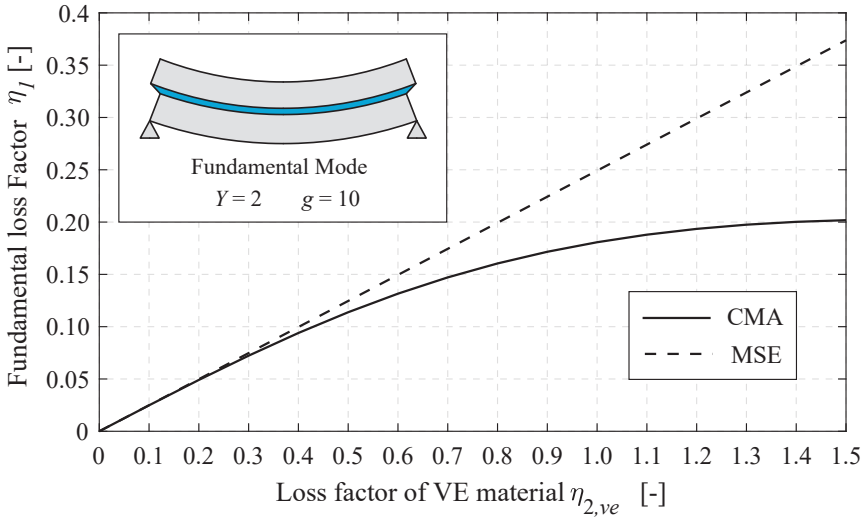

Figure 4.4: Loss factor of the fundamental vibration mode, η_1, of a simply-supported sandwich beam with $Y = 2$ and $g = 10$ as a function of the VE loss factor, $\eta_{2,ve}$. Results computed with Model 1 using CMA and MSE.

Current commercial VE materials used in damping applications commonly have loss factors $\eta_{2,ve}$ higher than 0.8 [172]. Thus, according to this, the MSE method may overestimate excessively the additional damping ratio provided by a VE treatment of this nature. This fact was initially reported by Rongong [175] and further studied by

Torvik and Runyon [176]. In fact, to solve this problem Rongong proposed a modification for the MSE method which will be described in the following subsection.

Rongong's modification to the MSE

Rongong's modification, denoted as RMSE is based on two facts. Firstly, the proposal was based on a previous modification made by Morgenthaler [177] and named the Absolute Value MSE (AVMSE). Morgenthaler noted that the MSE always underestimated the system's natural frequency as it uses the shear storage modulus G_2' of the VE material to perform the real modal analysis. Instead, he proposed to perform the MSE with the modulus of the complex shear modulus $|G_2^*|$ which represents more realistically the actual stiffness of the VE material. Secondly, Rongong noticed that a correction had to be made in the modal energies derived from using $|G_2^*|$ to provide a better approximation to the actual strain energies involved in the MSE.

When simply applying the AVMSE method, a modal loss factor, here named as $\eta_{n,AVMSE}$, is obtained. The modal loss factor given by the RMSE, $\eta_{n,RMSE}$, can be related to this latter as follows:

$$\eta_{n,RMSE} = \frac{1}{\left(\frac{1}{\eta_{2,ve}} + \sqrt{1+\eta_{2,ve}^2}\left(\frac{1}{\eta_{n,AVMSE}} - \frac{1}{\eta_{2,ve}}\right)\right)}. \tag{4.14}$$

Moreover, Torvik and Runyon proved that the RMSE method always slightly underestimates the system loss factor, which results in being convenient when predicting the additional dissipative capacity provided by a damping treatment at the design stage.

4.3.3 Comparison between the different modelling approaches

As a result of combining the 3 types of models with the 3 types of analysis above described, 9 modelling approaches may be defined. These are listed in Table 1.

Within them, the approach M2-RMSE (which employs the simplified FE Model 2, analysed with the RMSE method) is the one proposed in this Chapter as a simple but accurate enough modelling approach for practitioners to model the damping behaviour of the studied CLD-treated floor beams. M1-CMA has been considered to be the approach providing the most accurate and realistic results.

Table 4.1 The 9 different modelling approaches compared.

Modelling Approaches	Model 1: Detailed FE	Model 2: Simplified FE	Model 3: Analytical
CMA	M1-CMA	M2-CMA	M3-CMA
MSE	M1-MSE	M2-MSE	M3-MSE
RMSE	M1-RMSE	M2-RMSE	M3-RMSE

The benchmark beam defined in Section 2 has been used to compare the 9 modelling approaches. For that, the fundamental modal parameters of this beam (its fundamental natural frequency $f_1 = \omega_1/(2\pi)$ and its fundamental loss factor η_1) have been obtained within each approach for different shear stiffness of the VE core,i.e. varying the shear parameter g of the beam through varying the G_2' of the VE material. Thus, obtaining similar results to those previously shown in Chapter 3. This is usually done when assessing CLD treatments, as it is well known that there is an optimum shear stiffness which provides the maximum dissipation capacity to the sandwich beam [7]. When designing an optimum CLD treatment, it is a common practice to modify g by varying h_2 or b_2, as G_2' is a material characteristic that can not be changed at will. However, the author preferred to vary G_2' to maintain constant the geometry of the CLD treatment along each studied beam. Throughout the whole study, g has been computed using Equation 3.32, no matter which model M1, M2 or M3 has been used.

The research performed in this Chapter is limited to the fundamental modal parameters of floor beams, as the fundamental mode is the main contributor to the final dynamic response of the floor under human-induced excitation. Despite this fact, the methodology developed in this Chapter is also applicable for estimating higher-order modal parameters which could be relevant in other structural types or under different dynamic excitation sources, such as machine-induced vibrations. Unlike the analytical PDE, the FE models might be adapted in certain circumstances in which the main hypotheses used for the PDE are not fulfilled.

This comparison is depicted in Figures 4.5.(a) and 4.5.(b) in which the results of each modelling approach are represented with a line characterized by a colour (defining the model) and a type of line (defining the analysis). In both figures, the optimal region around the maximum loss factor has been zoomed in. Additionally, Figures 4.6a and 4.6b depict, for each type of model, the relative errors when predicting f_1 and η_1 with the MSE and RMSE compared to the values provided by the CMA.

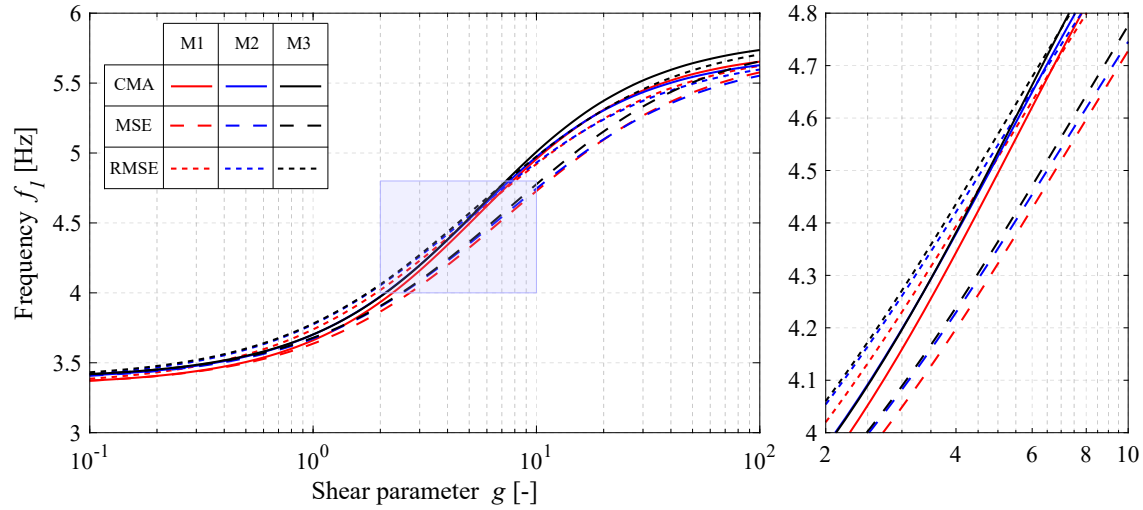

(a) Fundamental natural frequency of the beam f_1

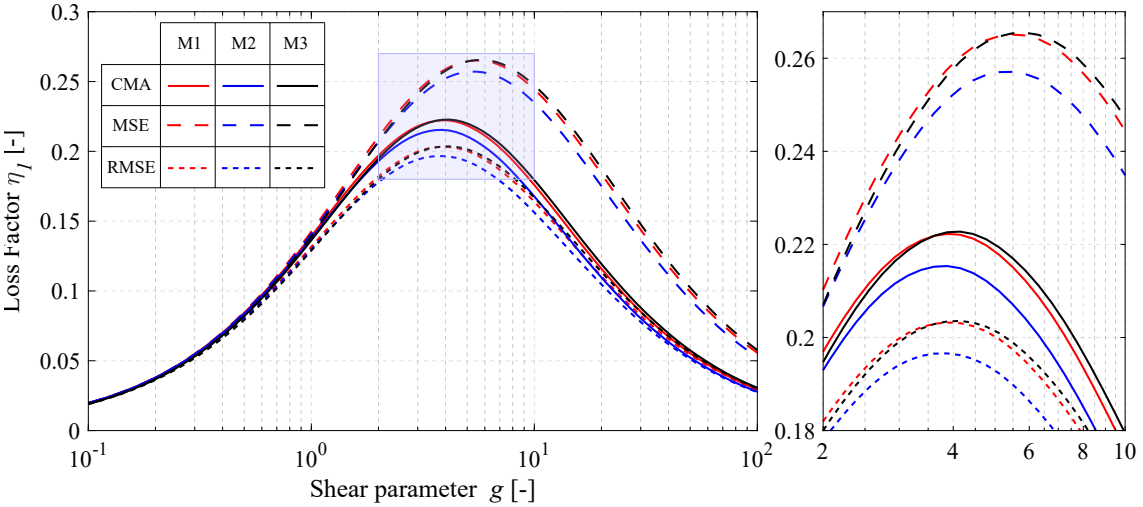

(b) Fundamental loss factor of the beam η_1

Figure 4.5: Comparison of the dynamic parameters of the beam predicted with the 9 different modelling approaches as a function of the shear stiffness of the VE core.

From Figures 4.5 and 4.6, the following conclusions may be extracted. First, models M1, M2 and M3 provide similar results when using the same type of analysis. It is important to highlight that the equivalent constant-height slab used in models M2 and M3 provides similar results to the rib-deck slab modelled in detail in M1. M2 provides lower values of η_1 (with deviations smaller than 5% when compared to model M1) while the fundamental natural frequency is almost identical for both modelling approaches.

Regarding the type of analysis, on the one hand, when compared to the CMA,

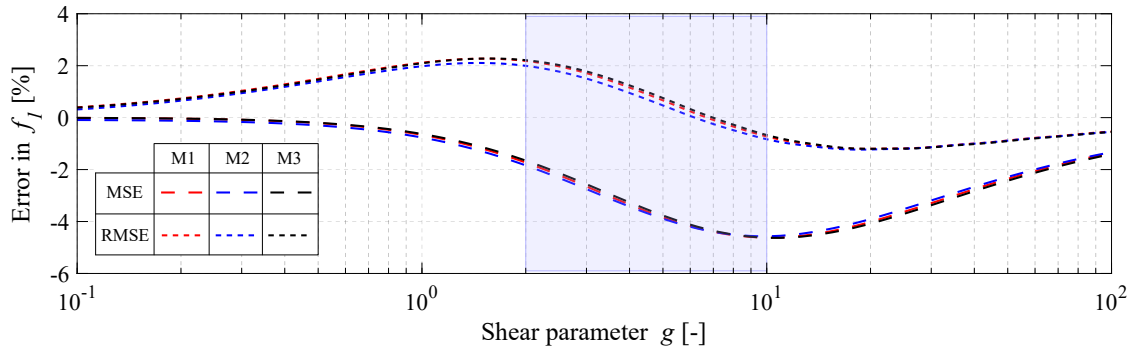

(a) Error in the fundamental natural frequency of the beam f_1

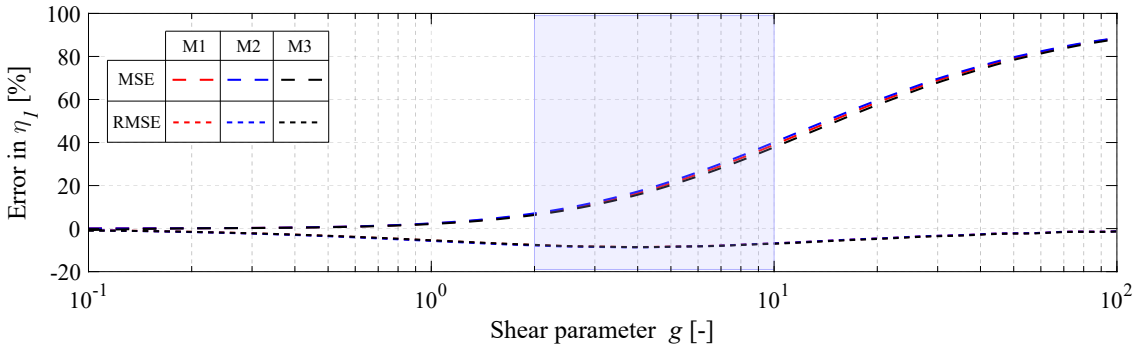

(b) Error in the fundamental loss factor of the beam η_1

Figure 4.6: Error given by the MSE and RMSE compared to CMA.

the MSE always underestimates f_1 (with a limited error of -5%, Figure 4.6.(a)), over predicts η_1 (providing errors of up to +40% in the zoomed-in region, Figure 4.6.(b)) and overestimates the optimal value of g reaching an error for this case of +50% (see zoom in Figure 4.6.(b)). On the other hand, the RMSE method provides limited errors of f_1 (smaller than +2%, Figure 4.6.(a)), always under-predicts the value of η_1 (reaching errors of around -10% in the range of maximum damping, Figure 4.6.(b)) and computes the optimal value of g accurately (see zoom in Figure 4.5.(b)). Thus, the RMSE is accurate enough to estimate at the design stage the additional damping ratio provided by the CLD treatment while remaining on the safe side. Finally, when comparing the proposed modelling approach, M2-RMSE, with the most accurate one, M1-CMA, the maximum error achieved in η_1 is -12%, which is small enough for engineering design purposes. Furthermore, the approach M2-RMSE offers a methodology that considerably reduces the number of nodes and elements in the FE model. In this study, this has meant decreasing by a factor of 10 the time needed to generate and mesh the geometry of the model, and by a factor of 4 the time needed to perform the modal analysis and expand the beam's vibration modes. This fact can be useful when using large structural FE models or when developing

parametric or sensitivity analysis to accurately design the applied CLD treatment, as in these cases, a model of the floor needs to be run many times.

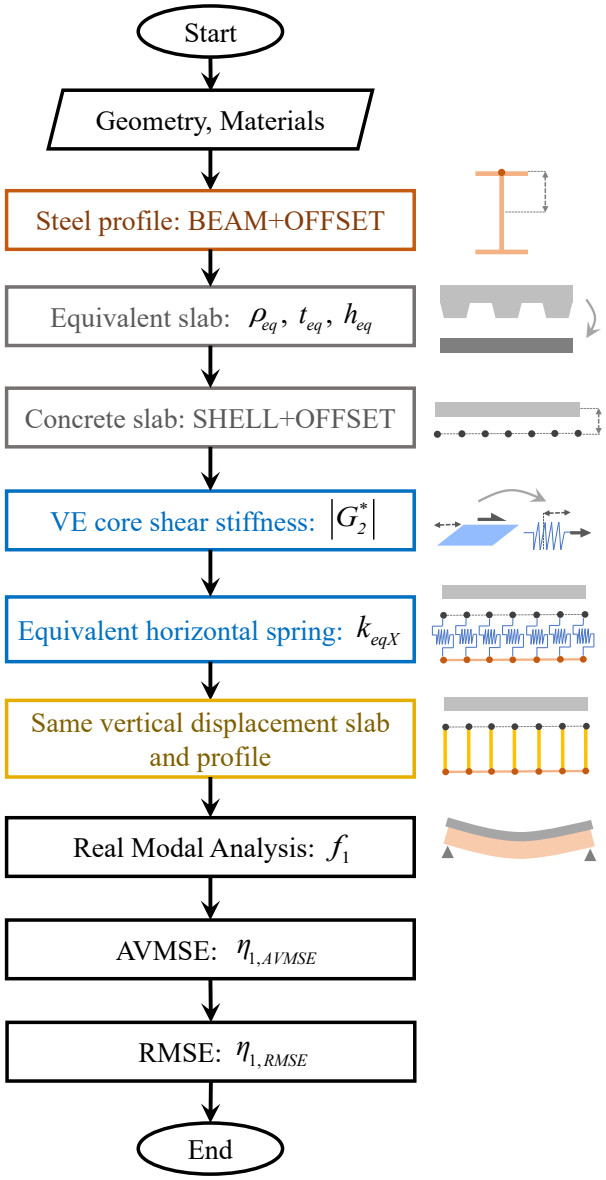

Figure 4.7: Flowchart for M2-RMSE approach.

To sum up, a flowchart for the development of the modelling approach M2-RMSE has been included in Figure 4.7 and can be summarized in the following steps:

1. Model the steel profile with an offset.
2. Compute an equivalent constant-height slab for the rib-deck slab.

3. Model the slab with an offset.
4. Compute the equivalent stiffness of the spring elements used for the VE layer. An elastic stiffness for this layer considering the absolute value of the complex shear modulus is assumed.
5. Model the VE layer with spring elements.
6. Couple the vertical displacement of the steel profile and the concrete slab.
7. Perform a real modal analysis.
8. Compute the η_{AVMSE}.
9. Compute the η_{RMSE}.

4.4 Parametric study

A parametric study is conducted for studying the dynamic behaviour of partially treated composite beams, that is, the CLD treatment is only applied for a percentage of its length. Both approaches, M1-CMA and M2-RMSE, have been used to further check the accuracy of the second one. In this section model M3 has been excluded from the following study. The reason for this decision is the fact that in Model 3, the concrete slab is reproduced as an Euler beam. In partially treated beams, the central region is connected to longitudinal shear using shear studs. Therefore, a big longitudinal shear needs to be transferred between the steel profile and the slab, and so, the shear lag effect becomes prevalent for predicting the slab bending stiffness. This means that in partially treated beams, the fact of modelling the concrete slab as a beam or as a shell has a big impact on the results obtained for f_1 and η_1. Indeed, using a beam model tends to over-predict both parameters.

4.4.1 Studied cases

The set of composite beams partially treated is depicted in Figure 4.8 in which the variation range of the studied parameters is shown. Regarding material properties, a lightweight concrete LWC25 with a characteristic compressive strength $f_{ck} = 25$ MPa was chosen. A steel S275 with a yielding stress f_y =275 MPa was used for profiles. Finally, the VE layer was defined with a constant loss factor $\eta_{2,ve} = 1$ and its complex shear modulus G_2^* is varied for each case.

In terms of geometry, two parameters have been varied: first, the beam length L which adopted values of 6, 9, 12 and 15 m; and second, the percentage of beam length (L_{ve} in Figure 4.8) treated with CLD which has been varied from 0% to 100%, each 10%. The concrete slab geometry has remained constant and has been defined with a steel rib-deck Cofraplus 60 with 1.2 mm gauge, a width $b_c = 3.00$ m and a full height $h_c = 0.12$ m. For the CLD, two 1mm steel sheets and a 1mm VE layer between them have been considered. The width of the CLD treatment has been considered equal to the width of the steel profile.

For each beam resulting from combining a given L, and a given $\%CLD$, the lightest steel profile from the Universal Beams (UB) series that fulfils the static design criteria of the partially treated beam is chosen. For that, a simply-supported beam scheme together with a Dead Load (DL) of 1 kN/m^2 and a Live Load (LL) of 4 kN/m^2 are used. This design complies with the Ultimate Limit State (ULS) and the Deflection Serviceability Limit State (DSLS) according to Eurocode 4 [178]. When $\%CLD = 0$, the resisting section is the composite one, while when $\%CLD = 100$, this section is composed only of the steel one. However, when $\%CLD$ is in between, a beam with a partially connected length arises, so special attention must be paid to these limit states. Some important aspects in this respect are covered in the following subsections.

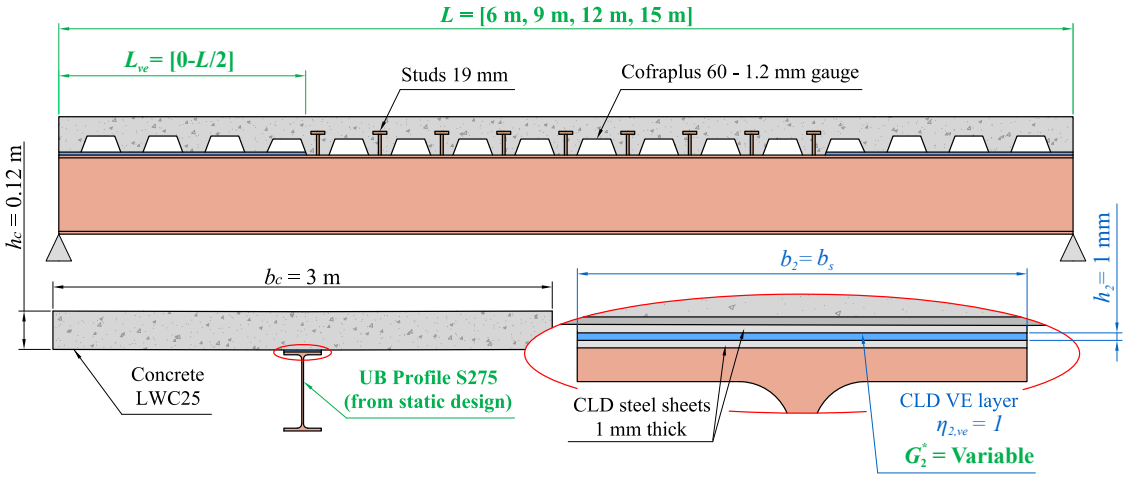

Figure 4.8: Parameters that define each partially treated composite beam for the parametric study (green parameters are those varied along the set of cases).

The parametric study performed is composed of 4 x 11 = 44 beams, each one of them resulting from combining a length L, a $\%CLD$ and an appropriate UB profile. Finally, the

dynamic characteristics of each beam have been extracted with M1-CMA and M2-RMSE for different shear stiffnesses of the VE core, G_2^* and $|G_2^*|$, respectively.

The static design of partially treated beams is covered in more detail in Chapter 6 in the section 6.3, fully devoted to this topic. Here, a summary of the static calculations performed on partially treated beams is provided.

Bending ULS of beams with partial connected length

For this limit state, the following hypotheses are assumed: i) for sections of the beam without shear connection to the slab, the resisting bending moment is the plastic bending moment of the steel profile, and ii) for the mid-span section, the composite action with the concrete slab is considered as follows:

- The effective breath of the composite slab has been computed as follows:

$$b_{effc} = \min \begin{Bmatrix} (L - 2L_{ve})/4 \\ b_c/2 \end{Bmatrix}. \tag{4.15}$$

- The use of ductile shear connectors of diameter 19 mm with rigid-plastic behaviour has been assumed.

- Partial shear connection theory has been used [178]. A 'degree of shear connection' α, has been considered. This one has been computed as follows:

$$\alpha = \frac{P_{rd}(n/2)}{N_{cf}}, \tag{4.16}$$

$$N_c = \alpha N_{cf}, \tag{4.17}$$

where P_{rd} is the design value of the shear resistance of a single shear connector,N_c is the resulting axial load in the concrete slab when the beam bends in ULS with partial shear connection, N_{cf} is the resulting axial load in the concrete slab when the beam bends in ULS with full shear connection, and n is the total number of shear connectors used within the connected length of the beam.

DSLS of the beam with partial connected length

For the DSLS, two different bending stiffnesses along the beam are used: i) the one from the steel profile for the disconnected region, and ii) the one from the full composite cracked section for the central region assuming the same effective breadth described before.

4.4.2 Results

Modal parameters depending on g

Firstly, the modal parameters of each beam, namely, f_1 and η_1 have been obtained as a function of g (computed in the same way as before). Figure 4.9 shows an example for beams with 9 m of span and different $\%CLD$.

Charts with similar behaviour have been obtained for beams of 6, 12 and 15 m span. Some conclusions may be extracted from Figure 4.9a. First, the higher the $\%CLD$, the wider the frequency range along which the beam varies (Figure 4.9.(a)). Second, M2-RMSE predicts accurately the beam frequency. Third, from the optimal points it can be seen that the optimal frequency does not change significantly when increasing the $\%CLD$. This occurs because the loss of stiffness caused by the CLD treatment is compensated with the use of a stiffer UB profile.

Concerning Figure 4.9.(b) and Figure 4.10 the following aspects can be noted. First, the loss factor of the beam increases as the $\%CLD$ increases, and furthermore, the η_1 - g curve for a given $\%CLD$ is an envelope for those of lower $\%CLD$. Second, it can be seen that when the $\%CLD$ is lower than 30%, the increase in damping is marginal. Third, the values of η_1 predicted by the M2-RMSE are slightly lower than those predicted by M1-CMA (Figure 4.10) which is on the safe side. This difference becomes higher for lower $\%CLD$ reaching a maximum error of -35%. Nevertheless, this value corresponds to a relative error and occurs for lower values of $\%CLD$ and thus, it is associated with a small absolute error. This implies that to the author' experience, the proposed methodology is applicable for all ranges of $\%CLD$, as it provides reasonable estimations of the beams' damping ratios in absolute terms.

The difference between both approaches comes from: i) with M1-CMA the use of SOLID elements provides the additional dissipation mechanisms to the model, and ii) in M2-RMSE the use of a constant-height slab introduces also additional deviations. It

should be noted that η_1 is slightly underpredicted with the proposed approach M2-RMSE, which is on the safe side for structural design purposes.

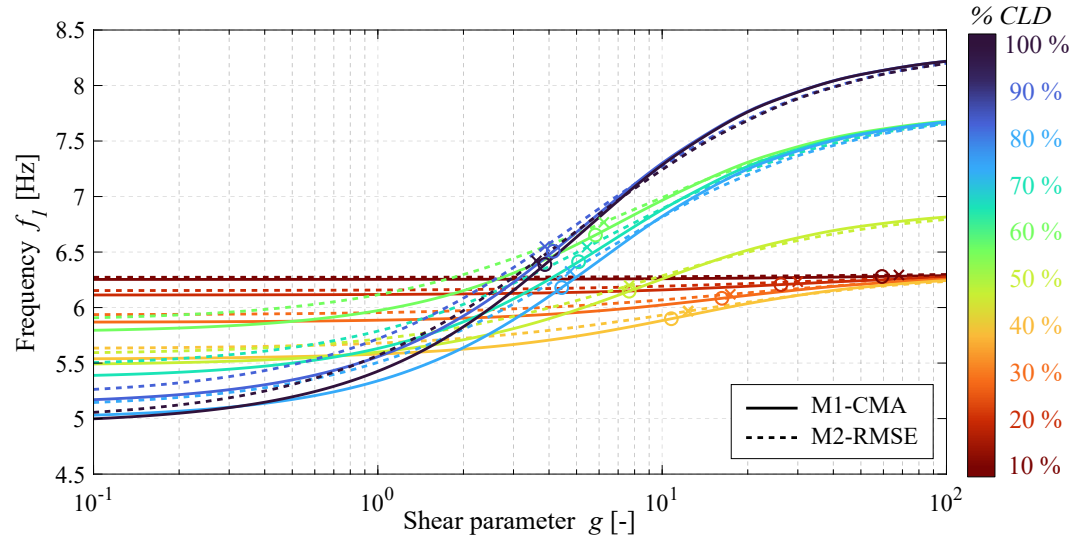

(a) Fundamental natural frequency of the beams f_1

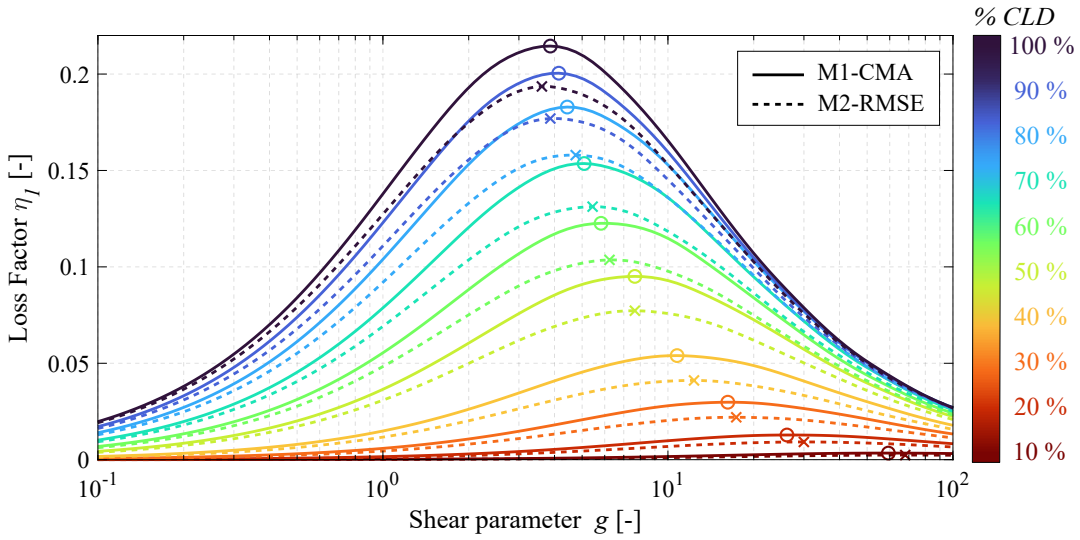

(b) Fundamental loss factor of the beams η_1

Figure 4.9: Parametric study of fundamental modal parameters varying g for 9 m span beams with different $\%CLD$ and computed with M1-CMA and M2-RMSE approaches.

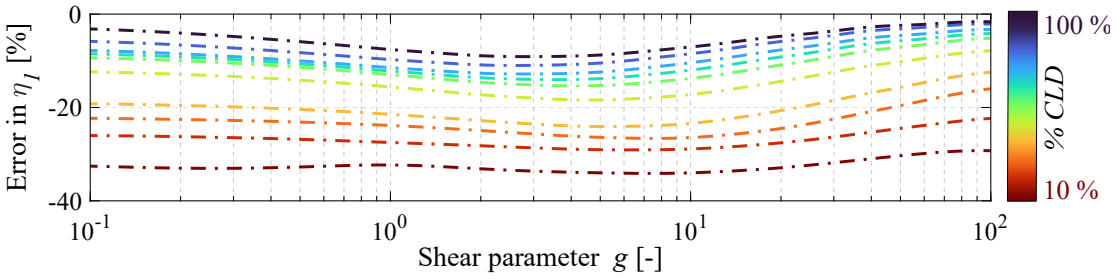

Figure 4.10: Error in the fundamental loss factor as a function of g for 9 m span beams for different $\%CLD$ when using M2-RMSE compared to M1-CMA.

Optimal modal parameters

The optimal values achieved in Figure 4.9 are now analyzed. Three parameters have been studied: the optimal frequency f_{opt}, the maximum loss factor η_{max} and the optimal shear parameter g_{opt}. Figure 4.11 shows these parameters for the 4 considered spans with different $\%CLD$.

The following conclusions can be derived. First, Figure 4.11.(a) shows that the f_{opt} is approximately constant with $\%CLD$ and the error of M2-RMSE is very low and decreases with the span (Figure 4.11.(b)). Second, Figure 4.11.(c) c shows that the value of η_{max} with $\%CLD$ for different beam spans is similar. Despite this fact, the shorter the span, the slightly higher the value of η_{max}. That is, shorter-span beams have smaller UB profiles, and thus, the resulting *'sandwich beam'* section has slightly higher values of Y. This means that the increase of bending stiffness achieved when connecting to shear short-span beams is higher than for long-span beams (where most of the stiffness of the composite section comes from the steel profile). According to Equation (3.49) the higher the value of Y, the higher η_{max} is, which explains the slight increase of η_{max} for short-span beams. In addition, in Figure 4.11.(d), it can be seen that the absolute value of the error of η_{max} is higher for short-span beams.

Third, from Figure 4.11.(e), it is also relevant to remark that the variation of g_{opt} with $\%CLD$ is similar for the different spans, being slightly higher for short-span beams. This can be explained again in terms of dimensionless parameters since g_{opt} depends directly on Y. The M2-RMSE always over-predicts slightly the value of g_{opt} and this error reduces when $\%CLD$ increases.

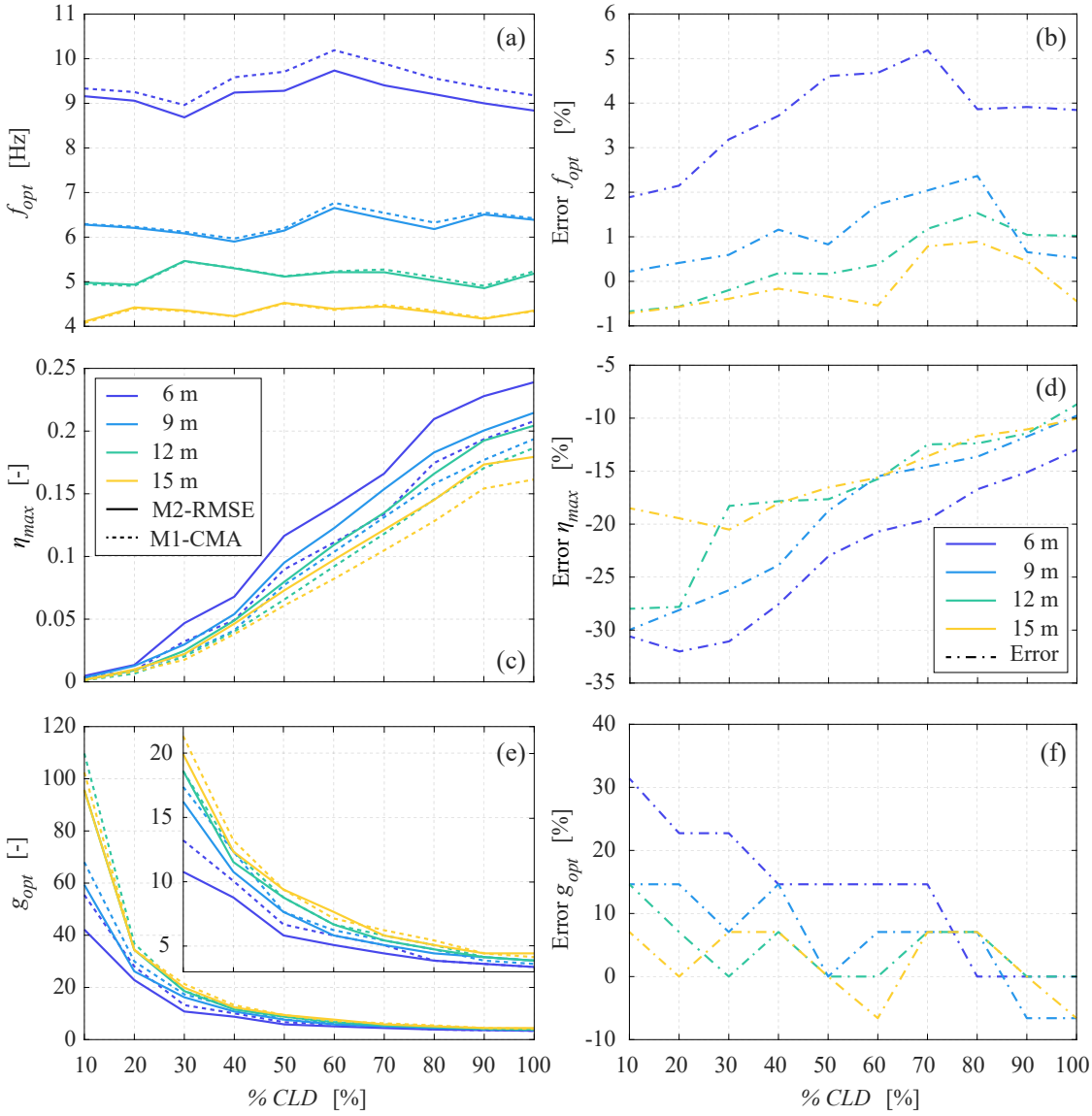

Figure 4.11: Optimal modal parameters for different beam spans and $\%CLD$. Comparison of predictions made with M1-CMA and M2-RMSE. (a) Optimal natural frequency f_{opt}. (b) Error of M2-RMSE in f_{opt}. (c) Maximum loss factor, η_{max}. (d) Error of M2-RMSE in η_{max}. (e) Optimal shear parameter g_{opt}. (f) Error of M2-RMSE in g_{opt}.

4.5 Application example to one-way floors

The optimal results obtained in the previous subsection have been used to predict the dynamic response of single-spanning floors subjected to human walking. Each floor is composed of one bay of secondary beams, all of them simply-supported in columns disposed each 3m (a distance equal to the slab width used for the parametric study). Thus, the modal parameters of the beams previously studied can be used to predict the dynamic response of these floors. A scheme of the floor structural layout is included in Figure 4.12.(a).

The floors' dynamic response has been assessed in terms of i) the response developed by a low-frequency floor when resonates with a given harmonic of the human dynamic load, and ii) the impulsive response after a human footfall (usually used to assess the VSLS of high-frequency floors). For that, a simplified methodology given by the AISC Design Guide 11 [23] has been followed, similar to the one exposed in section 2.3.2. This guideline has been selected because it has proven to have the best calibration when compared to other methodologies of its kind, according to the research done by Muhammad *et al.* [130] and Royvaran *et al.*[131]. Additionally, to demonstrate the effectiveness of CLD treatments at the design stage of lightweight floors, a second set of floors without CLD has been assessed for comparison. For these, a stiffening strategy based on increasing the steel profile of the floor is used to reduce their dynamic response.

4.5.1 Resonant response of low-frequency floors

The fundamental vibration mode of the floor is considered for the resonant response. Therefore, these floor parameters are needed: i) the fundamental natural frequency, in each case assumed to be equal to f_{opt} computed with M1-CMA, ii) the maximum damping ratio to be achieved on the floor with an optimum CLD treatment $\xi_{max} = \eta_{max}/2$ (computed with M1-CMA), and, iii) the effective weight associated to the fundamental vibration mode at its anti-node, W_{eff}. The latter has been computed assuming an effective floor area which is involved in the dynamic response (as depicted in Figure 4.12.(b)) [23]. Its effective length has been considered equal to the beam length, L, and its width B_{eff} has been computed as follows:

$$B_{eff} = 2\left[\frac{EI_{slab}}{EI_{beam}}\right]^{\frac{1}{4}} L, \tag{4.18}$$

where EI_{slab} is the flexural stiffness of the slab and EI_{beam} is of the secondary beam. The latter one is derived from the formula for the fundamental frequency of a simply-supported beam as follows:

$$EI_{beam} = \frac{4 f_{opt}^2 L^4 m}{\pi^2}, \tag{4.19}$$

where m is the mass per unit of length of the beam.

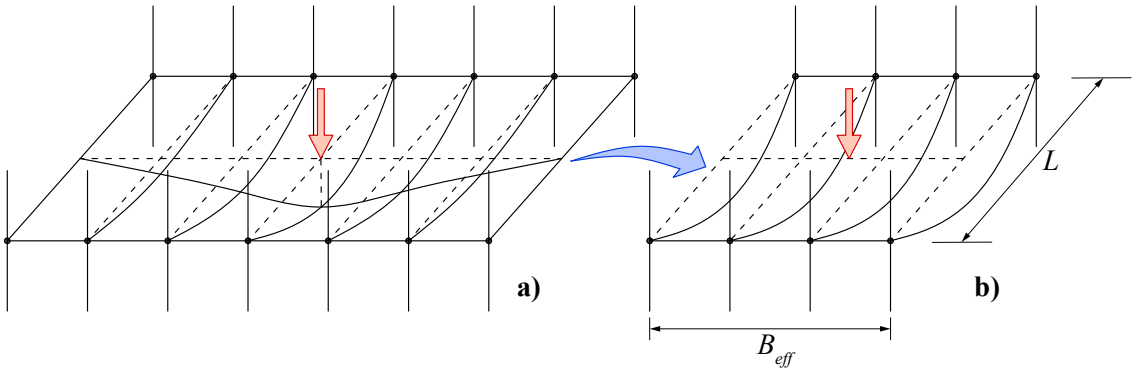

Figure 4.12: Layout of the single-spanning floors assessed. Conceptual representation of the effective floor area involved in the floor response.

Then, the effective weight of the floor is obtained as follows:

$$W_{eff} = 0.5 \; w \; B_{eff} L, \tag{4.20}$$

where the 0.5 factor is used to consider the vibration mode of a single-spanning simply-supported floor and w_{tot}, is the weight per unit of area of the studied floor derived from the following equation:

$$w_{tot} = w_{slab} + \frac{w_{prof}}{b_c}, \tag{4.21}$$

where w_{prof} is the weight per unit of length of the steel profile used in the floor.

A harmonic walking load is applied at the anti-node of the fundamental mode of vibration with a frequency equal to the fundamental natural frequency of the floor:

$$F_w(t) = Q\ \alpha_h \sin(2\pi f_{opt} t), \tag{4.22}$$

where Q is the weight of a human assumed to be 700 N and α_h is the dynamic loading factor depending on the loading frequency as follows:

$$\alpha_h = 0.83\ e^{-0.35 f_{opt}}. \tag{4.23}$$

The response has been computed in terms of peak acceleration according to the expression proposed by the AISC DG 11 [23] as follows:

$$a_{p,res} = \frac{R_{calres}\ Q\ 0.83\ e^{-0.35 f_{opt}}}{2\xi_{max}\,(W_{eff}/a_g)}, \tag{4.24}$$

where R_{calres} is a calibration reduction factor with a value of 0.7 and a_g is the acceleration of gravity.

The peak acceleration can be transformed into a root-mean-square (rms) value, $a_{rms,res}$, by dividing it by a crest factor equal to $\sqrt{2}$. Finally, the response factor R_{res} can be computed by dividing the $a_{rms,res}$ by a base rms acceleration value equal to 0.005 m/s^2 according to [43].

$$R_{res} = \frac{a_{rms,res}}{0.005}. \tag{4.25}$$

4.5.2 Impulsive response after a human footfall

The impulsive response is also computed according to the formulation proposed in [23]. Again, this formulation is a version of the more generic one described in Section2.3.2. The same floor parameters previously computed are used for that. As a load model, the mean effective impulse proposed by Willford and previously given in Equation 2.3 has been used. Therefore, the impulse I_{eff} (with units of [Ns]) has been applied at the anti-node of the fundamental vibration mode, and has been computed as follows:

$$I_{eff} = 42\ \left(\frac{f_p^{1.43}}{f_{opt}^{1.30}}\right), \tag{4.26}$$

where f_p is the human pacing frequency here assumed to be 2.6 Hz (as higher pacing frequencies provide higher impulsive responses in terms of rms acceleration [43]). Remembering the concepts previously commented on Chapter 2, the impulsive response is composed of a peak acceleration $a_{p,imp}$ followed by a decaying response that lasts till the next footfall occurs, during a time equivalent to the pacing period. The rms impulsive acceleration $a_{rms,imp}$ can be computed following a similar formulation to the one shown in Equation 2.22, but expressed in acceleration terms:

$$a_{p,imp} = \frac{2\pi f_{opt} R_M I_{eff}}{(W_{eff}/a_g)}, \tag{4.27}$$

$$a_{rms,imp} = \sqrt{f_p \int_0^{(1/f_p)} \left(a_{p,imp}\, e^{-2\pi f_{opt}\xi_{max} t}\, sin(2\pi f_{opt} t)\right)^2 dt}, \tag{4.28}$$

$$a_{rms,imp} = \frac{a_{p-imp} R_{calimp}}{\sqrt{2}} \sqrt{\frac{1 - e^{-4\pi(f_{opt}/f_p)\xi_{max}}}{4\pi(f_{opt}/f_p)\xi_{max}}}, \tag{4.29}$$

where R_M is a higher mode factor equal to 2, and R_{calimp} is a calibration factor equal to 1.3.

The response factor R_{imp} is again derived according to [43] as follows:

$$\begin{aligned} R_{imp} &= \frac{a_{rms,imp}}{0.005} \;\; (f_{opt} < 8 \text{ Hz}), \\ R_{imp} &= \frac{a_{rms,imp}}{2\pi f_{opt}\, 0.0001} \;\; (f_{opt} > 8 \text{ Hz}). \end{aligned} \tag{4.30}$$

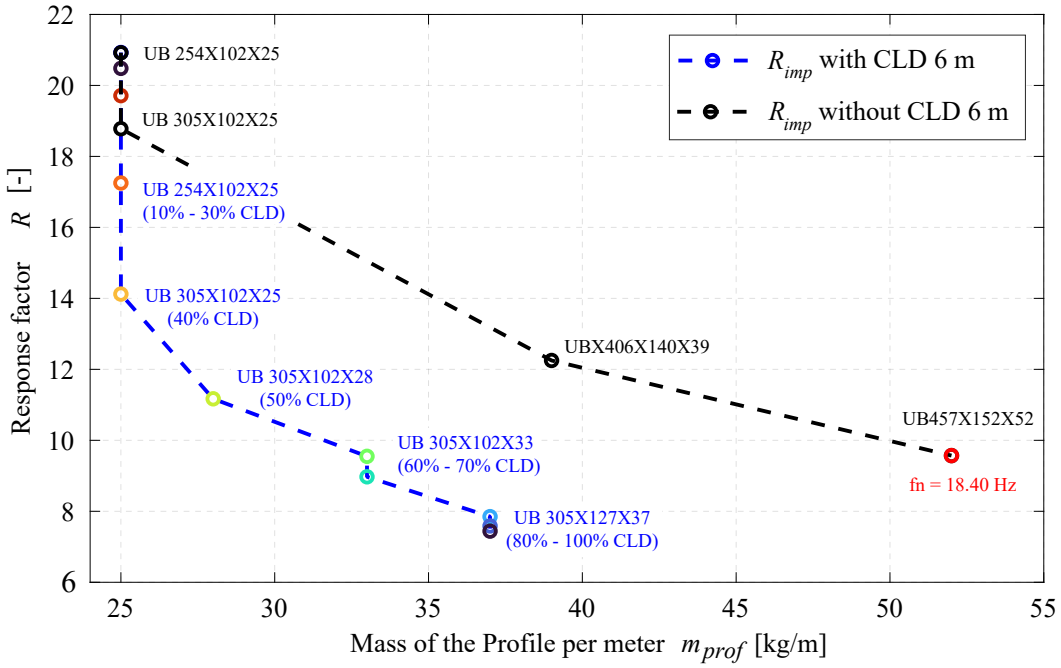

(a) Response of floor with 6 m span.

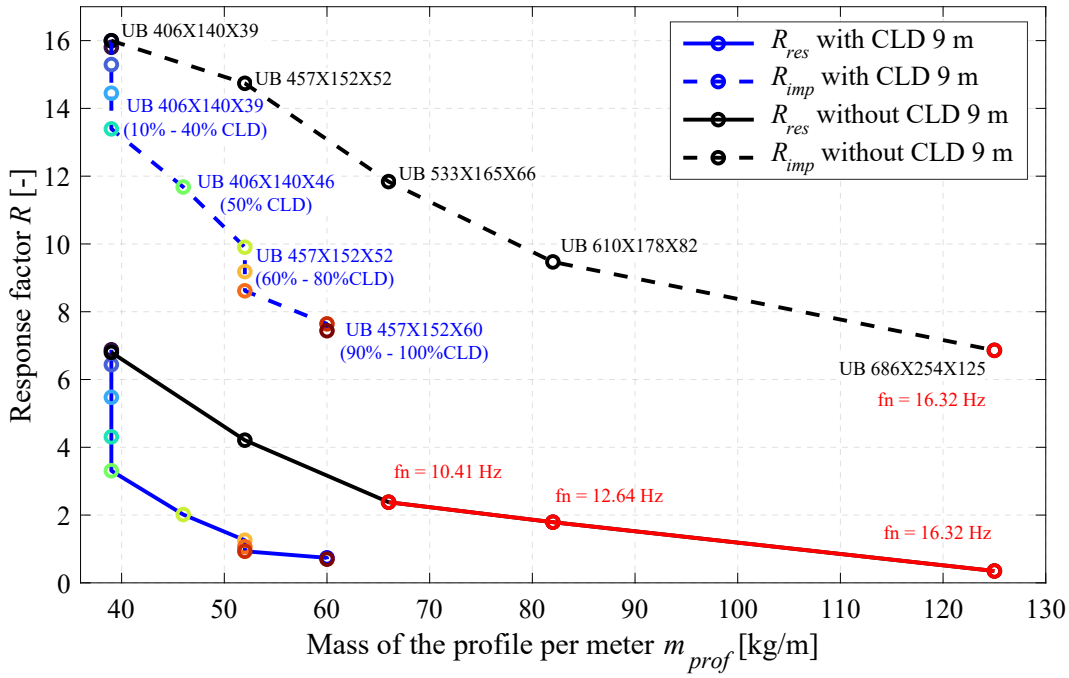

(b) Response of floor with 9 m span.

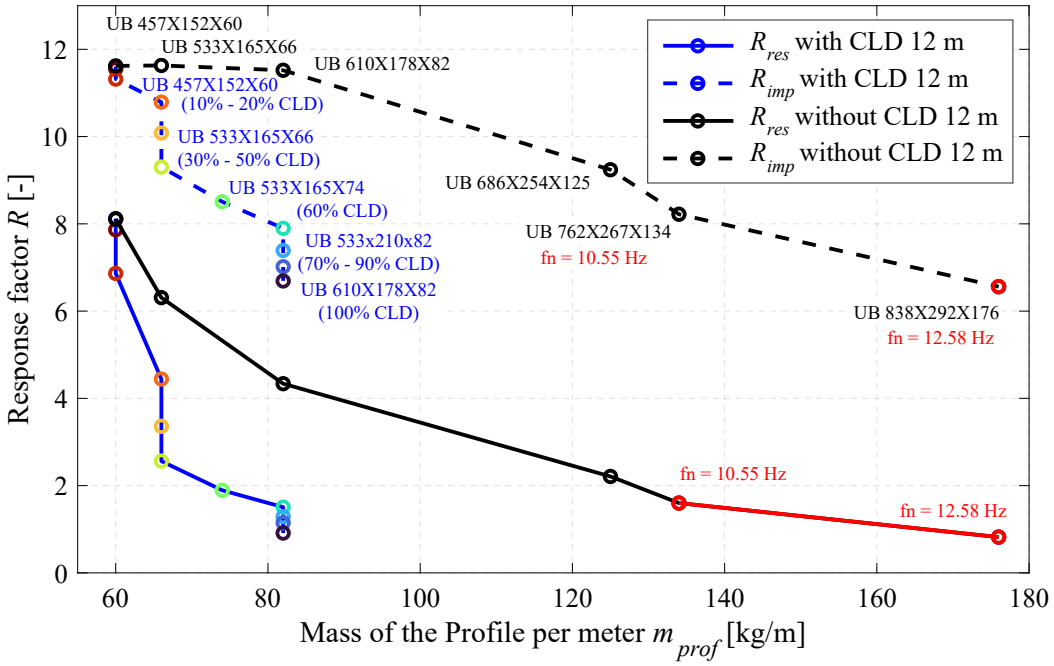

(c) Response of floor with 12 m span.

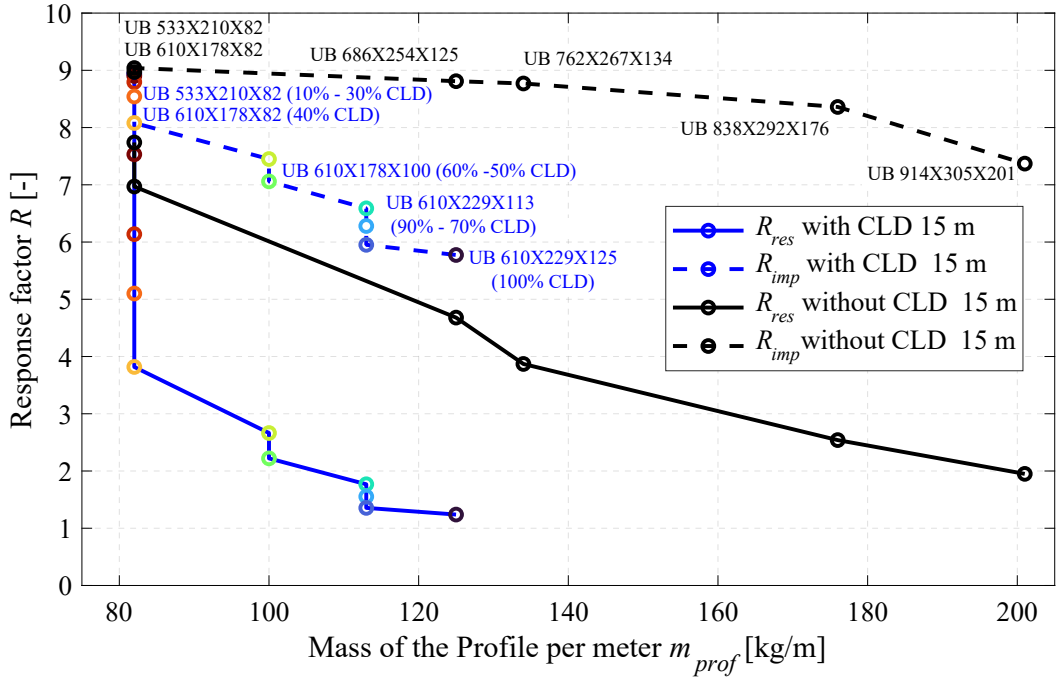

(d) Response of floor with 15 m span.

Figure 4.13: Response factors R_{res} and R_{imp} of assessed beams with and without CLD treatment as a function of the mass of the steel profile used in the floor m_{prof}.

Table 4.2 Numeric results for the dynamic behaviour of one-way floors with 6 and 9 m of span

GEOMETRY		L [m]	$\%\ CLD_{est}$ | $\%\ CLD_{real}$	UB Profile	Y [-]	f_{opt} [Hz] M1-CMA | M2-RMSE	η_{opt} [-] M1-CMA | M2-RMSE	g_{opt} [-] M1-CMA | M2-RMSE	R_{imp} [-] M1-CMA | M2-RMSE	R_{res} [-] M1-CMA | M2-RMSE
Length [m]	6	6	0 | 0	254X102X25	2.35	9.30 | 9.30	0.0000 | 0.0000	-	20.93 | 20.93	5.26 | 5.26
Ribdeck Slab Type	Cofraplus 60		10.00 | 14.57	254X102X25	2.35	9.15 | 9.33	0.0048 | 0.0033	42.18 | 55.43	20.48 | 20.62	4.80 | 4.93
Ribdeck gauge [mm]	1.2		20.00 | 21.60	254X102X25	2.35	9.05 | 9.25	0.0135 | 0.0092	22.82 | 28.01	19.71 | 20.09	4.14 | 4.45
Slab Width [m]	3		30.00 | 35.67	254X102X25	2.35	8.68 | 8.96	0.0468 | 0.0323	10.77 | 13.22	17.25 | 18.24	2.72 | 3.20
Slab Height [m]	0.12		40.00 | 42.70	305X102X25	2.35	9.24 | 9.58	0.0679 | 0.0491	8.77 | 10.06	14.12 | 15.13	1.65 | 1.96
MATERIALS			50.00 | 56.76	305X102X28	2.41	9.28 | 9.70	0.1164 | 0.0896	5.83 | 6.68	11.17 | 12.12	0.96 | 1.14
			60.00 | 63.73	305X102X33	2.38	9.73 | 10.19	0.1402 | 0.1112	5.08 | 5.83	9.55 | 10.34	0.66 | 0.77
Concrete Type	LWC25		70.00 | 70.82	305X102X33	2.38	9.40 | 9.88	0.1660 | 0.1335	4.43 | 5.08	8.97 | 9.72	0.58 | 0.68
			80.00 | 84.88	305X127X37	2.35	9.20 | 9.56	0.2095 | 0.1745	3.87 | 3.87	7.85 | 8.44	0.43 | 0.50
Steel Type	S275		90.00 | 91.92	305X127X37	2.35	9.00 | 9.35	0.2279 | 0.1934	3.61 | 3.61	7.59 | 8.10	0.40 | 0.46
			100.00 |100.00	305X127X37	2.35	8.84 | 9.17	0.2389 | 0.2079	3.37 | 3.37	7.44 | 7.87	0.39 | 0.43

GEOMETRY		L [m]	$\%\ CLD_{est}$ | $\%\ CLD_{real}$	UB Profile	Y [-]	f_{opt} [Hz] M1-CMA | M2-RMSE	η_{opt} [-] M1-CMA | M2-RMSE	g_{opt} [-] M1-CMA | M2-RMSE	R_{imp} [-] M1-CMA | M2-RMSE	R_{res} [-] M1-CMA | M2-RMSE
Length [m]	9	9	0.00 | 0.00	406X140X39	2.24	6.30 | 6.30	0.0000 | 0.0000	-	15.99| 15.99	6.88 | 6.87
Ribdeck Slab Type	Cofraplus 60		10.00 | 13.83	406X140X39	2.24	6.28 | 6.29	0.0034 | 0.0024	59.34 | 68.02	15.80| 15.86	6.43 | 6.56
Ribdeck gauge [mm]	1.2		20.00 | 22.83	406X140X39	2.24	6.21 | 6.23	0.0128 | 0.0092	26.15 | 29.98	15.29| 15.48	5.47 | 5.80
Slab Width [m]	3		30.00 | 31.83	406X140X39	2.24	6.08 | 6.12	0.0298 | 0.0220	16.22 | 17.36	14.44 | 14.82	4.30 | 4.77
Slab Height [m]	0.12		40.00 | 40.83	406X140X39	2.24	5.90 | 5.97	0.0540 | 0.0411	10.76 | 12.34	13.39 | 13.94	3.30 | 3.77
MATERIALS			50.00 | 54.33	406X140X46	2.13	6.15 | 6.20	0.0951 | 0.0773	7.65 | 7.65	11.68 | 12.28	2.01 | 2.29
			60.00 | 63.33	457X152X52	2.11	6.65 | 6.77	0.1226 | 0.1036	5.82 | 6.23	9.90 | 10.42	1.25 | 1.41
Concrete Type	LWC25		70.00 | 72.33	457X152X52	2.11	6.41 | 6.54	0.1536 | 0.1312	5.08 | 5.44	9.18 | 9.68	1.06 | 1.19
			80.00 | 81.33	457X152X52	2.11	6.18 | 6.33	0.1829 | 0.1580	4.43 | 4.74	8.61 | 9.09	0.93 | 1.04
Steel Type	S275		90.00 | 90.33	457X152X60	2.01	6.51 | 6.55	0.2004 | 0.1769	4.14 | 3.86	7.64 | 8.01	0.73 | 0.81
			100.00 | 100.00	457X152X60	2.01	6.39 | 6.42	0.2145 | 0.1936	3.86 | 3.61	7.44 | 7.74	0.69 | 0.75

Table 4.3 Numeric results for the dynamic behaviour of one-way floors with 6 and 9 m of span.

GEOMETRY		L [m]	$\%\ CLD_{est}$ | $\%\ CLD_{real}$	UB Profile	Y [-]	f_{opt} [Hz] M1-CMA | M2-RMSE	η_{opt} [-] M1-CMA | M2-RMSE	g_{opt} [-] M1-CMA | M2-RMSE	R_{imp} [-] M1-CMA | M2-RMSE	R_{res} [-] M1-CMA | M2-RMSE
Length [m]	12	12	0.00 | 0.00	457X152X60	2.01	4.99 | 4.99	0.0000 | 0.0000	-	11.60 | 11.60	8.12 | 8.12
Ribdeck Slab Type	Cofraplus 60		10.00 | 10.51	457X152X60	2.01	4.98 | 4.95	0.0016 | 0.0012	95.70 | 109.70	11.55 | 11.57	7.87 | 7.94
Ribdeck gauge [mm]	1.2		20.00 | 20.07	457X152X60	2.01	4.93 | 4.91	0.0092 | 0.0066	34.37 | 36.80	11.32 | 11.40	6.86 | 7.17
Slab Width [m]	3		30.00 | 31.05	533X165X66	2.02	5.47 | 5.45	0.0248 | 0.0202	18.59 | 18.59	10.79 | 10.93	4.44 | 4.73
Slab Height [m]	0.12		40.00 | 41.74	533X165X66	2.02	5.30 | 5.31	0.0489 | 0.0401	11.53 | 12.34	10.08 | 10.33	3.36 | 3.68
MATERIALS			50.00 | 51.50	533X165X66	2.02	5.11 | 5.12	0.0797 | 0.0656	8.77 | 8.77	9.30 | 9.64	2.56 | 2.87
			60.00 | 61.84	533X165X74	1.93	5.21 | 5.23	0.1093 | 0.0921	6.68 | 6.68	8.51 | 8.87	1.89 | 2.12
Concrete Type	LWC25		70.00 | 72.15	533X210X82	1.80	5.21 | 5.27	0.1348 | 0.1180	5.44 | 5.83	7.90 | 8.21	1.51 | 1.66
			80.00 | 82.34	533X210X82	1.80	5.03 | 5.10	0.1659 | 0.1453	4.75 | 5.08	7.39 | 7.72	1.29 | 1.43
Steel Type	S275		90.00 | 92.51	533X210X82	1.80	4.86 | 4.91	0.1924 | 0.1704	4.14 | 4.14	7.02 | 7.32	1.15 | 1.26
			100.00 | 100.00	610X178X82	1.87	5.18 | 5.24	0.2042 | 0.1865	3.87 | 3.87	6.69 | 6.92	0.91 | 0.98

GEOMETRY		L [m]	$\%\ CLD_{est}$ | $\%\ CLD_{real}$	UB PROFILE	Y [-]	f_{opt} [Hz] M1-CMA | M2-RMSE	η_{opt} [-] M1-CMA | M2-RMSE	g_{opt} [-] M1-CMA | M2-RMSE	R_{imp} [-] M1-CMA | M2-RMSE	R_{res} [-] M1-CMA | M2-RMSE
Length [m]	15	15	0	533X210X82	1.80	4.12 | 4.12	0.0000 | 0.0000	-	8.93 | 8.93	8.10 | 8.10
Ribdeck Slab Type	Cofraplus 60		10.00 | 11.24	533X210X82	1.80	4.11 | 4.08	0.0017 | 0.0014	95.70 | 102.46	8.90 | 8.91	7.84 | 7.89
Ribdeck gauge [mm]	1.2		20.00 | 22.29	610X178X82	1.87	4.42 | 4.40	0.0099 | 0.0080	34.37 | 34.37	8.79 | 8.84	6.14 | 6.34
Slab Width [m]	3		30.00 | 30.57	610X178X82	1.87	4.36 | 4.34	0.0221 | 0.0176	19.91 | 21.31	8.54 | 8.63	5.10 | 5.44
Slab Height [m]	0.12		40.00 | 41.61	610X178X82	1.87	4.23 | 4.22	0.0464 | 0.0380	12.34 | 13.22	8.08 | 8.23	3.82 | 4.18
MATERIALS			50.00 | 52.65	610X178X100	1.71	4.53 | 4.51	0.0729 | 0.0608	9.39 | 9.39	7.45 | 7.66	2.66 | 2.95
			60.00 | 60.94	610X178X100	1.71	4.39 | 4.37	0.0974 | 0.0822	7.65 | 7.15	7.06 | 7.30	2.22 | 2.48
Concrete Type	LWC25		70.00 | 71.98	610X229X113	1.55	4.44 | 4.48	0.1212 | 0.1048	5.83 | 6.24	6.59 | 6.82	1.77 | 1.96
			80.00 | 80.26	610X229X113	1.55	4.31 | 4.35	0.1450 | 0.1280	5.08 | 5.44	6.28 | 6.50	1.55 | 1.70
Steel Type	S275		90.00 | 91.30	610X229X113	1.55	4.17 | 4.19	0.1734 | 0.1542	4.43 | 4.43	5.95 | 6.17	1.36 | 1.48
			100	610X229X125	1.48	4.35 | 4.33	0.1794 | 0.1614	4.43 | 4.14	5.77 | 5.97	1.24 | 1.34

4.5.3 Results of the dynamic behaviour of floors with and without CLD

The results obtained by following the procedure explained in subsections 5.1 and 5.2 are depicted in Figure 4.13 where the response factor of each floor assessed has been plotted against the mass of the steel profile per meter, m_{prof} used in the floor. Blue curves correspond to floors treated with CLD while black ones are stiffened floors without CLD treatment. Continuous lines represent the resonant floor response while the dotted ones represent the impulsive response. Furthermore, the identification of the UB profile used in each case is included next to their impulsive response, and, in the case of CLD-treated floors, the $\%CLD$ is also included next to the dot. For clarification, the same data plotted in blue lines can be found in a numeric format in Tables 4.2 and 4.3. Moreover, some graphs have red sections indicating that the methodology used to compute the response on that specific floor was not calibrated for its natural frequency (which has also been included). In the case of the 6m span floors, only the impulsive response has been computed as their natural frequencies were always over 10 Hz.

Concerning Tables 4.2 and 4.3, They present the numeric results depicted in Figures 4.11 and 4.13. Each table corresponds to a beam length analyzed, L. Each row provides the information for each studied case resulting from combining a beam length L with a given $\%CLD$. The lightest UB profile that satisfies the static design of the beam analyzed is included for each case. The geometry parameter Y of each beam section is also presented. The next columns correspond to the dynamic parameters of the beam optimally treated, f_{opt}, η_{max} and to the optimal shear parameter of each CLD treatment g_{opt}, all of them presented in Figure 4.11. To conclude the Table presents the results depicted in Figure 4.13: the resonant response of CLD-treated floors, R_{res}, and their impulsive response R_{imp}. Every parameter presented has been computed using both approaches, M1-CMA (values at the left side of each cell) and M2-RMSE (values on the right side).

The parameter $\%CLD_{est}$ corresponds to the percentage of CLD that is aimed to be analyzed in each case. However, as the concrete slab is defined with a rib-deck with ribs of a given length in M1-CMA, only certain discrete percentages of CLD may be studied. Thus $\%CLD_{real}$ corresponds to the closest higher real $\%CLD$ that can be assessed.

From Figure 4.13 it can be seen that the amount of steel needed to obtain the same level of dynamic response is much lower when including CLD treatments than when stiffening the floor. On the one hand, in CLD treated floors, m_{prof} increases a 50% when $\%CLD$ increases from 0% to 100% (e.g. from 82 kg to 125 kg in 15 m beams in Figure 4.13.(d), or from 60 kg to 82 kg in 12 m beams in Figure 4.13.(c)), however, R_{res}

drastically decreases from 8 to 1 for 12 m and 15 m beams (Figures 4.13.(c) and 4.13.(d)) and R_{imp} decreases from 8.5 to 5.5 in 15 m beams (Figure 4.13.(d)), or from 16 to 7 in 9 m beams (Figure 4.13.(b)). On the other hand, the stiffening strategy is competitive for 6 m beams (Figure 4.13.(a)) where the frequency of the floor increases fast as the floor is stiffened (despite CLD treatments still providing better designs in this case). However, for 12 m and 15 m floors, the amount of additional steel mass needed to reach the same vibration reduction as the one obtained with CLD is around 120% to 140% (e.g. from 60 kg to 134 kg in 12 m floors, Figure 4.13.(c), or from 82 kg to 201 kg in 15 m floors, Figure 4.13.(d)).

4.6 Conclusions

The presented study provides a detailed analysis of how to predict the additional damping ratio provided by studied CLD treatment, using FE models. More specifically, a simplified modelling approach has been proposed and later validated comparing its results with those obtained with more complex and widely accepted models.

First of all, 3 types of models combined with 3 types of analysis have been used to predict the dynamic characteristics of a case-study beam fully treated with CLD along its overall length. All of them provided similar results. From here, two modelling approaches were chosen to develop a deeper parametric analysis with partially CLD-treated beams: i) the most complex approach, named M1-CMA (with detailed geometry, SOLID elements and using Complex Modal Analysis (CMA)), and ii) the proposed modelling approach named M2-RMSE (which uses spring elements to model the VE layer and employs a modified MSE method). This parametric study was developed by combining different beam lengths (6m, 9m, 12m and 15 m) with different percentages of CLD treatment (from 0% to 100% each 10%). First, It was observed that treatments with $\%CLD$ lower than 30% may not be useful due to the reduced additional damping provided. Second, the M2-RMSE always under-predicted the loss factor of the beams, with maximum relative mismatches with respect to M1-CMA of around -35% (however, higher errors occur for lower percentages of length treated, so their absolute error associated is low). Additionally, the higher the $\%CLD$ and the higher the beam length, the lower this mismatch. Thus, it has been concluded that the approach M2-RMSE is simple and accurate enough for engineering purposes, especially for optimization processes in which many models need to be run to reach a satisfactory solution. This research also provides a detailed step-by-step procedure to accurately develop this modelling approach for practitioners to

easily integrate this damping technology in future designs of lightweight floors.

Finally, a dynamic response analysis of single-spanning floors made with the analysed beams was developed as an application example. The set of CLD-treated floors was compared to a second set of floors in which the vibration level was reduced by stiffening the steel profile of the floor. It was concluded that CLD treatments enable the development of lighter and more slender floors with less use of steel for the same level of vibration. Hence, the CLD treatment when properly designed, is an efficient tool to reduce the embodied carbon of long-span composite floors sized by the VSLS.

The results shown here shed light on the practical ways of modelling CLD treatments applied to civil engineering purposes, and on their effectiveness when designing vibration-sensitive floors.

5

Experimental tests on reduced-scale specimens

5.1 Introduction

This Chapter deals with an experimental campaign developed to study the effectiveness of CLD treatments applied to composite floor beams. These tests mainly aimed to quantify the additional damping ratio provided by this damping technique and understand its main advantages and limitations. In addition, an important effort has been done on experimentally characterizing the dissipation capacity of the CLD treatment at different motion amplitudes in order to answer reasonable questions that may arise like: Will the CLD treatment work at low-motion amplitudes at those experienced by floors? Will the shear dissipation mechanism be activated if the vibration is so small?. To reduce the economic and time effort needed to test full-scale specimens (FSSs) a set of three reduced-scale specimens (RSSs) was designed. These set of specimens have been designed so the 100% CLD RSS exhibits the same amount of extra damping ratio as the 100% CLD FSS, considering that both of them are treated with the same CLD configuration. Once the 100% CLD RSS has been designed, the same beam is tested with 0 and 50% CLD. Along this Chapter, the FSS to be reproduced is first described in subsection 2. Subsection 3 addresses the design process of the equivalent RSS. Section 4 explains the experimental set-up and the series of tests performed. The data post-processing performed on each

type of test in described in Subsection 5. Subsection 6 provides the experimental results obtained. Subsection 7 makes a deep discussion and comparison of results, for finally deriving some conclusions.

5.2 Full-scale specimen

This section is focused on describing the 100% *CLD* FSS to be reproduced by the RSSs later defined in the following sections. The FSS chosen is intended to be a typical simply-supported composite floor beam used for long-span floors, and it has been depicted in Figure 5.1. This one consists of a 12 m span composite beam composed of an IPE 450 profile made of S355 steel with 210 GPa of Young modulus, and a concrete slab with 3 m of width and 0.15 m of height made of RC-25 with 31 GPa of Young modulus. The FSS considered as a reference is a 100% *CLD* with a VE layer applied along its overall length. The dimensions of the damping treatment applied to this beam are the height of the VE layer, h_2= 0.05 mm and its width b_2= 200 mm. Additionally, the VE layer considered is constrained between two thin steel plates of 1mm thickness. The CLD treatment is applied to the RSS with 100% *CLD*, searching to obtain the same amount of additional damping as the one that would be achievable on the FSS with 100% *CLD*.

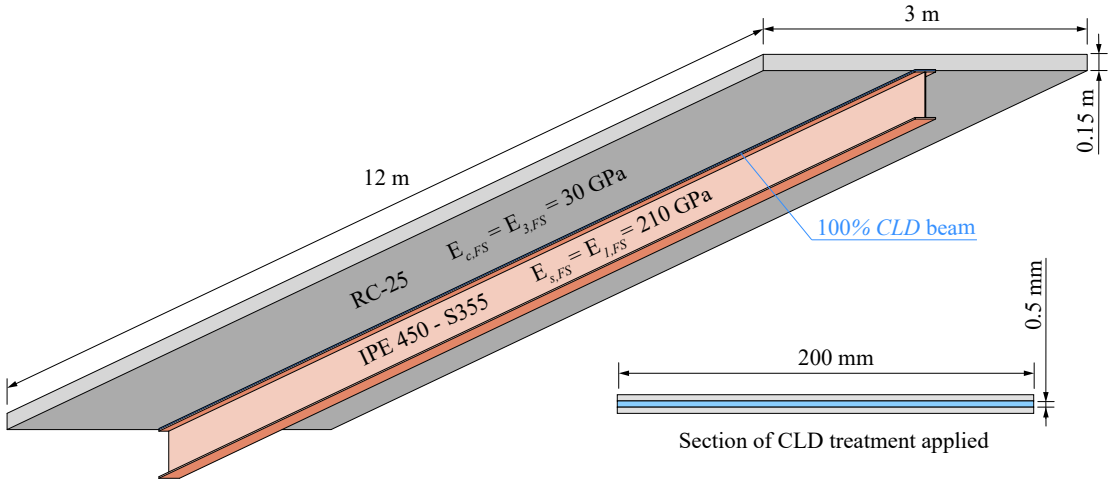

Figure 5.1: FSS to be reproduced.

For simplicity and continuing with the system above established, the following nomenclature will be used in this Chapter. The steel profile will be considered as the base layer of a 'sandwich beam' and so, it will be identified as layer 1. The concrete slab

acts as a constraining layer, so it corresponds to layer 3. Hence, the VE layer will be layer 2. From now on in this Chapter, each mechanical or geometrical property of these layers will be accompanied by two subscripts. The first one is a number from 1 to 3 that refers to the layer. The second subscript will be 'FS' or 'RS' depending on if it refers to variables that belong to the FSS or the RSS, respectively. Additionally, as the only vibration mode concerning to the analysis developed in this Chapter is the fundamental one, the symbols used to refer to the modal properties will lack of the correspondent subscript indicating the modal index. Instead, to subscripts will be used, one indicate FS or RS specimen and a second one to reveal the % CLD.

5.2.1 CLD treatment implemented

The CLD treatment used in the experimental campaign is the one produced by the company Heathcote Industrial Polymers. This treatment is the same as the one ARUP has used for its application in full-scale buildings. An image of this treatment has been included in Figure 5.2, and as can be seen, it is made of three layers, two steel sheets of 0.5 mm thickness that constrain a VE layer of also 0.5 mm.

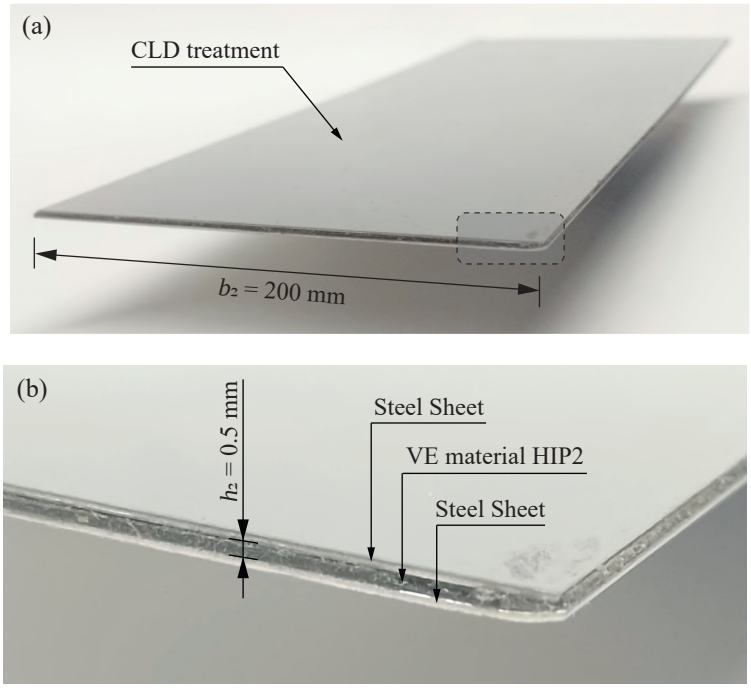

Figure 5.2: CLD treatment used on the experimental campaign. (a) General view. (b) Zoom of the thickness.

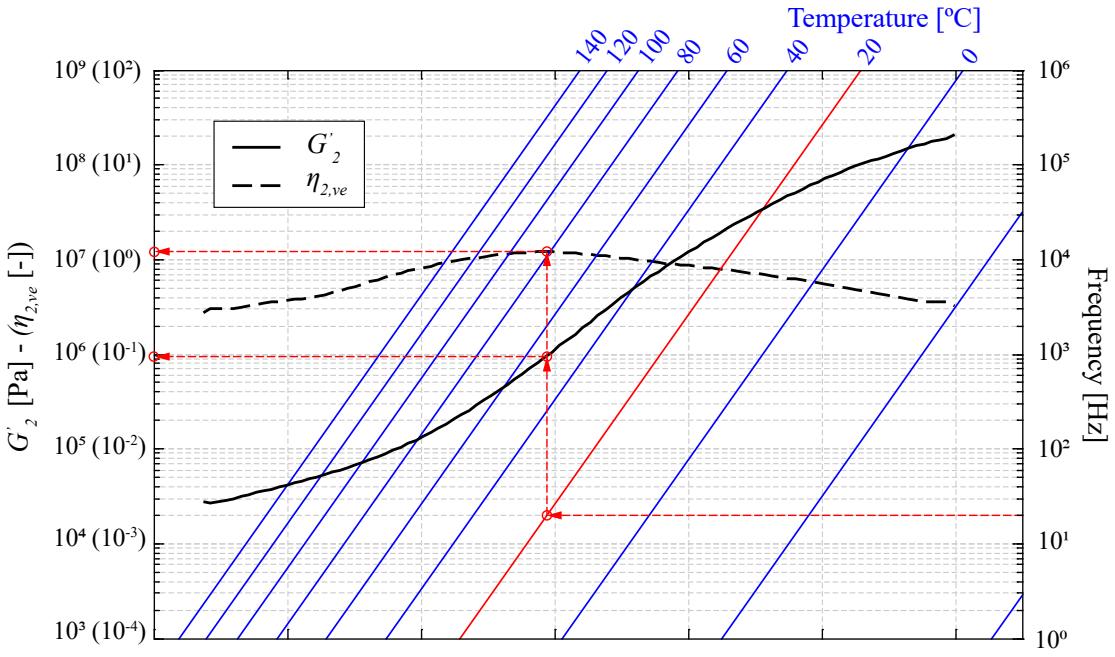

Figure 5.3: Nomogram of the VE material HIP2. [171]

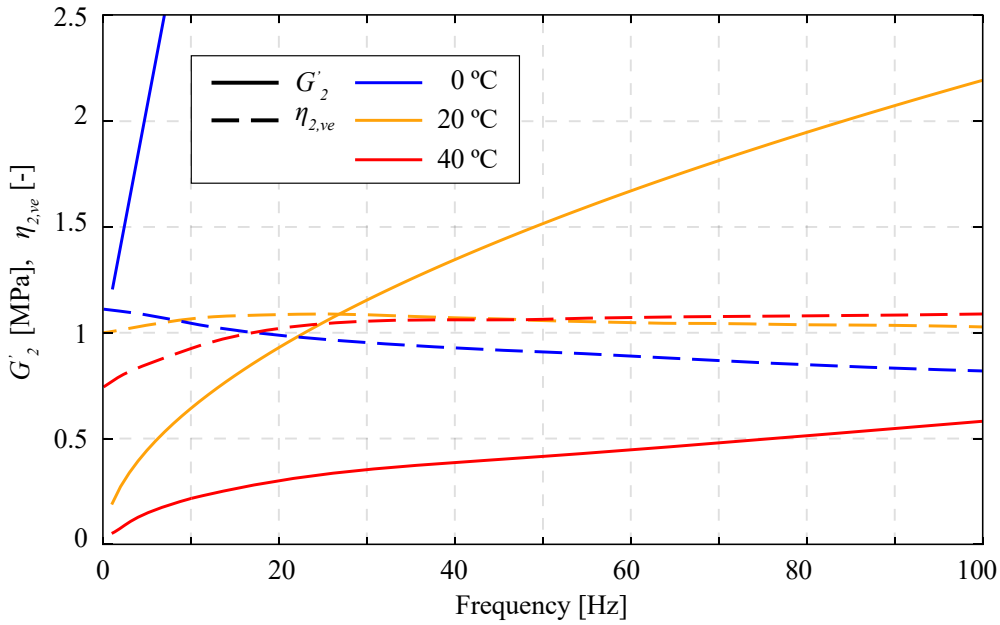

Figure 5.4: Dynamic properties of VE material HIP2 as a function of frequency for different temperatures.[171]

The VE material used for this treatment is the 'HIP2', an elastomeric and rubbery high-damping polymer produced by the same manufacturing company. They provide the dynamic mechanical properties of the HIP2 in the form of a nomogram which has been

included in Figure 5.3. This Figure also includes an example of how to obtain the dynamic properties of the HIP2 for a particular vibration frequency and a particular temperature. In fact in Figure 5.4 both dynamic properties are plotted as a function of frequency for 0, 20 and 40 degrees Celsius. While the loss factor $\eta_{2,ve}$ is more or less constant around a value of 1, the shear storage modulus of the material presents a great variation within temperature and frequency. This harms the effectiveness of the CLD treatment at temperatures different from the one taken as a reference for the design. In this study, the design temperature has been considered as 20 ºC.

5.2.2 Modal parameters calculation considering a frequency dependant VE behaviour

Before describing the process developed to design an adequate, it is important to elaborate on how to deal with a VE core with frequency-dependant mechanical properties. All the studies presented up to now have considered a VE material with constant mechanical properties (at least the loss factor $\eta_{2,ve}$). Although proceeding like this provides good approximations when working within narrow frequency bands (as the one comprised by the typical fundamental natural frequencies of floors between 6 to 10 Hz), it implies a certain level of error. To avoid this error and thus, develop an RSS as faithfully as possible, this variation has been accounted for.

The fact of considering frequency-dependent mechanical properties for the VE material influences the formulation of the PDE of the sandwich beam as its coefficients are no longer constants. Thus, the procedure for computing the complex fundamental natural frequency of the beam, ω_1^*, is altered. Now, an iterative process that involves $\eta_{2,ve}(\omega_1^*)$, $G_2'(\omega_1^*)$ and the own ω_1^* is needed to compute the modal properties of the beam. This iterative methodology is depicted in the flowchart of Figure 5.5 and is composed of the following steps:

1. Compute the fundamental natural frequency of the beam assuming a 0% CLD case, $f_{RS,0\%}$, where all the length is shear connected. This frequency serves as an initial guess value. %
2. Compute the shear modulus G_2 and the loss factor $\eta_{2,ve}$ of the VE material at that guess frequency.
3. Enter into the iterative process:

(a) Compute dimensionless modal properties for j^{th} iteration $\Omega_{1,j}$ and $\eta_{1,j}$.

(b) Dimensionalize results to $\omega_{1,j}$ and $\eta_{1,j}$.

(c) Check fundamental natural frequency convergence with the previous iteration.

(d) Update VE mechanical properties with the last natural frequency computed and continue with the next iteration.

4. Once convergence has been achieved extract the results for ω_1 and η_1

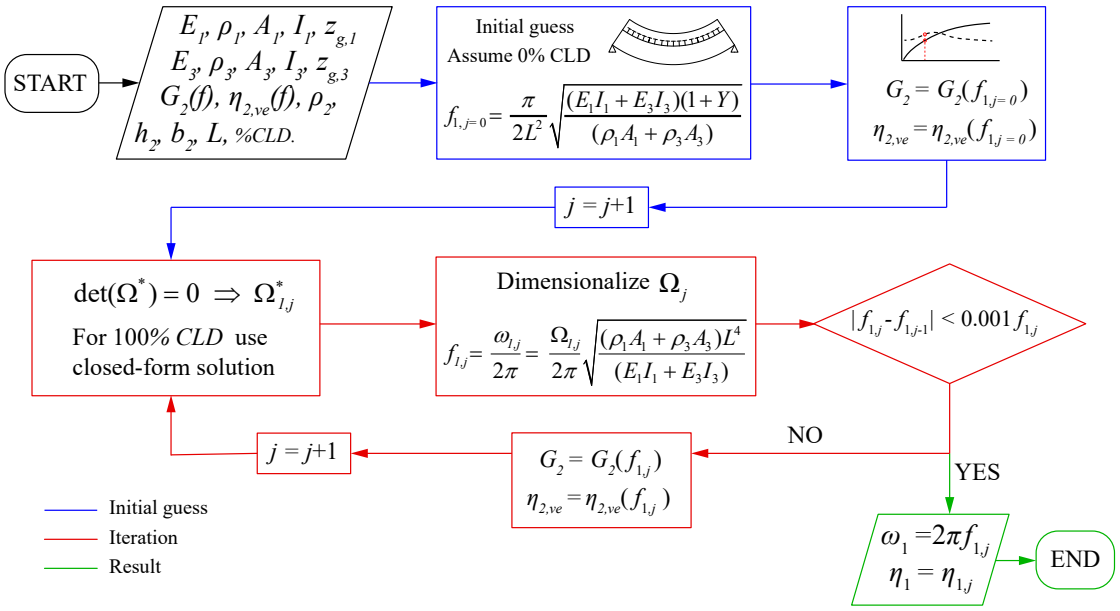

Figure 5.5: Flowchart for the iterative calculation of ω_1 and η_1

5.2.3 Mechanical and modal parameters of the FSSs

In the previous section the process to obtain the modal parameters of a sandwich beam with a frequency-dependant VE core has been explained. This methodology has been used in combination with the analytical model introduced in Chapter 3, to compute the fundamental modal parameters of the FSSs concerning to this chapter. For the cases with CLD treatment, the two steel sheets of the CLD treatment have been considered as part of sections 1 and 3 of the sandwich beam.

Before starting to iteratively compute the modal properties of the FSSs, only two parameters can be known, $Y_{FS} = 1.66$ and $f_{FS,0\%} = 5.05$ Hz. From the second one, a guess of the VE mechanical properties can be obtained so the iterative process can begin.

Table 5.1 Mechanical and modal parameters of FSSs that are replicated with RSSs.

$\%CLD$	Y_{FS} [-]	f_{FS} [Hz]	η_{FS} [-]	g_{FS}[-]	G_2 [MPa]	$\eta_{2,ve}$ [-]
0% CLD	1.67	5.05	-	-	-	-
50% CLD	1.66	4.77	0.055	13.68	0.433	1.034
100% CLD	**1.66**	4.55	**0.145**	13.34	0.422	1.033

5.3 Reduced-scale specimen

Two different concepts are treated in this Chapter: i) FSSs which refers to the specimens whose damping behaviour wants to be reproduced, for which predictions are made, but which are not actually tested, and ii) RSSs which refers to the specimens finally tested and that are used to reproduce the first one.

Ideally, three FSSs with 0, 50 and 100% CLD would be tested. The one with 0% CLD would be shear-connected using studs, displaying the highest natural frequency and the lowest damping ratio. When increasing the % CLD, the natural frequency would decrease and the damping ratio would increase. The test of three FSSs would have required a higher economic cost and a considerably higher amount of time, laboratory space and auxiliary media devoted to the specimens' construction. These constraining reasons, especially the one related to the laboratory space, impulsed the development of three RSSs. These specimens have been used to carry out the same experiments designed for the FSSs but at a much more affordable cost.

5.3.1 Conceptual design of RSS

Initially, some conceptual decisions were adopted before starting to define in detail the geometry and the mechanical properties of the RSSs. These previous dispositions enabled focusing and guiding this scaling process. These are the following ones:

- The structural type of the RSSs has to be analogous to the one of the FSSs. This means that the RSSs need to be conceived as simply supported composite beams made of a steel profile and a concrete layer between which there is a thin VE layer. This has been decided to have beams with the same materials as those of the FSS. Additionally, the use of concrete allows for great geometrical flexibility when designing a reduced-scale beam that needs to meet certain scaling rules.

- The configuration of the CLD treatment applied to both FSSs and RSSs has to be identical.
- The amount of extra damping ratio achieved on the RSS with 100% CLD has to be the same as the one predicted for the FSS with 100% CLD.
- The flexibility of the RSS should be maximised and its length minimised.

According to these principles, the conception process depicted in Figure 5.6 has been followed to come out with a preliminary design. The first option contemplated to develop an RSS uses a smaller IPE profile combined with a concrete slab. For short spans, this option provides beams with considerably higher natural frequencies, for that, a second option with less bending stiffness, in which the IPE profile is rotated 90º, has been considered. Finally, to solve the complicated geometry of this second option, a third one in which a UPE or UPN profile substitutes the IPE profile has been developed. Option 3 has been finally chosen as a conceptual design for the RSS.

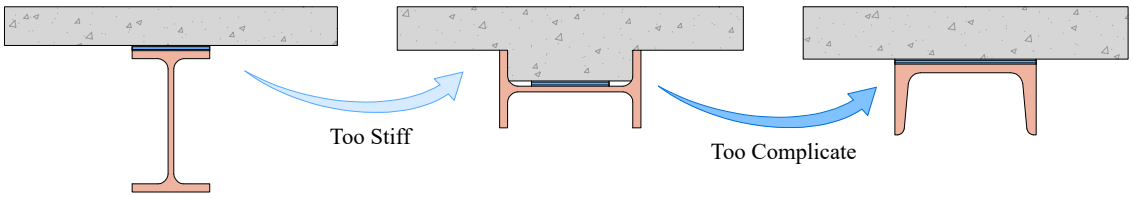

Figure 5.6: Conceptual Design of RSSs.

5.3.2 Scale laws for the *100% CLD* RSS

To develop a representative 100% CLD RSS able to exhibit the same damping ratio as the reference FSS, a set of scale laws needs to be mathematically defined. These rules have been developed based on the non-dimensional formulation for the sandwich beam presented in Chapter 3. More specifically, it has been used the formulas for the closed-form solution of the simply-supported sandwich beam presented in Equation 3.48 of Section 3.3.2.

Thus, the non-dimensional version of the sandwich beam PDE is the keystone of the process developed to obtain an equivalent reduced-scale version of the specimens that would have been wished to be tested.

The following scale laws have been established to compute the right dimensions that the RSS should have to be an equivalent version of the FSS:

- First, as the same materials are used in the base and constraining layers of the FSS and the RSS, the following equities are met:

$$E_{1,RS} = E_{1,FS}, \tag{5.1a}$$

$$\rho_{1,RS} = \rho_{1,FS}, \tag{5.1b}$$

$$E_{3,RS} = E_{3,FS}, \tag{5.1c}$$

$$\rho_{3,RS} = \rho_{3,FS}. \tag{5.1d}$$

- Second, as both the RSS and the FSS have the same CLD treatment, the following rules are met:

$$2h_{2,RS} = 2h_{2,FS}, \tag{5.2a}$$

$$b_{2,RS} = b_{2,FS}. \tag{5.2b}$$

- Third, both the RSS and the FSS need to have the same extra damping ratio for the 100% CLD case, thus, their Fundamental loss factors $\eta_{RS,100\%}$ and $\eta_{FS,100\%}$ need to be equal:

$$\eta_{RS,100\%} = \eta_{FS,100\%} = 0.145. \tag{5.3}$$

- Fourth, it has been considered convenient that both FSS and RSS have the same geometric parameter Y :

$$Y_{RS} = Y_{FS} = 1.66. \tag{5.4}$$

5.3.3 Restrictions Imposed to the RSS design

In addition to the scale laws above presented, the author decided to impose a set of restrictions that the RSSs should fulfil to meet their original purpose (being smaller and more manageable than the FSSs). These conditions can be formulated as constraints in equations as follows:

- First, to preserve the reduced-scale nature of the tested specimens, their span has been limited to 4 m. Thus the following limitation has been imposed:

$$L_{RS} < 4m. \tag{5.5}$$

- Second, for testing reasons the maximum frequency of the 0 % CLD, $f_{1,RS,0\%}$ RSS has been limited to 20 Hz. This decision has been adopted due to several reasons. First, this frequency value is an upper limit for the full-capacity operation of the electrodynamic shaker used for the dynamic tests. Second, because at the time the specimens were developed, future works related to dynamic digital image correlation (DIC) were planned. A limited natural frequency was needed to use a regular camera with a maximum sampling frequency of 100 Hz. These works have been finally postponed so they have not been carried out as a part of this thesis.

$$f_{RS,0\%} < 20Hz. \tag{5.6}$$

5.3.4 Computation of the geometrical configuration for the RSS

In order to find a suitable RSS, a sensitivity analysis has been carried out. Within this study different steel profiles, concrete slab dimensions and specimen lengths has been explored. The main process followed to find equivalent RSSs has been depicted in Figure 5.7. The different steps of this process are three and are described below:

Step 1: Initial parameters

Two initial parameters have to be defined for the specimen: the UPN profile used (Which implies the definition of all geometrical and mechanical parameters of layer 1) and the width of the concrete slab, $b_{3,RS}$.

Step 2: Concrete slab definition to meet $Y_{FS} = Y_{RS}$

The concrete slab height, $h_{3,RS}$, has to be defined so Equation 5.4, $Y_{FS} = Y_{RS}$, is met. There, Y_{FS} is a constant already known and the only remaining parameter to fully define the RSS section is $h_{3,RS}$. This parameter is a solution of a 4^{th} order polynomial expression that emerges from substituting Y_{RS} as a function of $h_{3,RS}$ in Equation 5.4. In the study performed, the 1 mm steel sheets that belong to the implemented CLD treatment have been included as parts of sections 1 and 3. This means that their bending and axial stiffness have been included in layers 1 and 3. However, if not included, a simpler and much more illustrative expression can be derived to understand the computation of $h_{3,RS}$.

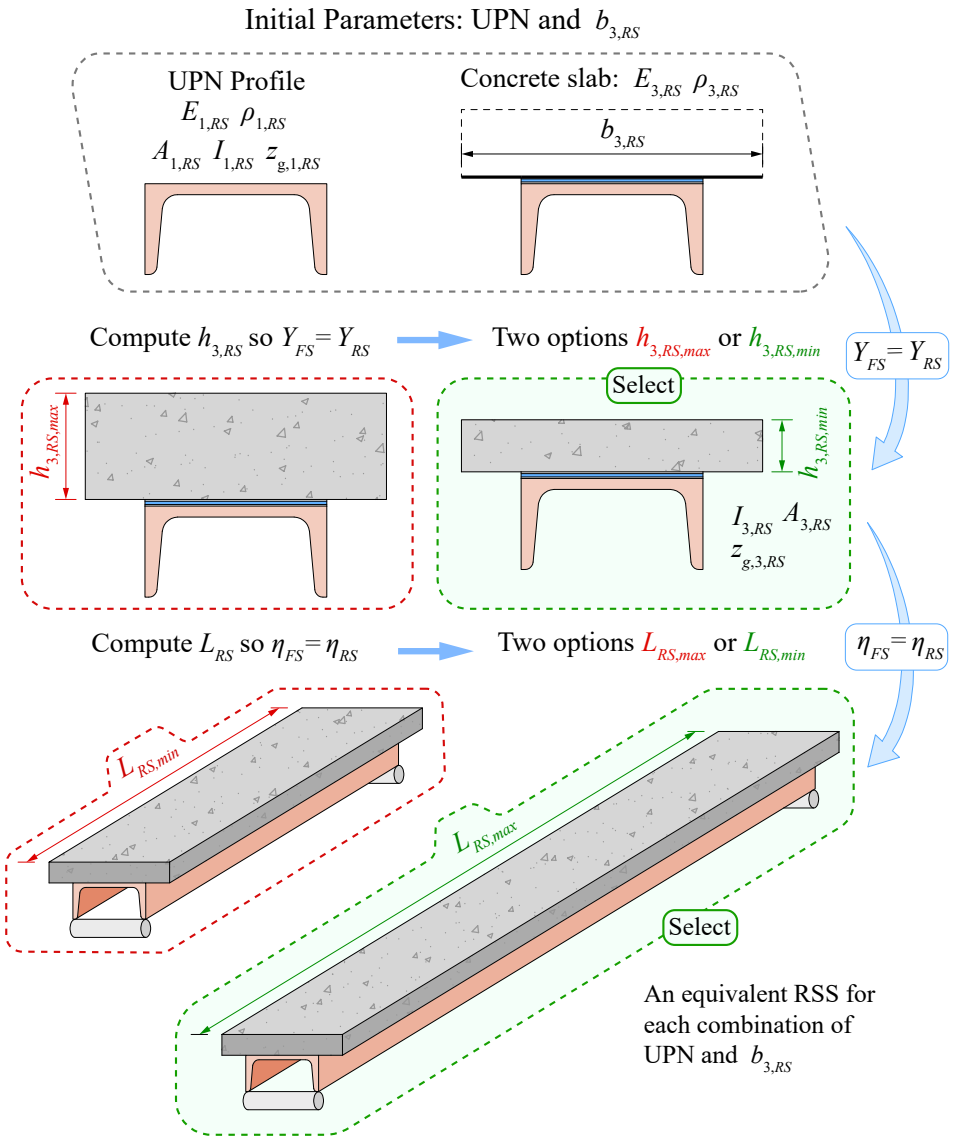

Figure 5.7: Flowchart for the computation of the adequate geometry of RSSs

$$Y_{FS} = \left(\frac{(h_3/2 + z_{g,1} + 2h_2 + 0.001)^2}{E_1 I_1 + 1/12 E_3 b_3 h_3^3} \frac{E_1 A_1 E_3 b_3 h_3}{(E_1 A_1 + E_3 b_3 h_3)} \right)_{RS} \tag{5.7}$$

This equation may have two or zero real solutions for $h_{3,RS}$. When having two, these correspond to two possible heights of the concrete slab that would produce an RSS equivalent in terms of Y to the FSS. From those, the most convenient height was finally chosen based on construction ease, this means, avoiding extremely thin or thick slabs. On the RSS finally developed with a UPN 200, the $h_{3,RS,min}$ was chosen.

Step 3: Length definition to meet $\eta_{FS,100\%} = \eta_{RS,100\%}$

Finally, the length of the RSS has been set to meet the condition $\eta_{FS,100\%} = \eta_{RS,100\%}$. According to equation 3.48.b the fundamental loss factor is a function of Y, $\eta_{2,ve}$ and g. Assuming that the VE mechanical properties are constant and substituting $\eta_{RS,100\%}$ by the aforementioned equation the following expression is obtained:

$$\eta_{FS} = \left(\frac{\pi^2 Y g \eta_{2,ve}}{\pi^4 + \pi^2 (2+Y) g + \left(1+\eta_{2,ve}^2\right)(1+Y) g^2} \right)_{RS} \tag{5.8}$$

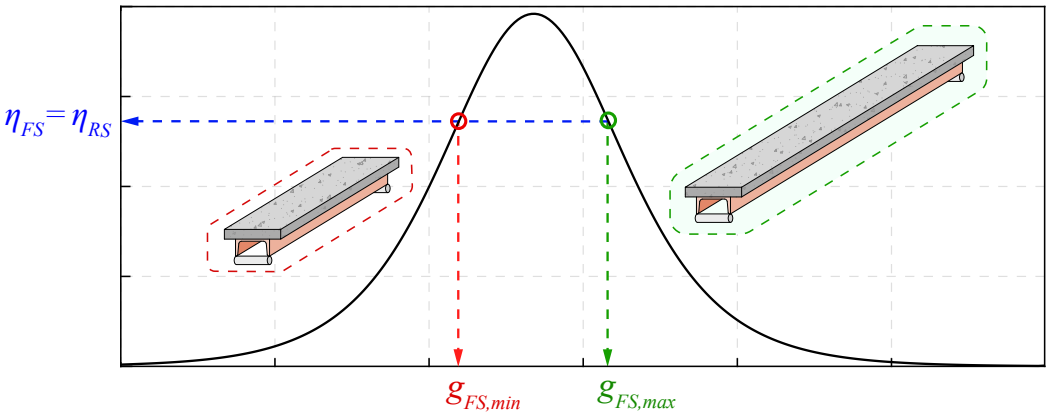

Figure 5.8: Two equivalent g values of the RSS, each one associated to a possible length that the specimen might have.

This equation can be transformed into a 2nd order polynomial equation in which the only unknown is g_{RS}. Again two possible values of g_{RS} may be selected, $g_{RS,min}$ and $g_{RS,max}$. These correspond to the two possible values of g that produce the same amount of loss factor on a sandwich beam, as indicated in Figure 5.8.

According to the definition of g_{RS}, this one is directly proportional to L_{RS}. Therefore, the options $g_{RS,min}$ and $g_{RS,max}$ imply equivalent RSSs with lengths $L_{RS,min}$ and $L_{RS,max}$, respectively. These lengths may be computed from Equation 3.32 as follows:

$$L_{RS} = \left(+\sqrt{\frac{g\ 4\ h_2^2 (E_1 A_1 E_3 A_3)}{G_2\ 2h_2\ b_2 (E_1 A_1 + E_3 A_3)}} \right)_{RS} \tag{5.9}$$

Finally, between both options the one represented by $g_{RS,max}$ and $L_{RS,max}$ has been

selected. This has been done to better replicate the FSS, as its shear parameter was indeed a $g_{FS,max}$. Thus, the FSS shear parameter was located at the right side of the optimum point into the $\eta(g)$ curve. Furthermore, selecting $g_{RS,min}$ would have implied a much shorter RSS with a considerably higher fundamental natural frequency and in which the beam bending hypothesis might not be met.

Up to now, this third step has been explained assuming that the VE mechanical properties are constant in frequency. However, if they are considered frequency-dependant, an iterative calculation has to be carried out. This one is similar to the one depicted in Figure 5.5. This procedure has the following particular steps.

1. G_2 and $\eta_{2,ve}$ are initially guessed.
2. $g_{RS,max}$ is derived form Equation 5.8.
3. $L_{RS,max}$ is computed from Equation 5.9.
4. $\Omega_{RS,100\%}$ is computed from Equation 3.48.a.
5. $f_{RS,100\%}$ is obtained by dimensionalizing $\Omega_{RS,100}$ and dividing it by 2π.
6. G_2 and $\eta_{2,ve}$ are updated entering with $f_{RS,100}$ in Figure 5.4 for 20 ºC.
7. This steps are repeated till convergence is achieved.

Sensitivity analysis for the RSS selection

Once explained the process followed to produced equivalent RSSs, a sensitivity analysis has been carried out considering different UPN profiles, and different concrete slab widths. Two particular examples of this sensitivity analysis, considering a UPN 140 and a UPN 200 have been depicted in Figures 5.9.(a) and (b), respectively. Each Figure considers the use of a UPN profile. The horizontal and vertical axis represent $b_{3,RS}$ and $h_{3,RS}$, respectively. As already has been explained in Step 2, only certain combinations of $b_{3,RS}$ and $h_{3,RS}$ provide a RSS compliant with the sacle law $Y_{FS} = Y_{RS}$. These combinations are represented with green and red dashed-dotted lines, the red for the $h_{3,RS,max}$ and the green for $h_{3,RS,min}$. Additionally, a contour plot has been overlaid in each Figure representing the values of $L_{RS,max}$ that for each case, enable meeting the scale law $\eta_{FS} = \eta_{RS}$. Finally the design conditions $L_{RS} < 4$ m and $f_{RS,0\%} < 20$ Hz are depicted with orange and blue thick lines, respectively. The withe area defined between these lines contains the specimens

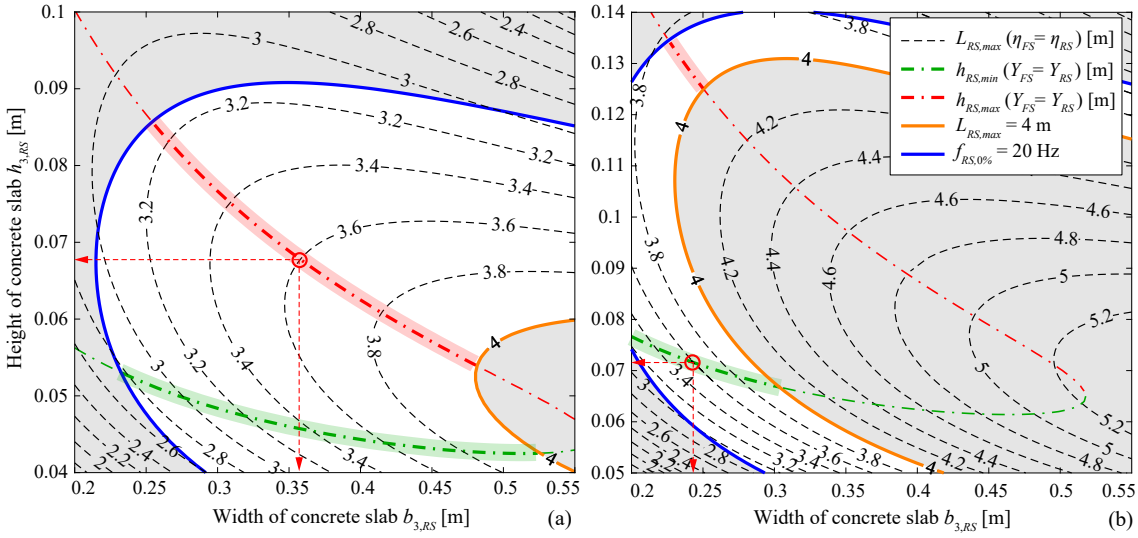

Figure 5.9: Sensitivity analysis performed to obtain the adequate geometry of the RSS. (a) Considering a UPN 140. (b) Considering a UPN 200.

that meet both of these design considerations. Thus, the possible RSSs that fulfill both scale laws and design conditions are comprised within the shaded sections of the green and red lines aforementioned.

It can be observed that in both figures the isoline of $L_{RS,max} = 3.6$ m is more or less equidistant from the blue and the orange lines. For that reason, specimens with this length have been chosen. In the case of a UPN 140 the selected specimen had a $h_{3,RS,max}$ while when using a UPN 200 the selected one had a $h_{3,RS,min}$. Table 5.2 provides a summary of all the selected RSSs with $L_{RS} = 3.6$ using different UPN profiles. All these options have a $Y_{RS} = 1.66$ and a $\eta_{RS,100\%} = 0.145$.

Table 5.2 Different options for the equivalent RSS with $L_{RS} = 3.6$ m and using different UPN profiles

Type	$b_{3,RS}$ **[cm]**	$h_{3,RS}$ **[cm]**	G_2 **[MPa]**	$\eta_{2,ve}$ **[-]**	$f_{RS,100\%}$ **[Hz]**	$f_{RS,0\%}$ **[Hz]**
UPN 140	35.6	6.8	0.752	1.077	13.45	15.06
UPN 160	28.5	9.0	0.848	1.084	16.85	18.90
UPN 180	28.3	6.2	0.762	1.077	14.31	16.08
UPN 200	24.2	7.2	0.827	1.083	16.06	18.05
UPN 220	21.3	8.1	0.873	1.085	17.78	19.98
UPN 240	20.2	8.6	0.900	1.086	18.82	21.16

5.3.5 Final RSS developed adapted to constructive tolerances.

From those RSSs finally proposed in Table 5.2, the option using a UPN 200 was finally selected. To ease the specimen construction, the dimensions of the concrete slab were rounded to $b_{3,RS} = 0.24$ m and $h_{3,RS} = 0.07$ m. Thus, the final geometrical dimensions and predicted modal properties of these RSSs are provided in Tables 5.3 and 5.4, respectively.

Table 5.3 Geometrical description of the RSSs finally constructed

L_{RS} [m]	Profile	$b_{RS,3}$ [m]	$h_{RS,3}$ [m]
3.6	UPN 200	0.24	0.07

Table 5.4 Predicted mechanical and modal parameters of RSSs finally constructed

$\%CLD$	Y_{RS} [-]	f_{RS} [Hz]	η_{RS} [-]	g_{RS}[-]	G_2 [MPa]	$\eta_{2,ve}$ [-]
0% CLD	1.67	17.58	-	-	-	-
50% CLD	1.636	16.57	0.0563	16.57	0.84	1.082
100% CLD	1.636	15.89	0.142	13.96	0.822	1.082

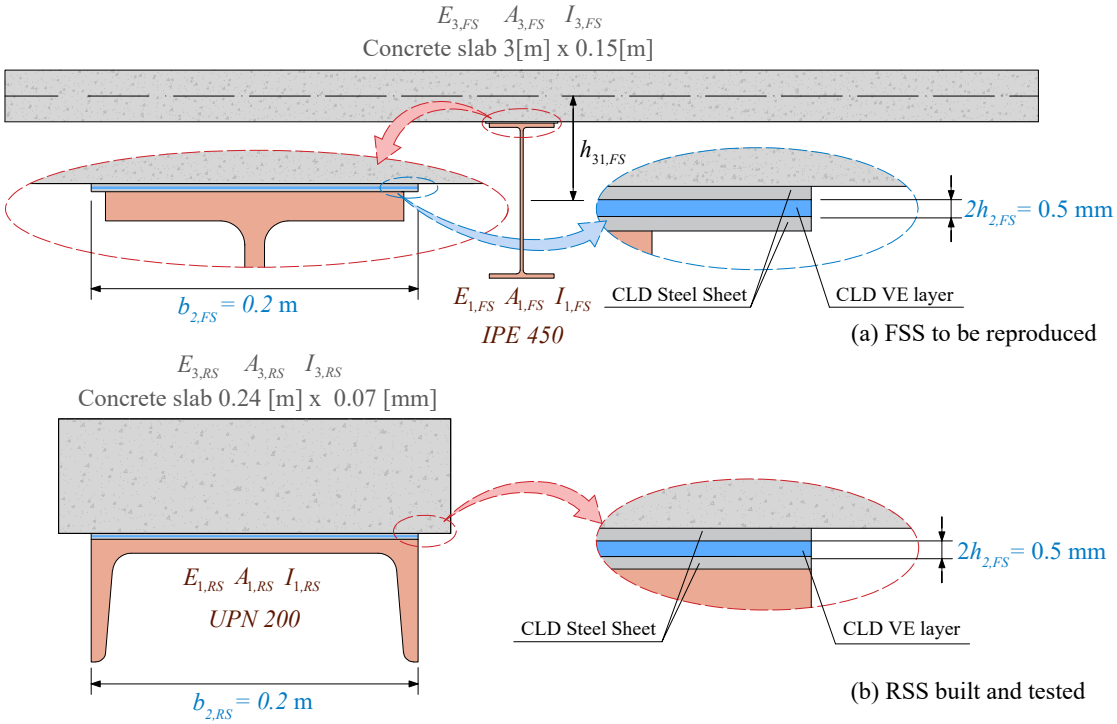

Figure 5.10: Comparison between the 100% CLD FSS that the author aimed to reproduce and RSS finally built for that.

A graphical comparison between the 100% *CLD* FSS and RSS has been depicted in Figure 5.10.

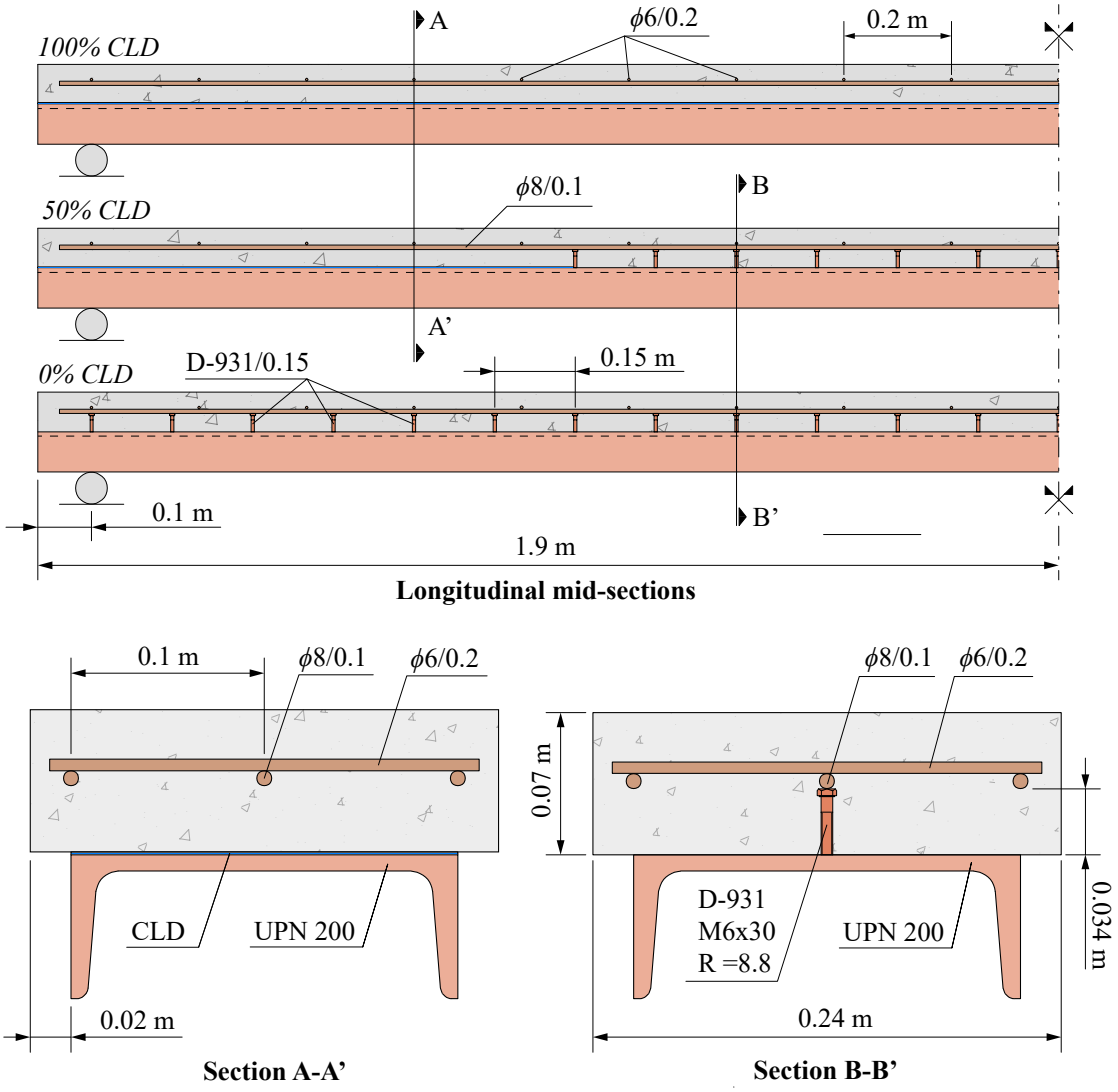

Figure 5.11: Constructive desing of the RSSs finally tested

The final constructive design of the RSSs is provided in Figure 5.11. The following aspects of these designs need to be considered. First, the actual length of the beams is 3.8 m but their span is 3.6 m, thus, a clearance of 0.1 m has been left at each support. Second, the reinforcement of the concrete slab is the minimum one to prevent shrinkage cracking. In this sense a 3 ϕ8 bars have been used as a longitudinal reinforcement, while ϕ 6 bars each 0.2 m have been used in the transversal direction. Finally, the shear connection between

the concrete and the steel has been performed with D-931 bolts of M6x30 metric with Resistance class 8.8. These have a diameter of 6 mm, a height of 30 mm and a Resistance of 800 MPa. They have been disposed each 0.15 m, providing a resistant-enough shear connection for the small force amplitudes tested.

5.3.6 Construction of the RSSs

The main particularity related to the construction of the RSSs has been the use of bonding materials to develop a solid link between the outer steel sheets of the CLD with the concrete slab and the steel profile. In FSSs this link is achieved thanks to the friction developed at these interfaces because of the heavy weight of the slab. This great weight is not present in the RSSs so the bonding was fundamental to achieve a proper deformation of the VE layer, as illustrated in Figure 5.12.

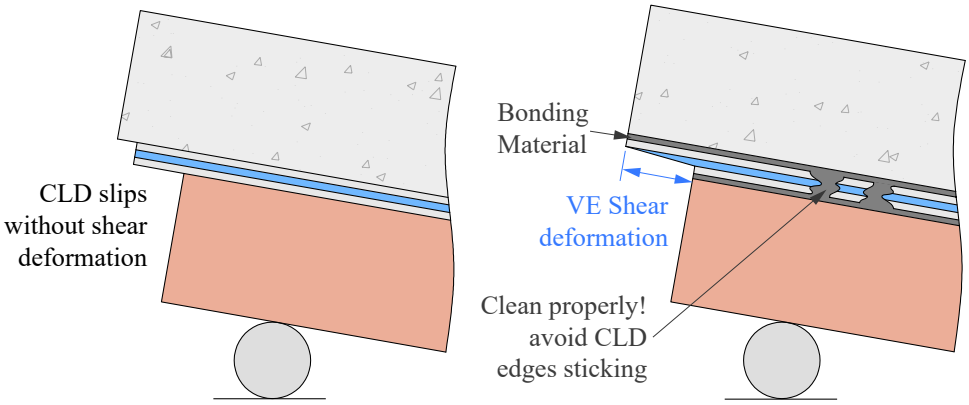

Figure 5.12: Influence of the bonding of the proper functioning of the CLD treatment

The construction process of the RSSs is composed by a series of steps that have been graphically explained in detail in the scheme of Figure 5.13. Additional photos related to this procedure have been included in Figure 5.14. The construction steps are the following ones:

1. Welding of the bolts that serve as shear studs connecting steel and concrete.
2. Building the formwork for the concrete slab. For the 0% CLD specimen, the slab has been casted directly over the steel profile. However, for the specimens with 50 and 100% CLD independent slabs that would be later bonded to the profiles,

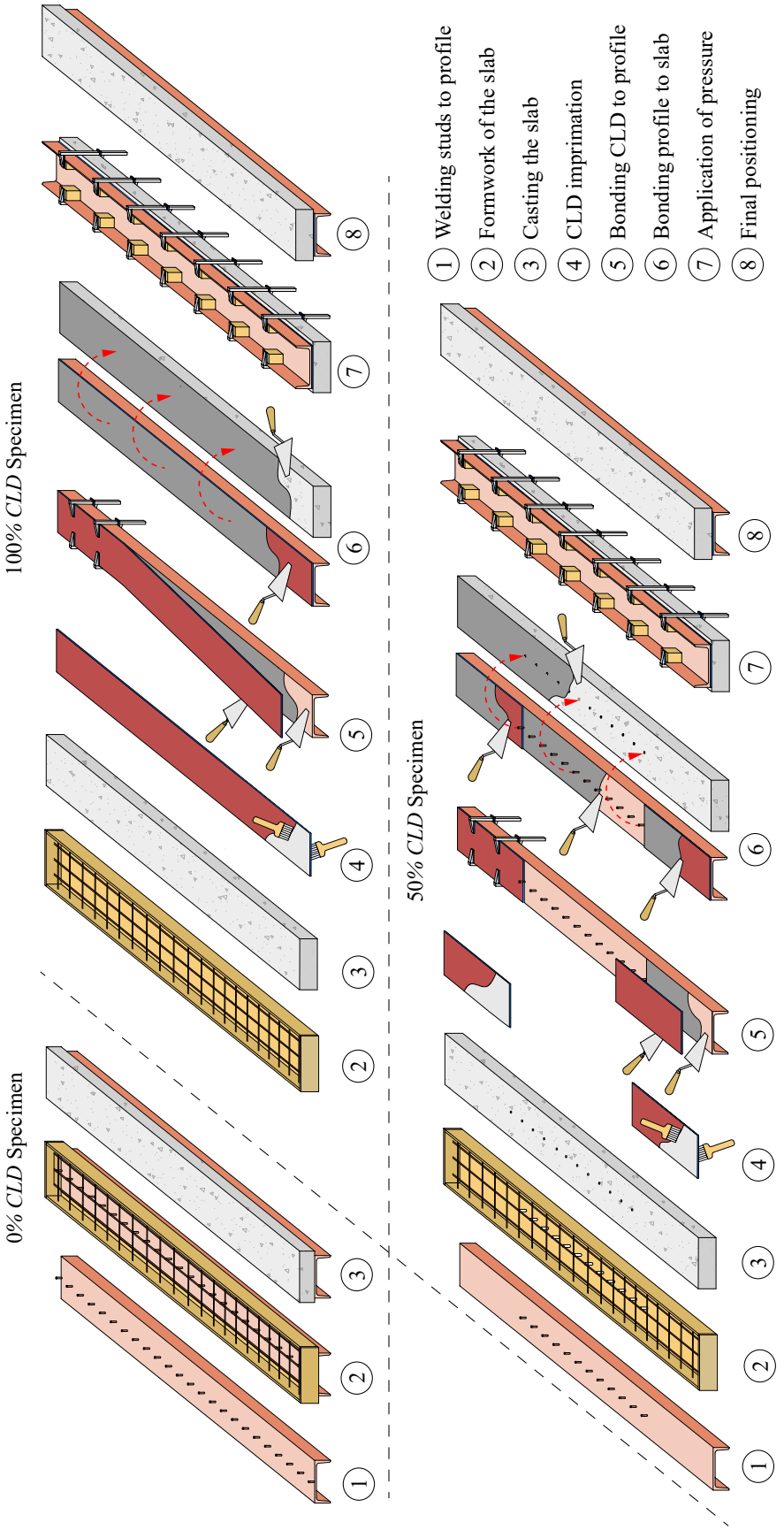

Figure 5.13: Construction process of the RSSs

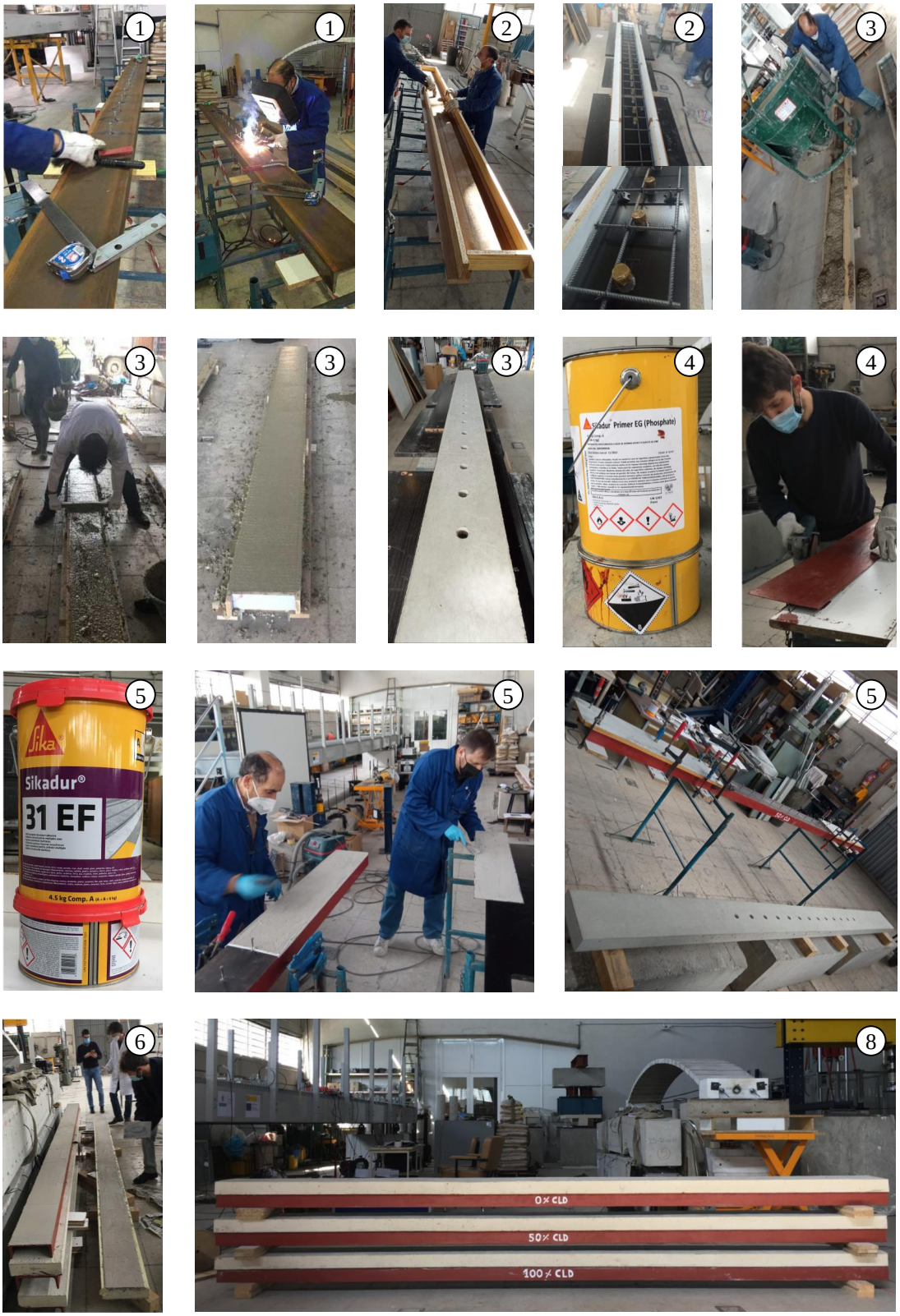

Figure 5.14: Photos related to the construction process of each RSS.

were developed. The 50% CLD slab was provided with a set of holes for later accommodating the shear bolts inside them, when bonding.

3. Pouring the concrete and casting of the slabs. Concrete vibration and surface smoothing is also performed to ensure a right thickness of the slab. The slabs of the specimens with 100 and 50% CLD were left aside during at least one month for them to freely develop their shrinkage before being bonded to the profiles. Due to supply problems, the concrete used on the mechanical

4. Application of primer painting on the two outer faces of the CLD treatment. The product used is Sikadur Primer EG (Phosphate) and it has a characteristic red colour. This primer is capital to achieve a good bonding on the smooth steel surface of the CLD.

5. Bonding of the CLD treatment to the steel beam. First, the steel profile needs to be properly cleaned. The bonding product used in this case was Sikadur 31 EF. This is a two-component epoxy resin that needs to be mixed before being used. The product was applied by means of a trowel in the two faces to be bonded (as the technicians do in the second image corresponding to this step in Figure 5.14). The thickness of the layer applied on each face varied between 0.5 to 1 mm. After joining the two elements, pressure was applied over the joint using woodworking clamps. When doing so, a surplus of product was slowly expelled from the joint. During the next two hours and till the epoxy resin hardened, this surplus needed to be carefully removed and the edge of the CLD treatment were cleaned. This cleaning process is fundamental to avoid the sticking of the two steel sheet of the CLD along their edges, which would ruin the shear deformation of the VE core. This last fact has been highlighted in Figure 5.12.

6. Bonding the concrete slab to the steel profile days after the previous bonding. The same Sikadur was used in this case and a similar procedure was followed. In the case of the 50% CLD beam, the holes left on the slab to accommodate the bolts were also filled with epoxy resin so an adequate functioning of the shear connection was achieved. Then the two elements were adequately bonded positioning each bolt inside its correspondent hole.

7. In this case, the application of pressure was much more severe as the two elements were much stiffer so many sergeant clamps were used. Again, the surplus was correctly cleaned. In this case, in order to achieve a completely cleaned CLD edge, this one was profusely sanded with a grinder radial saw.

8. Final positioning of the beam. The beam is carefully rotated along is longitudinal axis

5.3.7 Concrete mechanical properties

After building the beams, some concrete specimens were tested to know their Young modulus, density and compressive strength. Two different types of concrete were used due to construction planning inconveniences, one for the 0 and 100% CLD beams and a different one for the 50% CLD beam. Three cylindrical specimens were tested for each concrete. The elastic modulus of both materials was similar, however, the one used for the 50% CLD beam displayed a much lower compressive strength. The average mechanical properties of these concrete, E_{cm}, ρ_{cm} and f_{cm}, are summarized in Table 5.5. Regarding the density, an equivalent that considers the effect of the influence, ρ_{ceq} is additionally provided.

Table 5.5 Real mechanical properties of the concrete used on each RSS.

% CLD	E_{cm}[GPa]	ρ_{cm} [kg/m^3]	ρ_{ceq} [kg/m^3]	f_{cm}[MPa]
0% CLD	30.83	2244	2304	29.67
50% CLD	33.46	2211	2290	22.4
100% CLD	30.83	2244	2304	29.67

5.4 Experimentation campaign description

This section describes the experimental campaign performed on each RSS. First, the experimental set-up is introduced, and then, the different tests performed are explained.

5.4.1 Aim and objectives of the tests

The main aim of these tests is to characterize the amount of additional damping ratio provided by the CLD treatment implemented in the RSSs previously built. The following objectives are pursued to achieve this goal:

- Obtain a detailed characterization of the fundamental modal properties of the RSS.

- Characterize the variation of these fundamental modal properties with the amplitude of vibration and with the type of excitation.

5.4.2 Experimental set-up

The set of tests carried out on the RSSs have been designed to pursued the aforementioned objectives. As the main variables of interest are the modal parameters of the RSS under serviceability conditions, their structural collapse is not needed, and therefore, the aimed tests should belong to the category of Non-Destructive testing. The most adequate type of tests to obtain these modal parameters are those belonging to a branch of structural dynamic testing known as Experimental Modal Analysis or EMA. Three elements need to present on a experimental set up that aims to accurately characterize how a structure responds to a given dynamic load i) the structure itself, ii) the measurement of an input dynamic force to the structure, and iii) the measurement of the dynamic response of the structure to that dynamic force. Exactly as in a static test, force and structural response need to be synchronously known to properly characterize the structural behaviour. Knowing this, the experimental set-up designed has been based on the conceptual scheme depicted in Figure 5.15. The RSSs have been disposed as simply supported. A dynamic force has been applied at mid span and five acceleration measurements have been taken at distances of $L/2$, $L/4$ and $L/6$ from the supports.

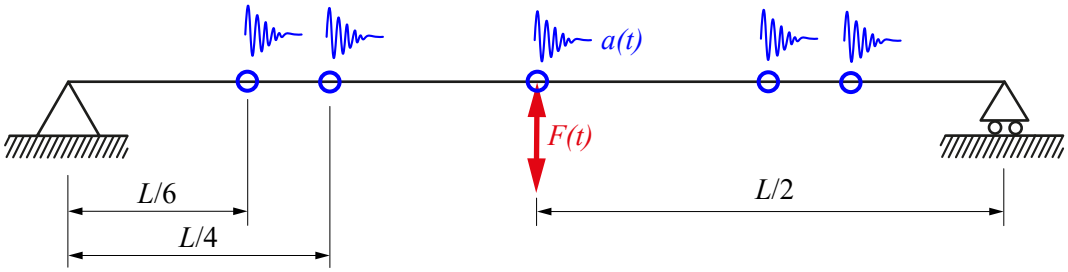

Figure 5.15: Conceptual scheme of the layout conceived for the experimental tests

A detailed scheme of the experimental set-up developed has been included in Figure 5.17. The following subsections will explain the different parts of this scheme.

Force generation and measurement

The dynamic force has been introduced into the structure by means of an electrodynamic shaker. This type of exciter is the most adequate for reproducing dynamic forces with

high frequency content and low amplitude. The electromagnetic working principles of this exciter have been illustrated on Figure 5.16. The shaker is composed of two parts: a moving part with a 'U' shape called 'armature', and a fixed part with a shape of an 8 lay-down called 'body'. Each part has it own coil, thus, there is an static coil on the body and a moving coil on the armature. The static coil is in charge of inducing a magnetic field B on the shaker body due to the Faraday's Law, as indicated in Figure **??**.(a) (where N_{sc} is the number of loop of the static coil, μ is the magnetic permeability and l_{sc} is the length of the cable on the static coil). If in presence of this magnetic field the moving coil is supplied with a current I_{mc}, due to Lorentz's law, the coil will experience an induced mechanical force F as shown in Figure 5.16.(b) (where l_{mc} is the length of the moving coil). Finally, as the moving coil has a certain velocity v, perpendicular to the magnetic field, a back electromotive force $E_{Bemf} = v$ x B, is induced on the moving coil with opposite sign to the one that was initially powered, and with an associated intensity I_{Bemf}, as indicated in Figure 5.16.(c).

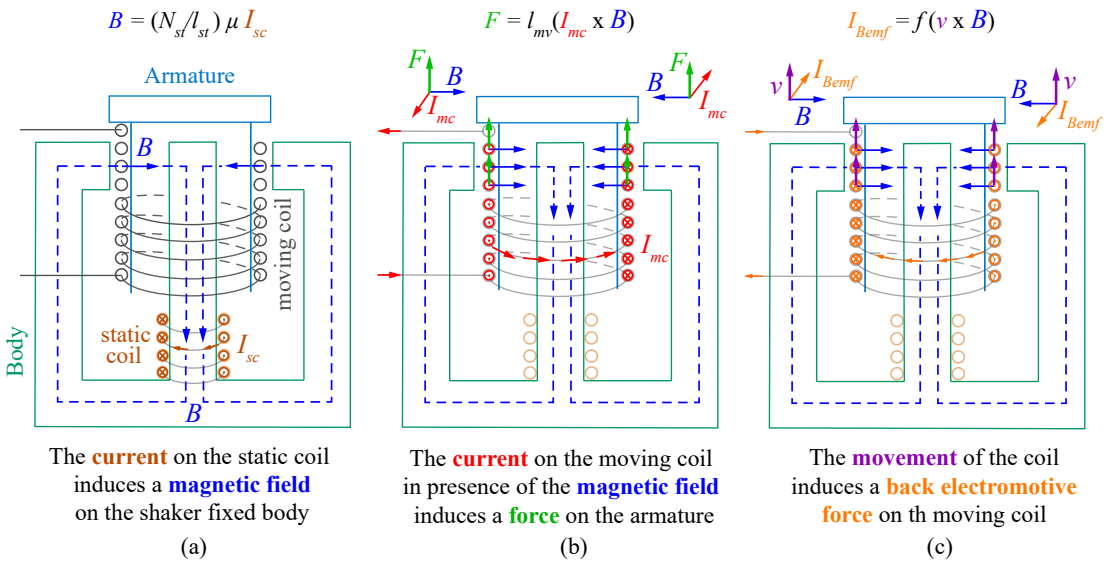

Figure 5.16: Electromagnetic working principles of the electrodynamic shaker.

With this type of exciter, a customized force waveform F may be created through powering the moving coil of the armature with an homothetic waveform in terms of current I_{mc}. A constant gain K_{sh} can be used to obtain the following linear relation between both magnitudes:

$$F = K_{sh} I_{mc} \tag{5.10}$$

The powering current is given to the shaker from an apparatus known as 'power amplifier'. This one has the function of amplifying a weak voltage signal with the desired waveform V_{wf} (traditionally created with an oscilloscope and nowadays with a computer), into a high-amplitude current I_{pa} with the same shape for powering the shaker. This is done applying a constant gain K_{pa} between voltage and current. However, it is important to know that the actual waveform in the moving coil, I_{mc} might not be equal to the desired I_{pa}, as some distortion is always introduced by the back electromotive current I_{Bemf} as indicated below:

$$I_{mc} = I_{pa} - I_{Bemf} \tag{5.11}$$

For that reason, power amplifiers usually have two modes of functioning commonly known as i) voltage mode, and ii) current mode. In 'voltage mode', the distortion introduced by I_{Bemf} is not corrected, and thus, the actual waveform on the moving coil I_{mc} is not proportional to the input V_{wf}. In 'current mode' this distortion is corrected and the proportionality is met. Both approaches are mathematically expressed on the following equations:

$$I_{pa} = K_{pa}V_{wf} \rightarrow I_{mc} = K_{pa}V_{wf} - I_{Bemf} \quad \text{Voltage mode} \tag{5.12a}$$

$$I_{pa} = K_{pa}V_{wf} + I_{Bemf} \rightarrow I_{mc} = K_{pa}V_{wf} \quad \text{Current mode} \tag{5.12b}$$

In these experiments, 'current mode' has been selected to enhance the desired waveform replication on the final force produced by the shaker. This force has not been directly measured with a load cell. Instead, it has been estimated from I_{mc} according to Equation 5.10. The Power amplifier enables monitoring I_{mc} at any moment with a channel that provides a proportional voltage signal called V_{mc} related to the current as follows:

$$I_{mc} = K_{mc}V_{mc} \tag{5.13}$$

Thus, the final force has been estimated from V_{mc} as follows:

$$F = K_{sh}K_{mc}V_{mc} \tag{5.14}$$

To properly use this estimation strategy, two conditions need to be met: i) the shaker must be mounted on the position 'fixed body - free armature'. This means that the shaker

body has to be fixed to the floor and the armature must be connected to the excited structure with a rod, and ii) the internal rubber bands that link the armature with the body need to be removed to not mechanically distort the force introduced on the structure.

The shaker model used is the APS 400 ELECTRO-SEIS® and it has been driven by a compatible power amplifier of the model APS 145. Table 5.6 provides the values of the aforementioned constant gains related these models.

Table 5.6 Gains of the shaker and the power amplifier used.

K_{sh} [N/A]	K_{pa}[A/V]	K_{mc} [A/V]
20.46	7.5	10

Acceleration measurement

The acceleration response of the structure has been measured on 5 structural points. Their location has been selected to capture as well as possible the three first modes of vibration. Despite this, the results shown in this thesis are mainly related to the mid-span measurement. The accelerometers used for the tests are of the model PCB 393-B12. These are sensors of the type IEPE or 'Integrated Electronic Piezoelectric'. This means that signal amplification is already integrated into the sensor and thus, a current needs to be supplied to measure its voltage signal. These accelerometers were chosen because of their great versatility, enabling to measure low ambient vibrations while being also useful to capture higher acceleration up to half of a g. The accelerometers were fixed with magnets to one of the edges of the lower surface of the UPN 200 flange. The main characteristics of these sensors are listed in Table 5.7

Table 5.7 Main characteristics of the accelerometers PCB 393-B12 used on the tests.

Characteristic	Value	Unit
Sensitivity	1000	mV/(m/s^2)
Measurement range	4.9	m/s^2
Resonant Frequency	>10000	Hz
Broad band resolution	0.0008	m/s^2 (rms)
Spectral noise at 10 Hz	3.1	$(\mu$m/s$^2)/\sqrt{\text{Hz}}$

Data acquisition system

The data acquisition system is the set of software and hardware tools used to measure and control electrical signals that represent physical measurements of the structure being tested. This system consists of four elements:

- Computer: its use is fundamental to develop and launch the software prepared for the acquisition task.
- Data acquisition software: as the main elements of the hardware equipment for this purpose were products of 'National Instruments', the software used was LabVIEW. A program based on Real-Time acquisition for NI-CompactRIO was developed.
- Chassis NI CompactRIO-9066: this is the main responsible for organizing and managing the task of acquiring data. Equipped with a real-time processor, it allows for feasible and predictable signal measurements of up to 1000 Hz. Additionally, a versatile FPGA system is available for use in high-speed applications. The chassis has been designed for connection with specialized acquisition modules that measure a varied range of electrical analog signals. The acquisition task can be performed in stand-alone mode, just using the chassis, but in this instance, it was connected to a computer for later post-processing the data.
- Acquisition modules: the data acquisition itself is performed inside these modules. National Instruments provides a wide range of compatible modules for their chassis that can measure various sensor types, such as strain gauges, IEPE sensors, current sensors, voltage sensors, and thermoresistive sensors. Typically, each module includes an analog-to-digital or digital-to-analog converter (ADC or DAC) and, in certain cases, a signal conditioning, an anti-aliasing filter or a power-supplying circuit. Modules can be categorised as 'input' or 'output' modules depending on whether they have an ADC or a DAC, respectively. Input modules collect analogue data and convert it into digital mode for storage, while output modules convert a signal originally digital into analog mode for its transmission. Two types of modules have been used in these tests:
  - NI 9234 input module: this is a four channel module for voltage signal acquisition that enables the channel configuration on IEPE mode. This has been used to measure the accelerometers signals V_a on IEPE mode with AC coupling (removing the constant supply voltage), and also, for acquiring the voltage signal of the shaker V_{mc}, used for estimating its input force.

Table 5.8 Main characteristics of the acquisition modules NI-9234 and NI -9263

Characteristic NI-9234	Value	Unit	Characteristic NI-9263	Value	Unit
Number of channels	4	-	Number of channels	4	-
IEPE	yes	-	-	-	-
Resolution of ADC	24	bit	Resolution of ADC	16	bit
Voltage range	-5/+5	V	Voltage range	-10/+10	V

– NI 9263 output module: This is a four channel module for voltage signal transmission. This module has been used to produce the voltage signal with the adequate waveform V_{wf}, to be later transformed by the power amplifier into a supplying current for the shaker moving coil. The main characteristic of the two described modules are listed in Table 5.8:

5.4.3 Description of the measurement chain

Once that all the elements of the test have been described, the scheme depicted on Figure 5.17 may be fully comprehended. First, a voltage digital signal V_{wf} (light green line) is created on the LabVIEW program launched from the computer. This one is sent to the CompactRIO and is transformed to an analog voltage (red line) on the module NI 9263. This voltage is sent to the power amplifier, which working on current mode (and thus, compensating the effects of the back electromotive force), transforms it into an homothetic current I_{mc} signal (orange thick line) sent to the moving coil of the shaker. Inside the shaker this current induces a proportional force F that excites the beam. The movement of the structure is registered by the accelerometers, and their voltage signals V_a (continuous blue lines) are acquired by module NI-9234, which synchronously also acquires the monitoring voltage of the power amplifier V_{mc} (dashed blue line) that will enable estimating the force. These signals are converted to digital data (dark green lines) in this module and stored on the computer (purple line) for being post processed. Finally, it is important to comment that during the tests, the ambient temperature inside the laboratory of structures, was monitored using the room thermometer.

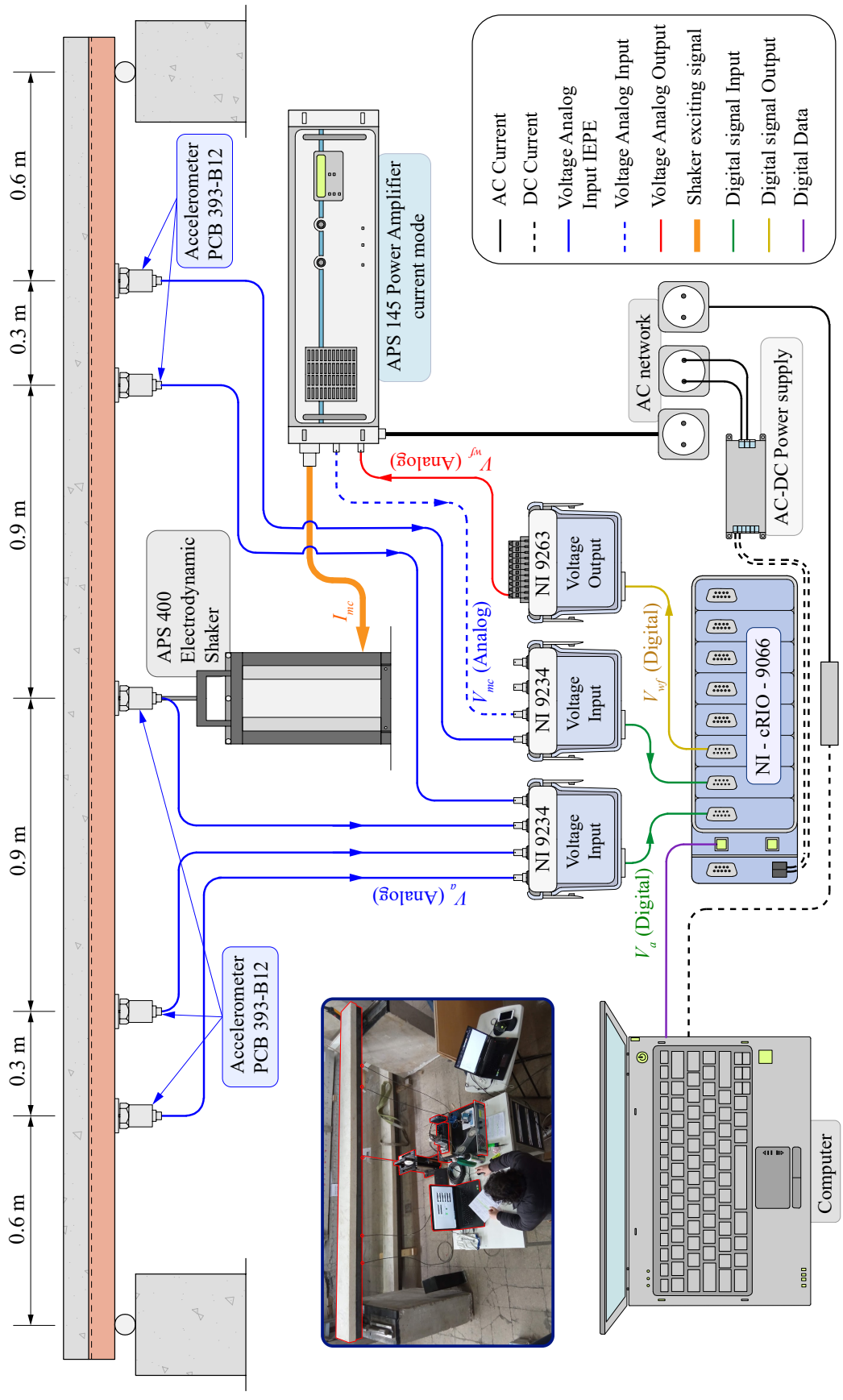

Figure 5.17: Experimental set-up, equipment used, measurement chain and measurement signals.

5.4.4 Experimental tests

Four types of tests have been designed to be carried out on each RSS using the experimental set-up above described. These tests have been described on Figure 5.18. The tests developed are the following ones:

- *EMA with sweep-sine excitation*: This test has been depicted on Figure 5.18.(a). In this case, the shaker has been driven with a sweep-sine signal, most commonly known as 'chirp' signal. This is a periodic and harmonic deterministic signal in which the frequency of the sinusoidal wave f_F continuously varies in time. Its amplitude F_{ss} and its phase ϕ_F have been kept constant during each test. Mathematically the function can be represented as follows:

$$F_{ss}(t) = F_{ss} \sin\left(2\pi f_F(t)t + \phi_F\right), \tag{5.15}$$

  f_F varies linearly in time between two limit frequencies, $f_{F,min}$ and $f_{F,max}$, around $\pm 2; Hz$ the fundamental frequency of the RSS being tested. This variation can be expressed as follows:

$$f_F(t) = f_{F,min} + \left(f_{F,max} - f_{F,min}\right) \frac{t}{T_d}, \tag{5.16}$$

  where T_d corresponds to the duration of the signal equal to 100s. After the force ends, 6 extra seconds are recorded in order for the beam to damp its vibration, so leakage problems are prevented when performing the Fourier transform of the signals.

  Different tests with this configuration have been carried out varying the amplitude of the inputted force F_{ss}, Thus achieving different amplitudes of resonant responses of the fundamental vibration mode. This has been done in order to study the influence of the amplitude of motion in the modal properties of the RSSs.

- *EMA with random excitation*: This test is shown in Figure 5.18.(b). The test is an alternative in which shaker has been powered with a random signal with a uniform frequency content between 1 and 200 Hz. This creates a sort of white or pink noise excitation with a random, ergodic and stationary nature. Again, the duration of each test was 100 s with 6 additional seconds. Additionally, diverse force amplitudes were tested to understand its influence on the dissipation capacity of the VE treatment.

- *Free-decay after impulse excitation*: This test is illustrated on Figure 5.18.(c). Here, each RSS is hit with an soft-tipped hammer, applying an impulse force to the beam.

The response to this force is a free-decaying vibration that may provide a quite reasonable value of the fundamental modal damping of the beam. A test with a duration of 200 s has been developed on each beam. First the beam is struck, then it is allowed to vibrate freely until the response has dissipated, and then the beam is struck again.

- *Operational Modal Analysis (OMA)*: This test corresponds to Figure 5.18.(d). For these tests, the low-amplitude ambient vibration of each RSS has been recorded during 300s. This data has been later analyzed with OMA techniques to extract the fundamental modal properties of each RSS low-amplitude vibration range.

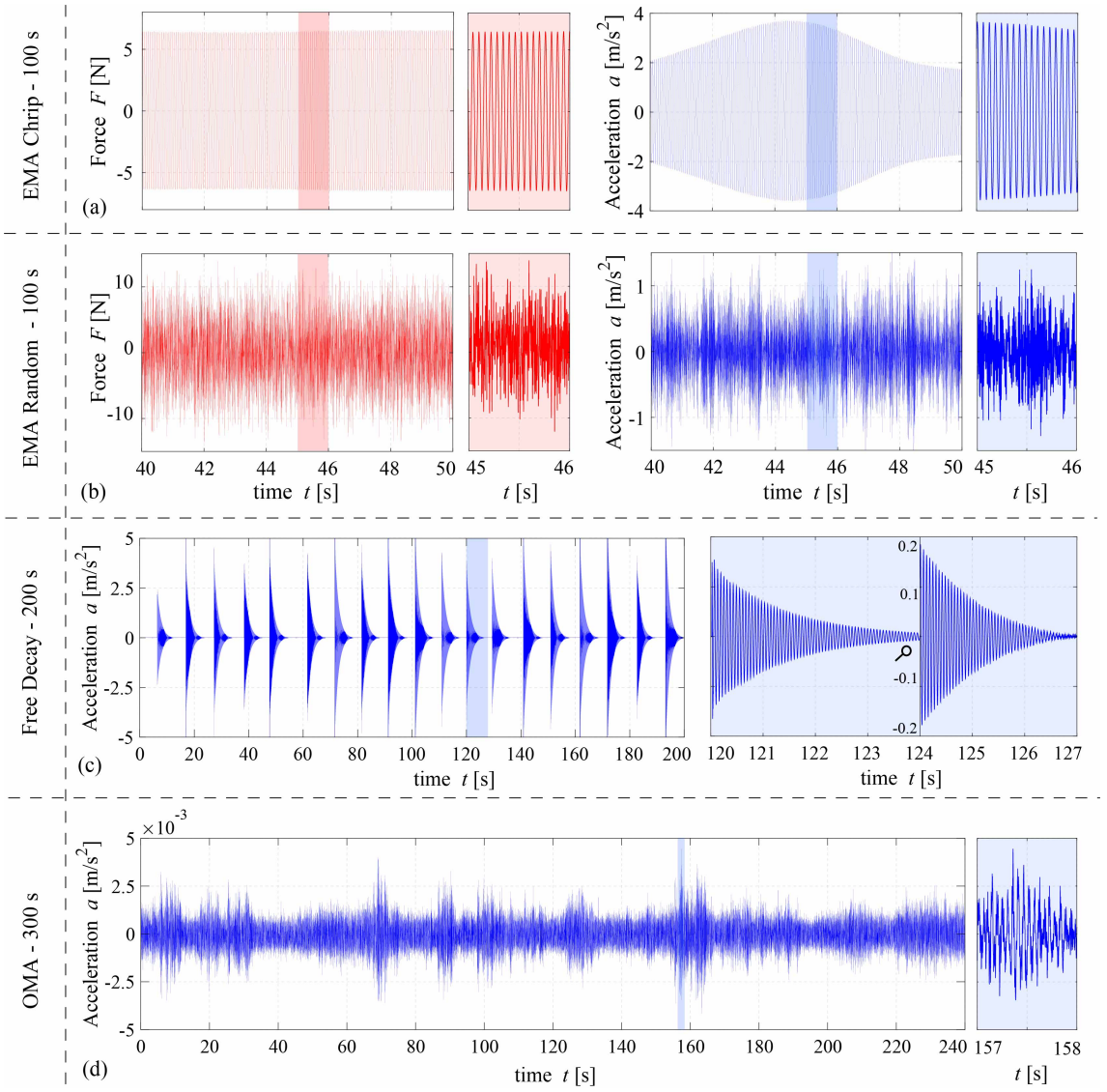

Figure 5.18: Experimental tests performed on each RSS.

5.5 Data Post-processing

The raw data extracted from all these tests are time-domain measurements of two physical magnitudes, either the force F applied to the structure, or the acceleration a experienced by it. The modal properties of the RSS tested have been obtained after careful post-processing of these data. This section will first explain the data treatment performed on each test, to later present the whole set of results obtained for each RSS. Finally, a summary of results will be included.

5.5.1 EMA tests: FRF extraction and modal parameter estimation

The main information to be obtained from this test is the Frequency Response Function (FRF) between the acceleration at mid-span and the applied force at mid-span around the fundamental natural frequency of the RSS tested. Then, this FRF is analyzed to extract the modal parameters of its equivalent SDOF.

Assuming that a given structure is a linear-elastic time-invariant system, implies that if this structure is excited with a stationary harmonic force $F(t) = F\ \sin(\omega t)$ with circular frequency ω, its steady-state response will be also harmonic with the same circular frequency ω and will be of the form $a(t) = a\ \sin(\omega t + \phi_a)$. For fully characterizing $a(t)$ once $F(t)$ is known, two parameters need to be obtained, its amplitude a, and its out-of-phase with respect to the force ϕ_a. As the system is linear, the quotient between the response and force amplitudes, a/F, has to be constant, as double the force, double the response. Therefore, to fully characterize the response, a/F and ϕ_a need to be obtained. The FRF is a function defined in the $\mathbb{R} \rightarrow \mathbb{C}$ space that enables achieving that objective. Its input is a real number with the circular frequency ω, and its output is a complex number which in polar coordinates has a module equal to a/F and a phase equal to ϕ_a. The most common way of graphically expressing this function is the so-called 'bode plot' in which both magnitudes are plotted in the frequency domain. Figure 5.19 provides an example of it for an FRF between a force applied at the mid-span of a simply-supported beam and the acceleration measured at the same location. There, two peaks may be appreciated on the a/F chart, corresponding to the 1^{st} and the 3^{rd} modes of vibration.

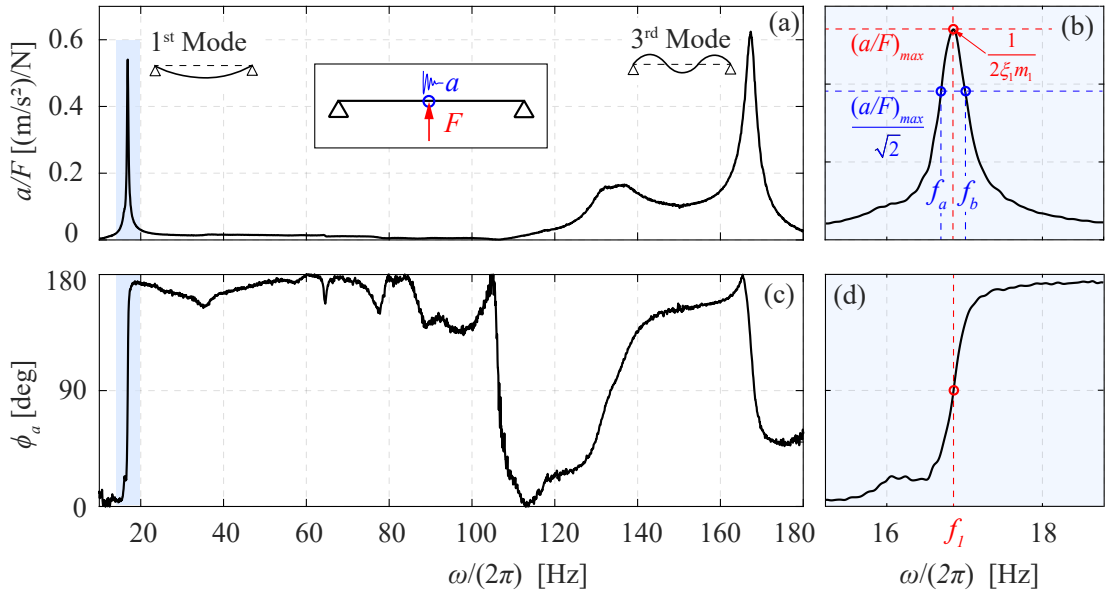

Figure 5.19: Example of a bode plot for a FRF between a force applied at mid span and an acceleration measured at mid span in a simply supported beam .

Experimentally, the FRF relating $a(t)$ and $F(t)$ may be approximated through measuring both signals and dividing their respective Fourier spectra $a(w)$ and $F(\omega)$ as follows:

$$FRF_{a,F} = \frac{a(\omega)}{F(\omega)} \tag{5.17}$$

This approximation works well if the Fourier spectra performed are clear. For that, the measurements need to be long, leakage causes should be avoided and sensors used should have reduced noise. Alternative predictions that reduce the influence of noise in the FRF prediction are the following ones:

$$FRF_{a,F-1} = \frac{a(\omega)F(\omega)}{F(\omega)F(\omega)} \tag{5.18a}$$

$$FRF_{a,F-2} = \frac{a(\omega)a(\omega)}{F(\omega)a(\omega)} \tag{5.18b}$$

On the one hand, $FRF_{a,F-1}$ is used when all the noise is assumed to be concentrated on the response signal. Thus the uncorrelated noise with the force signal is averaged at the numerator multiplication. On the other hand, when noise is concentrated on the force signal, $FRF_{a,F-2}$ should be used. For this study $FRF_{a,F-1}$ estimator has been chosen.

Additionally, a coherence function has been obtained together with each FRF estimated. This enables knowing the degree of correlation between the structural response and the force causing it. The coherence function has been computed according to:

$$C_{a,F} = \frac{|a(\omega)F(\omega)a(\omega)F(\omega)|}{a(\omega)a(\omega)F(\omega)F(\omega)} \tag{5.19}$$

FRFs with sweep-sine excitation

Using this type of excitation, the Fourier spectra of the force and response signals are only well defined within the test frequency range between $f_{F,min}$ and $f_{F,max}$. If the test has been properly developed, with recorded signals starting and ending at zero levels to avoid spectrum leakage, the FRF will result considerably clean within this range, but extremely noisy out of it. In this case, FRF averaging between identical tests (which is sometimes performed to obtain cleaner results) can be dispensed with due to the accuracy obtained from a single test.

FRFs with Random excitation

When using random excitation, the FRF is well defined within the whole range of frequencies contained in the random force (in this case, up to 200 Hz), however, the level of uncorrelated noise on the recorded signals is higher, and thus, the resulting FRF can be considerably noisy. To avoid this, averaging is performed. For that, the original 100 s signal is divided into 5 sections of 100/3 s with an overlapping between them of 100/6 s. In this way, 5 independent FRFs may be estimated for being later averaged. Nevertheless, spectral leakage problems may arise from this strategy, as the signal sections are directly extracted from the original one, and thus, they do not start and end at zero level. To overcome this, a Hamming window is applied to both the force and response signal sections before performing their spectra. This process has been depicted in Figure 5.20

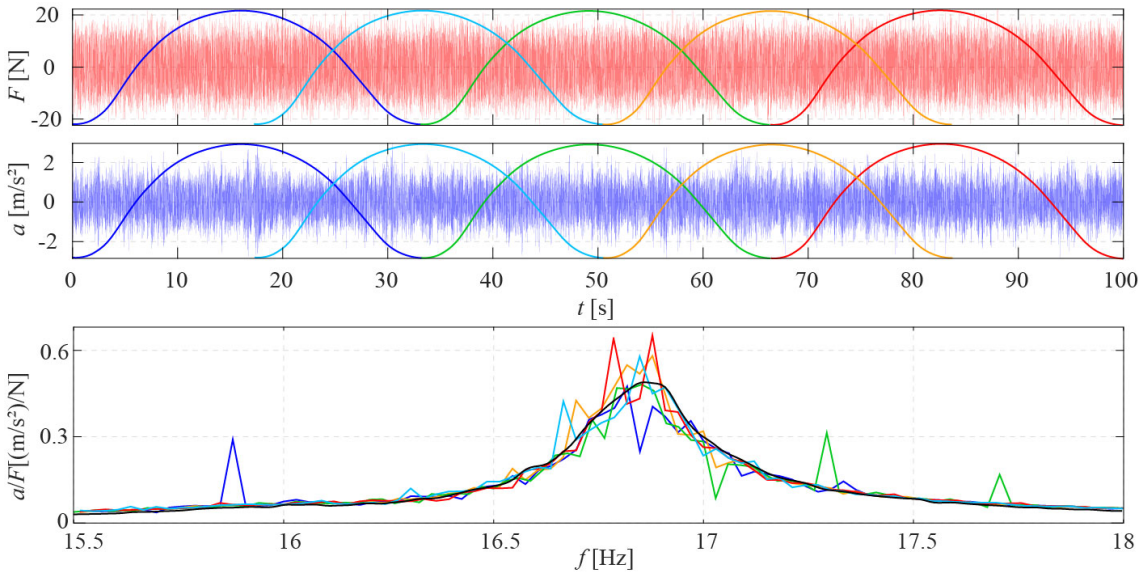

Figure 5.20: FRF extraction for EMA tests with random excitation

EMA test: Modal parameter estimation

If the natural frequencies are sufficiently spaced, each peak of the FRF can be well approximated by the FRF of an equivalent SDOF with the same natural frequency and damping ratio. Based on this fact, the modal characteristics of this SDOF can be estimated from the FRF following a three-step approach explained below:

1. *Fundamental natural frequency* f_1: This frequency is the one at which the phase ϕ_a between the force and the acceleration is 90º (as shown in Figure 5.19.(d). Additionally, at this frequency, the module of the FRF should be maximum.

2. *Damping ratio* ξ_1: This value has been estimated by making use of the so-called 'half power method' (which has been illustrated in Figure 5.19.(b)). In the vicinity of the FRF peak, there are two other points with amplitude equal to the maximum one divided by $\sqrt{2}$. These points are located at frequencies f_a and f_b in ascending order. Considering this, the damping ratio of the equivalent SDOF may be estimated as indicated below:

$$\xi_1 = \frac{f_b - f_a}{2f_1} \tag{5.20}$$

3. *Equivalent mass* m_1: This parameter is estimated knowing the expression for the maximum amplitude of the FRF as follows:

$$(a/F)_{max} = \frac{1}{2\xi_1 m_1} \Rightarrow m_1 = \frac{1}{2\xi_1 (a/F)_{max}} \tag{5.21}$$

5.5.2 Free-decay test post-processing

This is an output-only test in which f_1 and ξ_1 have been estimated as a function of the amplitude of vibration. To achieve that objective, first, the different free-decaying responses caused by each hit were isolated and filtered with a band-pass filter adjusted to the fundamental frequency of the beam. Then, the cycle peaks (positive and negative) of the filtered decaying signal, a_p were identified and used to estimate the damping ratio and the fundamental frequency of the beams. The very first peaks of the decay have been always discarded, as the contribution of higher vibration modes to the dynamic response is not negligible here. This estimation has been carried out repeatedly every few number of cycles N, as highlighted in Figure 5.21 using arrows. Within each set of N consecutive cycles three variables have been computed:

- The mean value of the maximum amplitude of vibration $a_{max,d}$ obtained as follows:

$$a_{max,d} = \frac{a_{p,1} + a_{p,N+1}}{2} \tag{5.22}$$

  where $a_{p,1}$ and $a_{p,1+N}$ are the first and the last peaks of the set.

- The damping ratio ξ_1 calculated using the formula of the logarithmic decrement considering its simplification for damping ratios lower than 10%:

$$\xi_1 = \frac{1}{2\pi N} \ln\left(\frac{a_{p,1}}{a_{p,N+1}}\right) \tag{5.23}$$

- The fundamental frequency has been derived using the times of the first and the last peak of the set, $t_{p,1}$ and $t_{p,N+1}$, respectively:

$$f_1 = \frac{N}{t_{p,N+1} - t_{p,1}} \tag{5.24}$$

This process has been repeated for consecutive sets of N cycles, as depicted in Figure 5.21. As a consequence, this analysis has enabled knowing how f_1 and xi_1 change with the amplitude of motion.

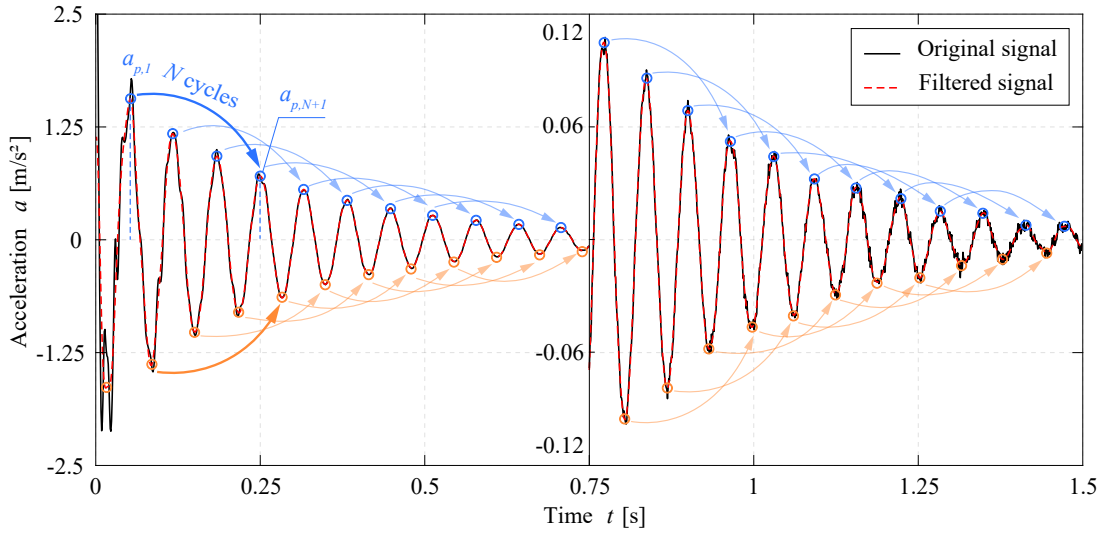

Figure 5.21: Post-processing performed to free-decay signals

5.5.3 OMA tests

The raw data extracted from the OMA tests is the ambient response of the 5 accelerometers used on the tests. Before treating this data with an OMA algorithm the measured signals need to be first filtered and then decimated. A low-pass filter with a cut frequency of 50 Hz was applied, later a decimation factor of 5 was used, so the final signal analyzed had a sampling frequency of 200 Hz. This data was then treated with the SSI-cov OMA algorithm in the commercial software MACEC, to obtain f_1 and ξ_1. The main parameters used for the detection of stable poles within the OMA analysis are the following ones:

- Frequency stabilization criteria: 2%
- Damping stabilization criteria: 5%
- Mode-shape stabilization criteria: 1%
- Damping Ration lower bound: 0%
- Damping ratio upper bound: 10%
- Number of times of a repeated pole to be considered as stable: 50

5.6 Experimental Results

This section provides the experimental results organized by way of a report. These results belong to the set of tests summarized in the following Table 5.9.

Table 5.9 Set of experimental tests performed on the RSSs.

RSS tested	**Tests performed**	**Temperature**
0% CLD	EMA: Sweep-sine at various amplitudes EMA: Random at various amplitudes Free-Decay OMA	15ºC
50% CLD	EMA: Sweep-sine at various amplitudes EMA: Random at various amplitudes Free-Decay OMA	15ºC
50% CLD	EMA: Sweep-sine at various amplitudes EMA: Random at various amplitudes Free-Decay	20ºC
100% CLD	EMA: Sweep-sine at various amplitudes EMA: Random at various amplitudes Free-Decay OMA	10ºC
100% CLD	EMA: Sweep-sine at various amplitudes EMA: Random at various amplitudes Free-Decay	20ºC

The testing of the same RSS at two different temperatures was performed to verify the influence of the temperature-dependant mechanical behaviour of the VE layer on the final modal properties, ξ_1 and f_1, of the beams. The temperature was measured using the laboratory thermometer, not internal thermocouple sensors. The tests were performed at winter time. For the low-temperature tests, the heating system was turned off, and the tests were performed in the early morning. For the 20ºC tests, the heating system of the lab was turned off and the room was pre-heated during 7 hours before performing the tests. These were developed at mid-day.

The results derived from the OMA tests are presented all together in a final subsection. Nevertheless, the results from the EMA and free-decay tests are jointly presented in different subsections coinciding with the rows of Table 5.9. One of these subsections,

for example, presents the EMA and free-decaying results for the RSS with 50% CLD tested at 15ºC. Each one of these subsections presents the following information:

- Two charts with the FRFs obtained in the EMA tests for different amplitudes of motion as those provided Figure 5.22. The left plot (5.22.(a)) corresponds to the FRFs from the sweep-sine excitation, and the right one (5.22.(b)) for the random excitation. Under each chart, the respective coherence plots of the tests have been included (Figures 5.22.(c) and (d)).
- A table with the modal parameters extracted from the FRFs with sweep-sine excitation (Table 5.10). The parameter F_{ss} in this table, represents the maximum amplitude of the sweep-sine force, and a_max_{ss} is the maximum response amplitude registered on the test.
- A table with the modal parameters extracted from the FRFs with Random excitation. (Table 5.11). The parameter F_r, represents the maximum amplitude of the band-pass filtered force signal around the natural frequency of the beam tested. Again, a_max_r is the maximum response amplitude band-pass filtered in the same way as the force.
- Four charts depicting the results of the free-decay tests (as those included in Figure 5.23).
  - *Top-left chart*: provides a plot of the free-decaying response with higher initial amplitude from those recorded. The envelopes of the other free-decays have been overlapped in the plot (blue lines have been used for positive envelopes, and yellow lines for negative ones). A zoom of the last part of the decay is also included (Figure 5.23.(a)).
  - *Top-right chart*: depicts the variation of ξ_1 with respect to the acceleration $a_{max,d}$ (Figure 5.23.(b)). The parameter $a_{max,d}$ was already described in Equation 5.22.
  - *Bottom-right chart*: shows the same information as the Top-right chart but the with $a_{max,d}$ expressed in logarithmic scale (Figure 5.23.(d)).
  - *Bottom-left chart*: illustrates the variation of f_1 with respect to $a_{max,d}$ also expressed in logarithmic scale (Figure 5.23.(c)).

The results of the EMA and free-decay tests are below included from subsections 5.6.1 to 5.6.5.

5.6.1 Results of 0% CLD RSS

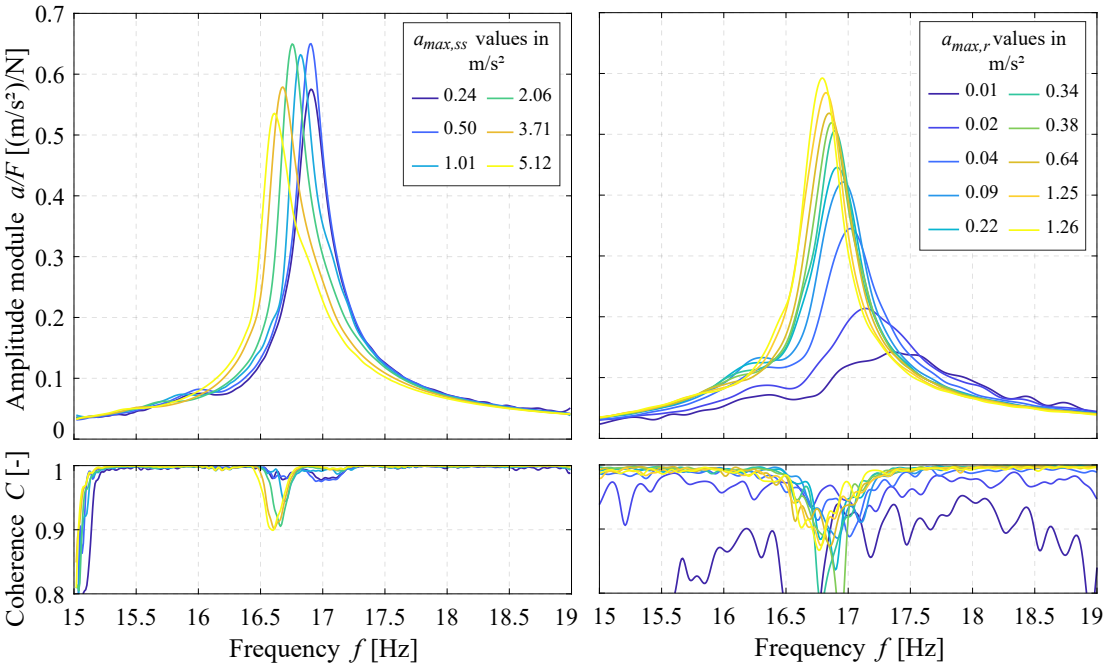

Figure 5.22: FRFs of RSS with 0% *CLD*

Table 5.10 Modal properties of the FRFs obtained with sweep-sine excitation for the 0% *CLD* RSS

F_{ss} [N]	$a_{max,ss}$ [m/s^2]	$\xi_{1,0\%}$ [%]	$f_{1,0\%}$ [Hz]	$m_{1,0\%}$ [kg]
0.42	0.24	0.64	16.90	134
0.84	0.50	0.56	16.91	134
1.64	1.01	0.55	16.83	142
3.25	2.06	0.59	16.56	130
6.48	3.71	0.69	16.67	124
9.72	5.12	0.70	16.60	133

Table 5.11 Modal properties of the FRFs obtained with random excitation for the 0% *CLD* RSS

F_r [N]	$a_{max,r}$ [m/s^2]	$\xi_{1,0\%}$ [%]	$f_{1,0\%}$ [Hz]	$m_{1,0\%}$ [kg]
0.15	0.01	2.82	17.37	122
0.30	0.02	1.85	17.15	124
0.59	0.04	1.13	17.04	127
1.17	0.09	1.03	16.98	114
2.35	0.22	0.98	16.93	114
3.52	0.34	0.75	16.88	129
4.68	0.38	0.76	16.90	124
7.05	0.64	0.92	16.86	100
11.63	1.25	0.84	16.84	101
14.66	1.26	0.79	16.82	105

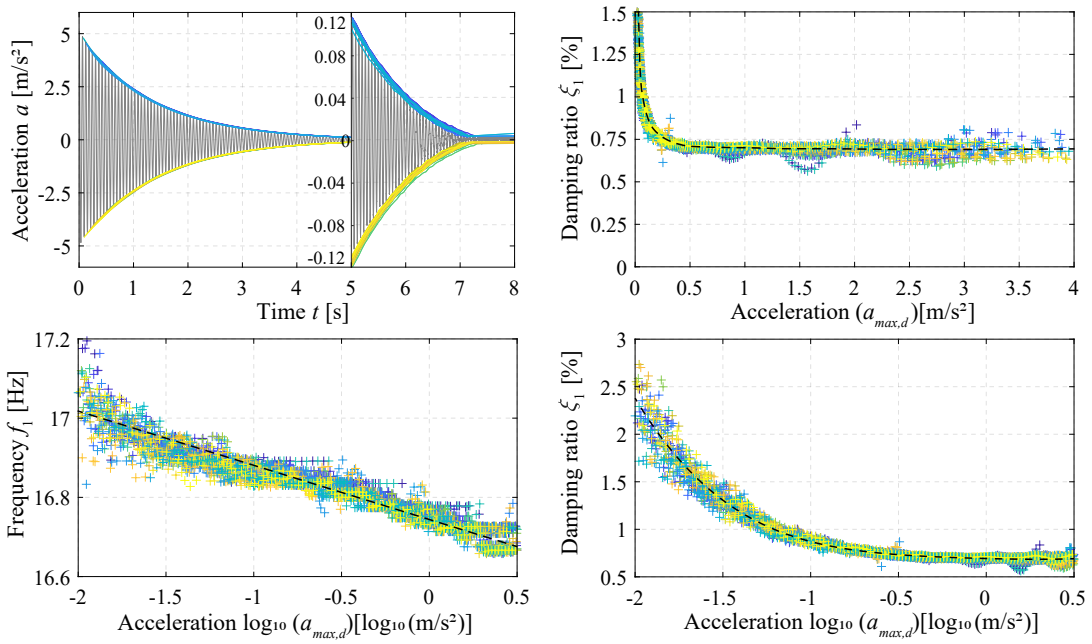

Figure 5.23: Experimental Results for free-decay test on the 0% *CLD* RSS

5.6.2 Results of 50% CLD RSS tested at 15ºC

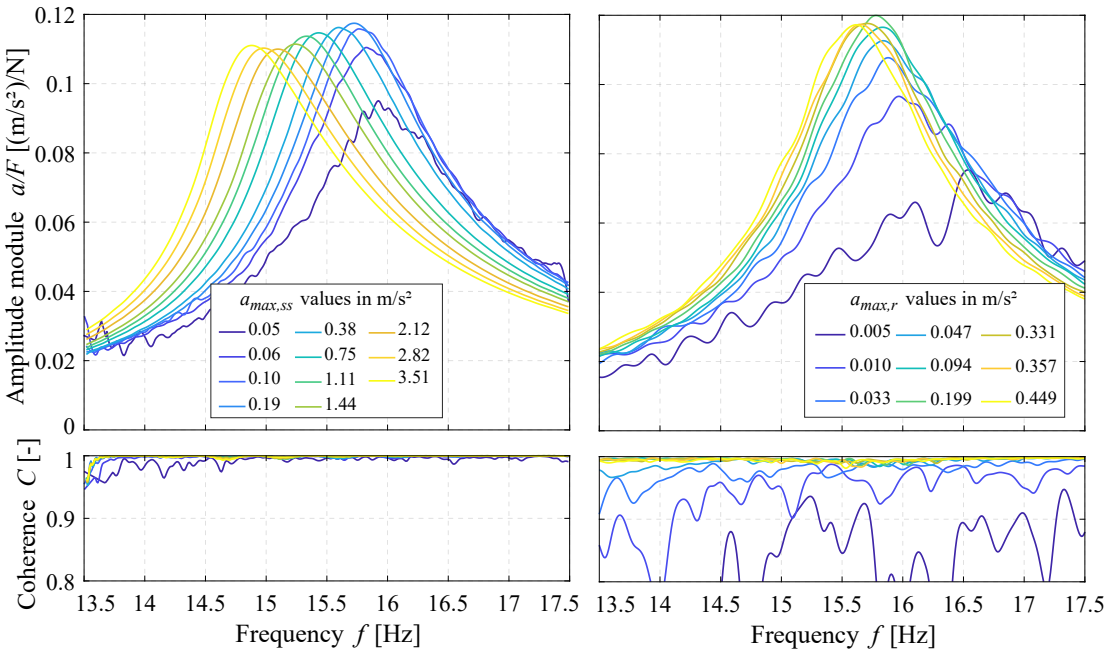

Figure 5.24: FRFs of RSS with 50% *CLD* tested at 15º.

Table 5.12 Modal properties of the FRFs obtained with sweep-sine excitation for the 50% *CLD* RSS tested at 15ºC

F_{ss} [N]	$a_{max,ss}$ [m/s^2]	$\xi_{1,0\%}$ [%]	$f_{1,0\%}$ [Hz]	$m_{1,0\%}$ [kg]
0.57	0.06	3.48	15.78	128
0.93	0.10	3.30	15.77	128
1.72	0.19	3.31	15.71	125
3.34	0.38	3.48	15.66	122
6.58	0.75	3.65	15.39	120
9.81	1.11	3.53	15.31	123
13.07	1.44	3.64	15.24	121
19.52	2.12	3.79	15.19	120
26.01	2.82	3.89	14.92	118
32.48	3.51	3.69	14.84	121

Table 5.13 Modal properties of the FRFs obtained with random excitation for the 50% *CLD* RSS tested at 15ºC

F_{ss} [N]	$a_{max,r}$ [m/s^2]	$\xi_{1,0\%}$ [%]	$f_{1,0\%}$ [Hz]	$m_{1,0\%}$ [kg]
0.16	0.005	4.80	16.51	135
0.31	0.01	4.18	15.95	121
0.67	0.03	4.04	15.83	114
1.24	0.05	3.83	15.84	116
2.52	0.09	3.69	15.81	115
5.59	0.20	3.48	15.82	120
7.25	0.33	3.59	15.71	118
11.05	0.36	3.54	15.65	120
11.96	0.45	3.61	15.60	118

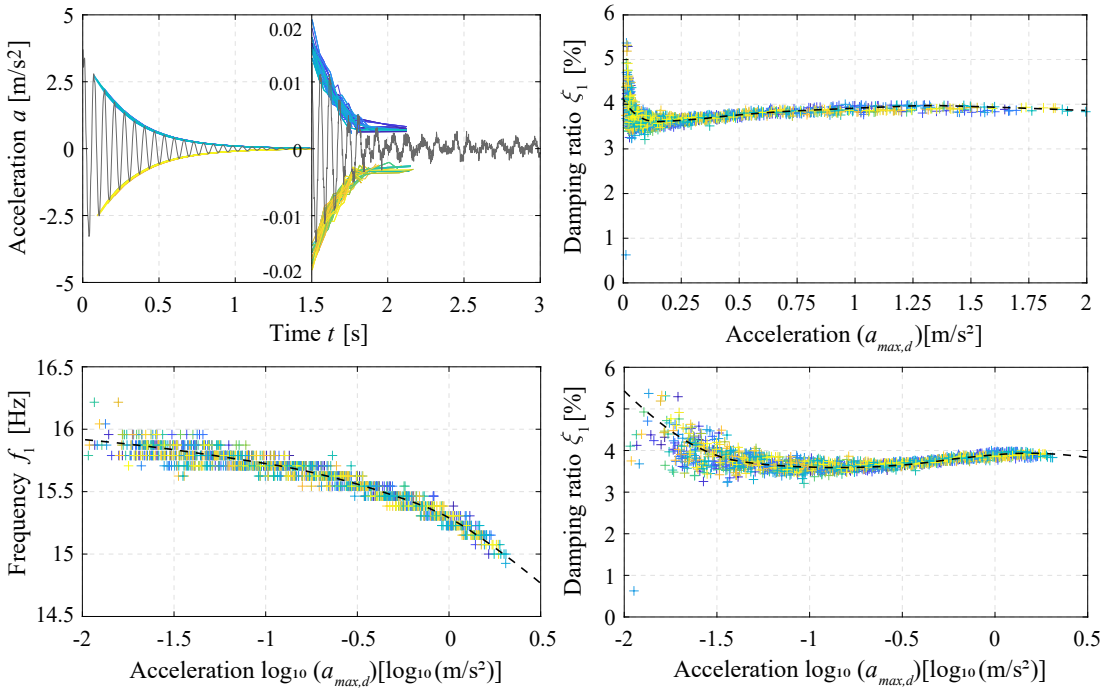

Figure 5.25: Experimental Results for free-decay test on the 50% *CLD* RSS tested at 15ºC

5.6.3 Results of 50% CLD RSS tested at 20ºC

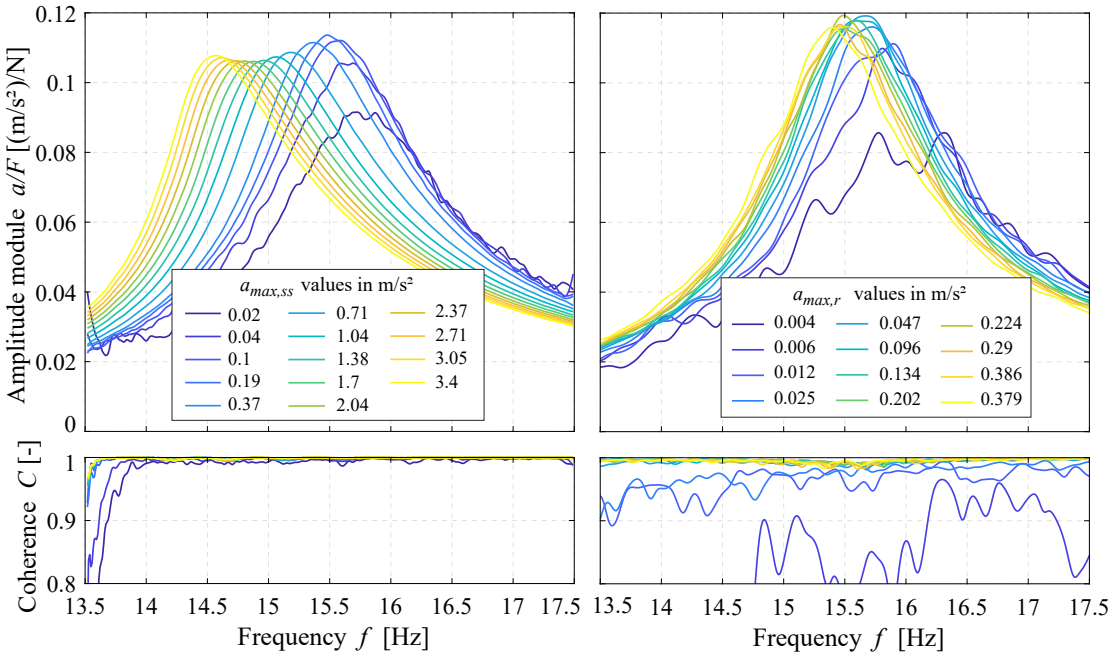

Figure 5.26: FRFs of RSS with 50% *CLD* tested at 20º.

Table 5.14 Modal properties of the FRFs obtained with sweep-sine excitation for the 50% *CLD* RSS tested at 20ºC

F_{ss} [N]	$a_{max,ss}$ [m/s^2]	$\xi_{1,0\%}$ [%]	$f_{1,0\%}$ [Hz]	$m_{1,0\%}$ [kg]
0.28	0.02	4.12	15.72	131
0.47	0.04	3.61	15.70	129
0.95	0.10	3.57	15.65	124
1.18	0.19	3.69	15.48	121
3.38	0.37	3.64	15.31	122
6.60	0.71	3.72	15.19	132
13.09	1.38	4.00	14.92	119
16.31	1.70	3.88	14.84	121
22.79	2.37	3.84	14.72	122
26.08	2.71	3.82	14.72	122
32.51	3.40	3.97	14.71	120

Table 5.15 Modal properties of the FRFs obtained with random excitation for the 50% *CLD* RSS tested at 20ºC

F_{ss} [N]	$a_{max,r}$ [m/s^2]	$\xi_{1,0\%}$ [%]	$f_{1,0\%}$ [Hz]	$m_{1,0\%}$ [kg]
0.14	0.006	4.66	15.81	123
0.31	0.012	3.24	15.81	139
0.66	0.025	3.69	15.91	122
1.66	0.05	3.52	15.71	122
2.37	0.10	3.44	15.62	122
3.72	0.13	3.49	15.61	121
5.16	0.20	3.52	15.57	121
6.08	0.22	3.59	15.47	119
7.93	0.29	3.41	15.45	123
9.84	0.38	3.51	15.44	121
10.72	0.38	3.51	15.43	123
14.90	0.52	3.46	15.40.	124

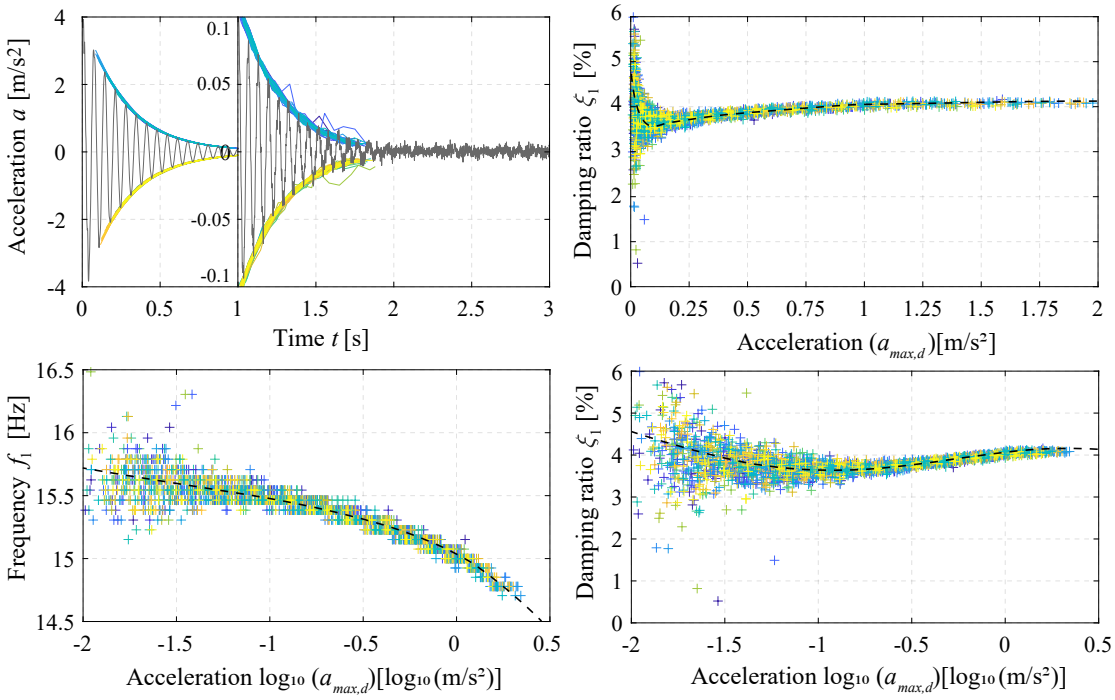

Figure 5.27: Experimental Results for free-decay test on the 50% *CLD* RSS tested at 20ºC

5.6.4 Results of 100% CLD RSS tested at 10ºC

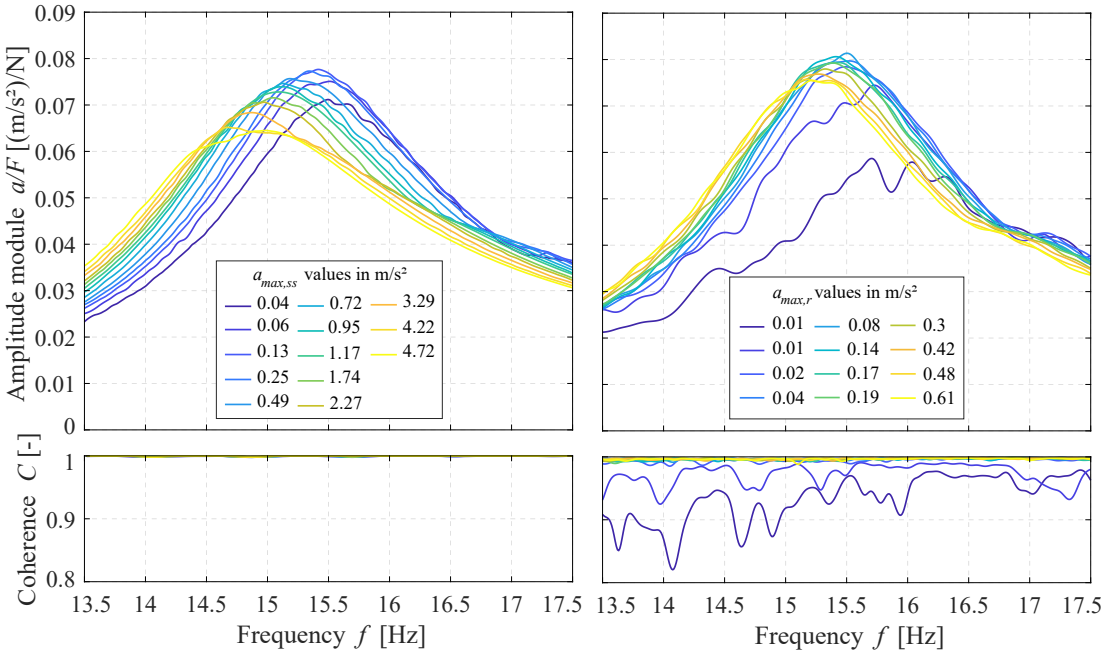

Figure 5.28: FRFs of RSS with 100% *CLD* tested at 10º.

Table 5.16 Modal properties of the FRFs obtained with sweep-sine excitation for the 100% *CLD* RSS tested at 10ºC

F_{ss} [N]	$a_{max,ss}$ [m/s^2]	$\xi_{1,0\%}$ [%]	$f_{1,0\%}$ [Hz]	$m_{1,0\%}$ [kg]
0.42	0.04	5.44	15.48	128
0.84	0.06	5.45	15.55	122
1.64	0.13	5.37	15.43	120
3.25	0.25	5.50	15.33	117
6.47	0.49	5.74	15.22	115
9.70	0.72	5.85	15.13	114
12.92	0.95	5.84	15.11	116
16.14	1.17	5.93	15.11	116
24.20	1.17	6.15	15.04	114
32.26	2.27	6.45	14.99	109
48.34	3.29	6.92	14.88	105
64.45	4.21	7.55	14.70	101
72.47	4.72	7.57	15.00	102

Table 5.17 Modal properties of the FRFs obtained with random excitation for the 100% *CLD* RSS tested at 10ºC

F_r [N]	$a_{max,r}$ [m/s^2]	$\xi_{1,100\%}$ [%]	$f_{1,100\%}$ [Hz]	$m_{1,100\%}$ [kg]
0.15	0.005	5.95	15.72	139
0.30	0.01	5.21	15.70	128
0.59	0.02	5.27	15.47	120
1.18	0.04	5.24	15.57	119
2.35	0.08	5.10	15.49	119
3.51	0.14	5.14	15.42	120
5.87	0.19	5.24	15.40	120
8.78	0.30	5.37	15.30	119
11.76	0.42	5.55	15.26	117
14.63	0.48	5.62	15.16	117
17.50	0.61	5.62	15.16	117

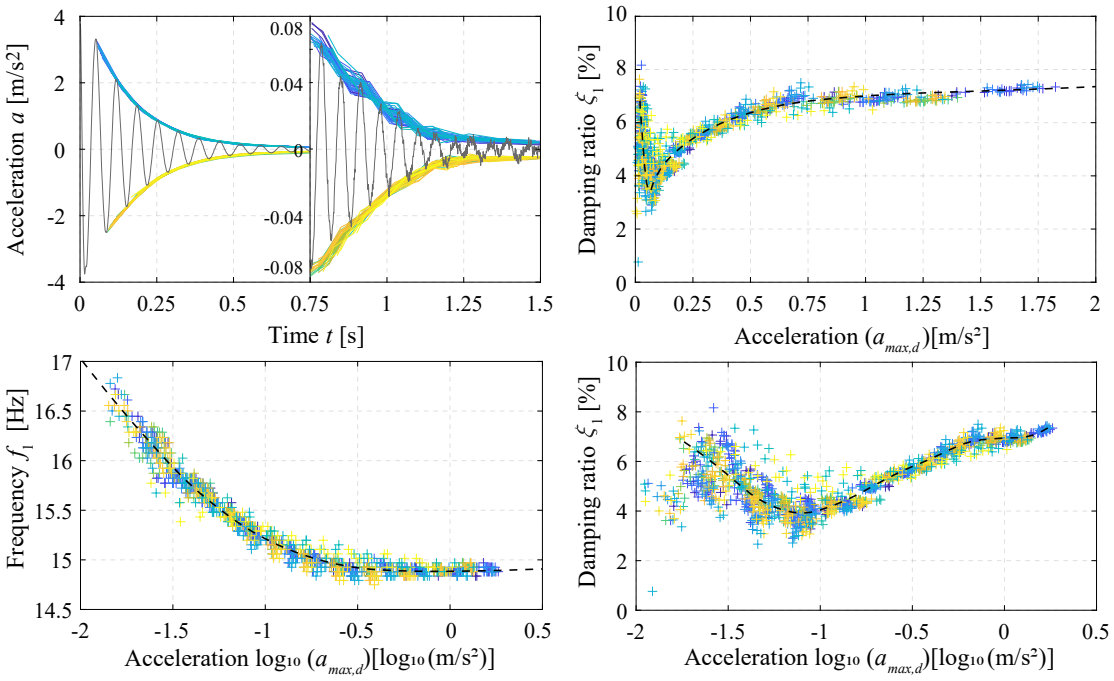

Figure 5.29: Experimental Results for free-decay test on the 100% *CLD* RSS tested at 10ºC

5.6.5 Results of 100% CLD RSS tested at 20ºC

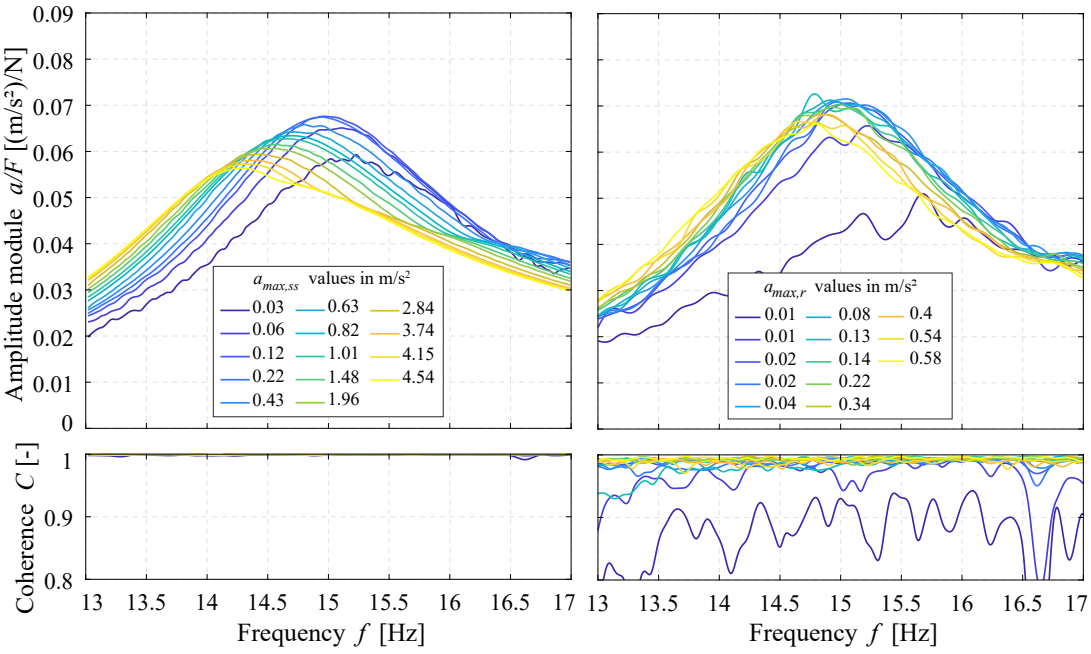

Figure 5.30: FRFs of RSS with 100% CLD tested at 20º.

Table 5.18 Modal properties of the FRFs obtained with sweep-sine excitation for the 100% CLD RSS tested at 20ºC

F_{ss} [N]	$a_{max,ss}$ [m/s^2]	$\xi_{1,100\%}$ [%]	$f_{1,100\%}$ [Hz]	$m_{1,100\%}$ [kg]
0.43	0.03	6.48	15.11	128
0.84	0.06	6.35	15.09	120
1.64	0.12	6.36	14.98	116
3.25	0.22	6.46	14.95	114
6.48	0.43	6.72	14.80	113
9.71	0.63	7.04	14.70	111
16.15	1.01	7.10	14.64	112
24.20	1.48	7.30	14.54	111
48.38	2.84	8.18	14.39	103
54.47	3.74	8.44	14.39	102
72.44	4.15	8.73	14.32	100
80.55	4.54	8.87	14.26	100

Table 5.19 Modal properties of the FRFs obtained with random excitation for the 100% *CLD* RSS tested at 20ºC

F_r [N]	$a_{max,r}$ [m/s^2]	$\xi_{1,100\%}$ [%]	$f_{1,100\%}$ [Hz]	$m_{1,100\%}$ [kg]
0.15	0.005	6.29	15.67	152
0.30	0.01	6.24	15.21	121
0.59	0.02	5.87	14.95	120
0.12	0.04	6.05	15.08	115
2.35	0.08	6.20	14.91	112
3.52	0.13	6.02	14.78	113
4.69	0.14	6.26	15.01	113
5.86	0.22	6.33	14.93	113
8.73	0.34	6.47	14.86	113
11.74	0.40	6.18	14.88	118
14.62	0.54	6.61	14.83	113
17.59	0.58	6.53	14.78	115

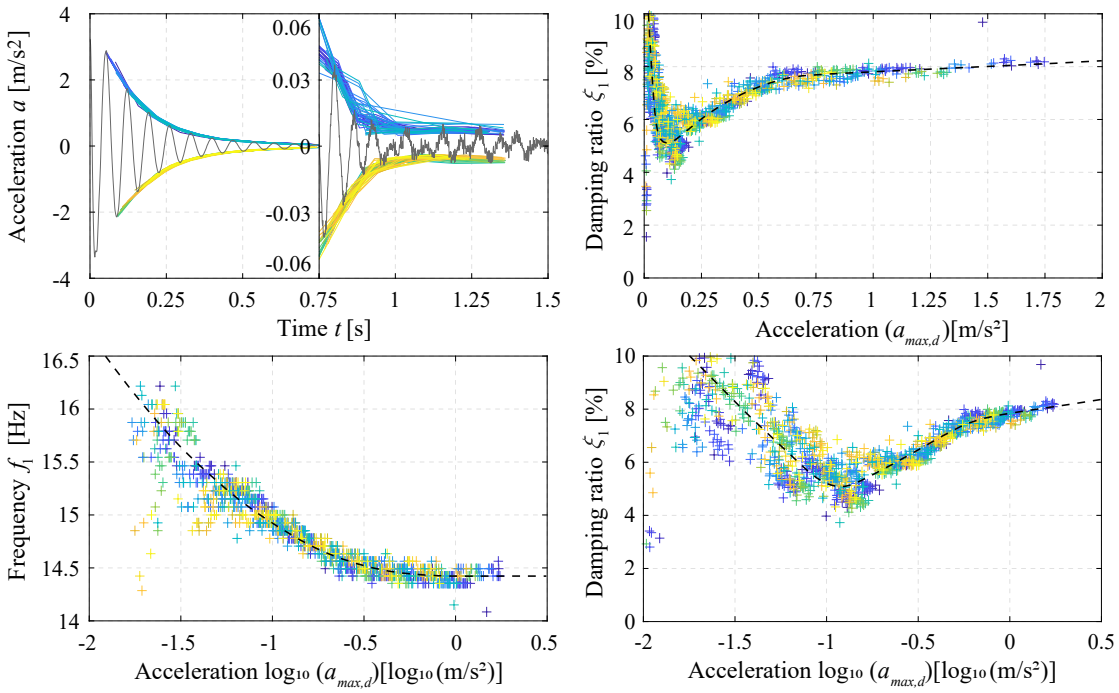

Figure 5.31: Experimental Results for free-decay test on the 100% *CLD* RSS tested at 20ºC

5.6.6 OMA results

This final subsection presents the results obtained from the OMA tests in the form of the stabilization diagrams shown in Figure5.32.

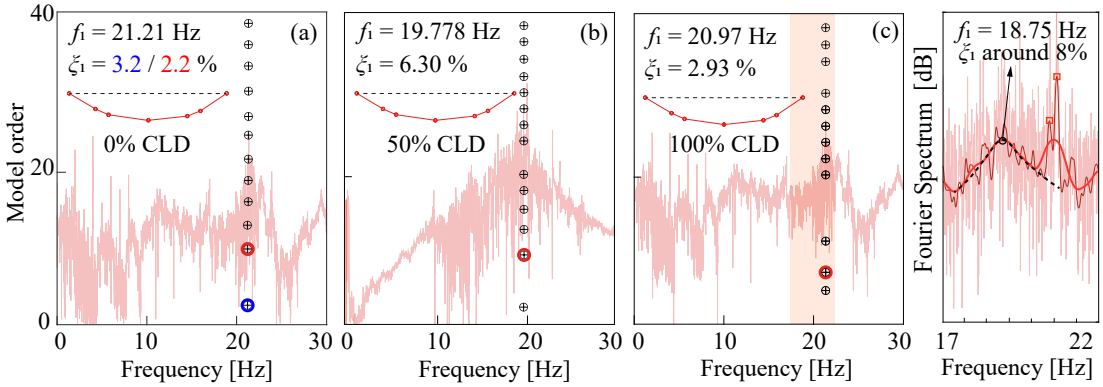

Figure 5.32: Results from OMA Analysis. (a) RSS with 0% CLD. (b) RSS with 50% CLD. (c) RSS with 100% CLD. (d) Fourier transform of the RSS with 100% CLD around its fundamental frequency.

For the RSSs with 0% CLD and 50% CLD the SSI-cov algorithm provided reasonable results in terms of ξ_1 and f_1. However, for the RSS with 100% CLD, the value of ξ_1 derived from the OMA resulted to be surprisingly low. For this reason, the Fourier transform of this signal was analyzed more in detail, as shown in Figure 5.32.(d). A smoothing technique was used with different levels of intensity, trying to reveal the actual nature of the resonant peaks of the signal. Next to the picked peak by the OMA, a wider one, with a lower natural frequency was founded. The 'Half power method' was directly applied to the response spectrum (something arguable, as implies assuming that the spectrum of the input ambient force is constant), and a damping ratio of 8% was obtained, which matches the results previously obtained for this beam. This fact evidences that capturing modes with such a big damping ratio using OMA techniques is usually challenging.

5.7 Discussion

To develop a deeper discussion of the experimental results provided above, a summary of them has been developed in Figure 5.33. Figure 5.33.(a) shows the evolution of f_1 with respect to a_{max} expressed in logarithmic scale. a_{max} here, encloses the three parameters

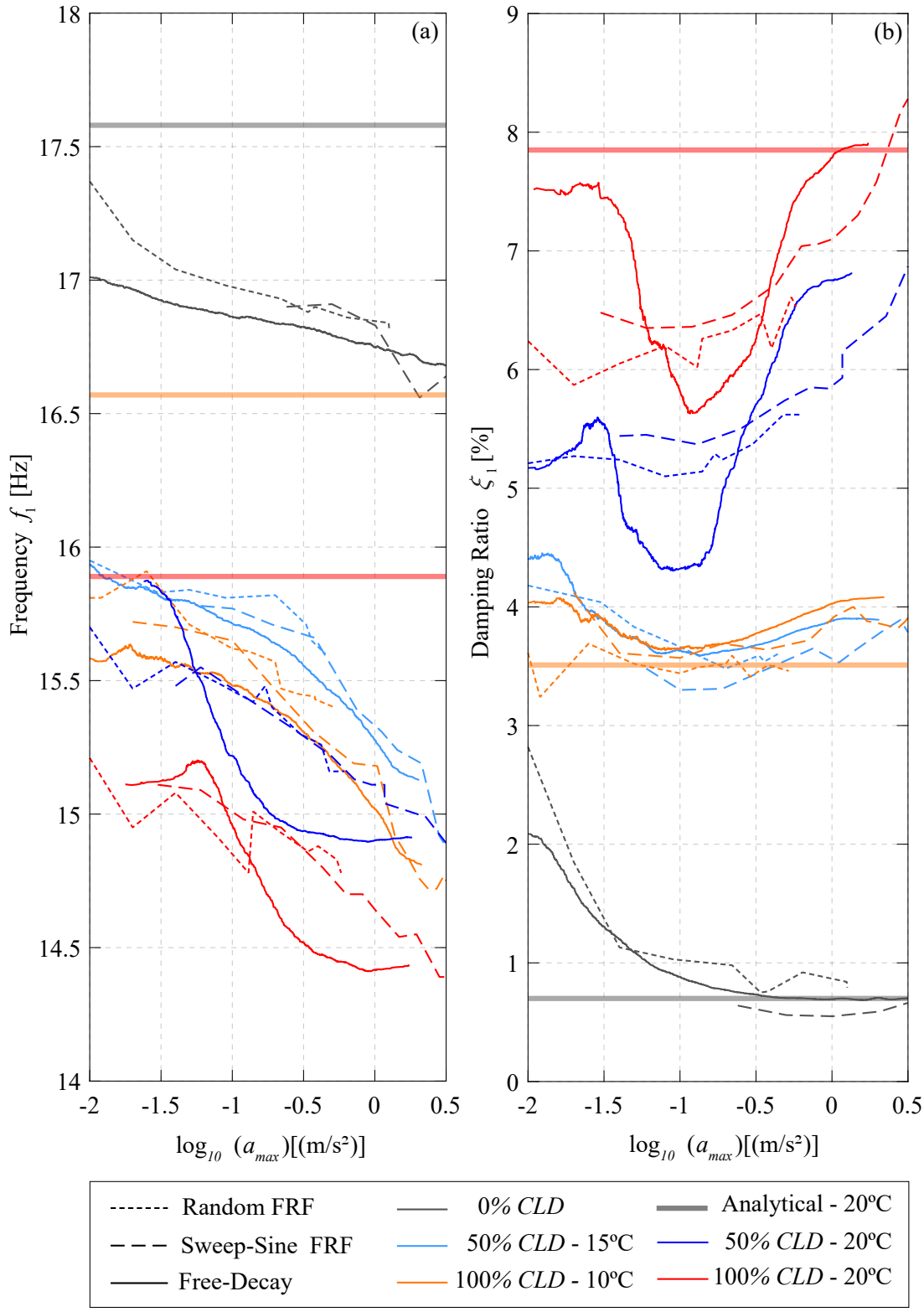

Figure 5.33: Summary of results

$a_{max,ss}$, $a_{max,r}$ and $a_{max,d}$, at the same time, as the results from the EMA and free-decay tests have been plotted together, each one with a different line type (the lines of the free-decay tests have been obtained with a moving mean). The five experimental cases introduced in Table 5.9 have been plotted together assigning a different colour to each test. Finally, the analytical results predicted for the RSSs with the VE mechanical properties at 20ºC (previously shown in Table 5.4) have been illustrated with horizontal, lighter and thicker lines. Similarly, Figure 5.33.(b) summarizes the evolution of ξ_1 with the logarithm of the amplitude of motion a_{max}.

In Figure 5.33.(b), the analytical predictions of ξ_1 for the RSSs with 50 and 100% CLD do not coincide with the values $\xi_{RS} = (\eta_{RS}/2)100$ provided in Table 5.4. This is because a base damping ratio of 0.7% (the one observed on the 0% CLD beam at high motion amplitudes) has been added to the predicted values ξ_{RS}. This has been done to account for the total damping ratio of the beams, and not only for the additional damping ratio provided by the CLD treatment. For example, on the 100% CLD beam the additional ξ_{RS} was equal to 0.143/2*100 = 7.05%. When adding to this value the base 0.7%, the final value of 7.75% plotted in Figure 5.33.(b) is obtained.

The discussion of the results has been structured in two parts. First, the experimental predictions of f_1 and ξ_1 using different methodologies have been commented on, and second, the degree of correlation between the predicted and the experimentally observed modal properties of the RSS, has been assessed.

5.7.1 Discussion about the experimental results

The conclusions that may be extracted from a careful analysis of the experimental results obtained are the following ones:

- In general terms, it can be appreciated a logical decrease of the f_1 when the % CLD increases. Hence, the highest natural frequency is achieved for the 0% CLD beam, while the beam with 100% CLD displays the lowest one.
- For CLD-treated beams, the influence of the temperature in their f_1 is notable. For example, in the RSS with 50% CLD, the fundamental frequency is higher at 15ºC, as the VE core is stiffer at lower temperatures. This variation of the beam bending stiffness with the temperature is much more perceptible in the 100% CLD beam, in which $f_{1,100\%}$ decreases up to 0.5 Hz from 10 to 20ºC when vibrating at high motion

amplitudes.

- As it was expected, the higher the % CLD, the higher the ξ_1 observed.
- For the RSS with 100% CLD, the lower the temperature, the lower the ξ_1. This change, though, is not as noticeable on the 50% CLD beam. When lowering the temperature 10ºC, the HIP2 material of the VE core will increase its shear stiffness G_2' by a factor of around 2, however, its loss factor, $\eta_{2,ve}$, will be kept constant around a value of 1. Assuming that $\eta_{2,ve}$ will not vary, implies that the bell-shape curves used in Chapter 3 to predict the damping, can be now used to explain this phenomenon. Therefore, these charts have been plotted for the 50 and 100% CLD beams with a geometric parameter $Y = 1.66$, as can be seen in Figure 5.34. When introducing the shear parameters g estimated for the different temperatures, it results evident that the 100% CLD beam is much more sensitive to a temperature change than the 50% CLD one. However, the level of sensitivity predicted is much higher than the one appreciated in the experiments. For a better understanding of this mismatch, an independent mechanical characterization of the VE material HIP2 at different temperatures, frequencies and amplitudes of motion would be required.

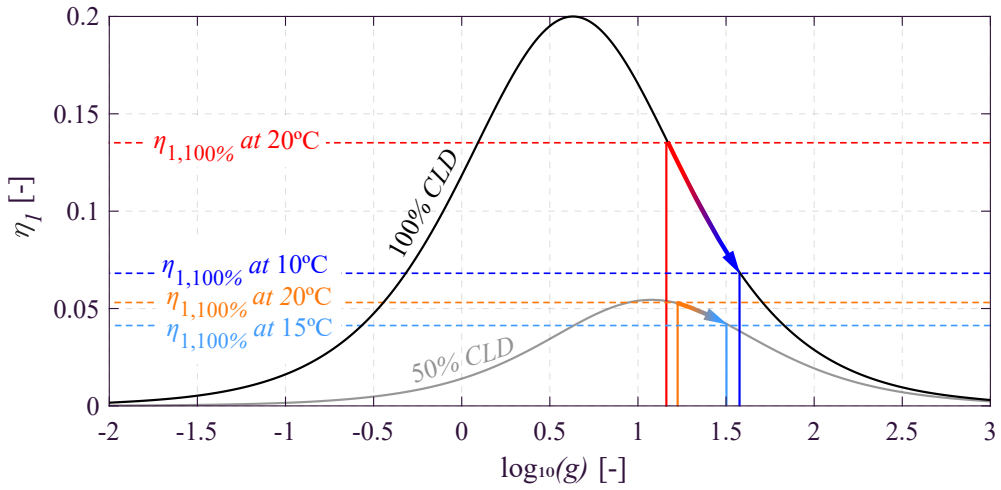

Figure 5.34: Influence of a temperature change on the fundamental loss factor of the RSSs with 50 and 100% CLD.

- The modal parameters obtained with the EMA tests carried out with sweep-sine and random excitation tend to correspond. A higher mismatch is found between the EMA and the free-decay predictions, especially for the RSSs with 100% CLD.
- Overall, it can be appreciated that the lower the amplitude of motion, the higher the

natural frequency. This might be explained by the frictional forces that become more prevalent at lower amplitudes, forcing the beam to change from a simply supported state to an encastred one. In fact, the OMA results exhibit much more higher values of f_1 than those presented in Figure 5.33.

- The behaviour of ξ_1 concerning the motion amplitude varies depending on the RSS analyzed. For the 0% CLD beam, the lower the amplitude, the higher the ξ_1. Indeed, $\xi_{1,0\%}$ increases from 0.7% to almost 3% on the OMA test. The 50% CLD beam displays a fairly constant value of $\xi_{1,50\%}$ around 3.5-4% that slightly increases for very-low motion amplitudes till the 6%. These increments of $\xi_{1,0\%}$ and $\xi_{1,50\%}$ might be explained by the friction developed at the shear-connected regions, which at lower amplitudes becomes an important source of damping. Finally, the behaviour of the 100% CLD beam is difficult to understand. For this specimen, the EMA tests predict a reduction of $\xi_{1,100\%}$ with the amplitude. However, the free-decay tests evidence a sort of 'U' shape for $\xi_{1,100\%}$, which is drastically reduced for motion amplitudes around 0.1 m/s^2.

5.7.2 Comparison with predicted modal parameters

The predictions for the RSS were done at a temperature of 20ºC, as this temperature is the only one directly appearing on the nomogram of Figure 5.3. To avoid additional errors coming from interpolation, predictions at other temperatures were not performed. Two main conclusions can be extracted from a comparison with the experimental results:

- The natural frequencies predicted are higher than those measured. Three main facts could explain this: i) not having considered the long-term elastic properties of the concrete in the predictions ii) not having taken into account the actual elastic behaviour of the shear-connected region, and iii) not having a good characterization of the VE material used in terms of the motion amplitude.
- The values of ξ_1 predicted agree well with those measured for higher motion amplitudes. In the low-motion range the results for $\xi_{1,50\%}$ are satisfactory, however, the level of matching of $\xi_{1,100\%}$ could be argued.

Looking at the results of $\xi_{1,100\%}$ on the EMA tests (the lower the amplitude, the lower the $\xi_{1,100\%}$) it could be reasonable to think that the mechanical behaviour of the VE material could depend on the level of shear deformation on the VE core; in other

words, on the magnitude of shear slip reached between the concrete and the steel. This shear slip is related to the amplitude of motion at mid-span in terms of displacement, not acceleration. It is important to highlight that the range of displacements tested on the RSSs is much lower than those that would be reached on FSSs for the same acceleration because the natural frequencies of the latter ones are aroung 3 times lower. Subscribing this, an acceleration level of 0.05 m/s^2 in the FSS should be compared to one of 0.05x3x3 = 0.45 m/s^2 in the RSS.

After all, the author considers that the performance achieved by the CLD treatment tested is good and its mechanical behaviour is reasonably predictable.

5.8 Conclusions

This chapter has been devoted to the experimental testing of three RSSs with different degrees of CLD treatment, 0, 50 and 100% CLD. These RSSs have been developed to replicate three Full-scale beams that for economical and laboratory space reasons, could not be built and tested. The main objective of these tests was to confirm the damping capacity of the CLD treatments as evidenced by an increase in the fundamental damping ratio ξ_1 of the CLD-treated beams. Four types of dynamic non-destructive tests were performed on each beam: i, ii) two EMA tests using five accelerometers and an electrodynamic shaker driven by sweep-sine and random excitation, considering different amplitudes for the applied force, iii) A free-decay test, and iv) an OMA test. The modal properties ξ_1 and f_1 of the fundamental mode of vibration of each RSS, have been extracted from each test performed. Special attention has been paid to the characterization of these modal parameters depending on the amplitude of motion of the beams. As a summary, the RSS with 50% CLD has exhibited a damping ratio of around 4%, while the 100% CLD one has reached damping ratio values of up to 8%. Additionally, the influence of the temperature on the mechanical properties of the VE material used has been confirmed. After all, the agreement between the predicted and the measured results seems to be satisfactory. This research demonstrates that the CLD technology studied can be applied on full-scale floors to reduce their vibration level feasibly and predictably.